UCLouvain

epl

École polytechnique de Louvain

Quantum behaviour of the electrons in nanodevices : study of a macroscopic analogy

Comparison between the walking droplet and the electron behaviour inside a chaotic stadium cavity

Author: **Olivier LEBLANC**
Supervisor: **Benoît HACKENS**
Readers: **Laurent FRANCIS, Loïc TADRIST (ULiège), Vincent BAYOT**
Academic year 2019–2020
Master [120] in Electrical Engineering

Aknowledgements

First of all, I sincerely would like to thank my advisor Benoît Hackens for accepting this subject proposal. He gave me the opportunity to spend time and energy with passion on a work field quite remote compared to the typical choices of an electrical engineering student. Including Boris-Brun Barrière, Nicolas Moreau and Sébastien Toussaint, I want to thank them all for a frequent and very interactive assistance on every question or issue raised during the development of my whole project. I had to discover and learn most of the state of the art in this field, and their reflection throughout the whole year more than contributed to the work I realized. I also want to thank Laurent Francis, Vincent Bayot and Loïc Tadrist who did me the honor of participating on my jury. More particularly, I was kindly welcomed twice at the *Microfluidics lab* at Uliège by Loïc Tadrist and Tristan Gilet, experts in this work field, to visit their laboratory. They brought me important advices on some features of the setup, and gave me a 3D-printed reservoir useful for the droplet generator. Loïc also bothered helping me, a first time in the working of the droplet generator and a second one remotely, in the debugging of my vibrating set. In addition to them, I have to thank Corentin Félix for the design and fabrication of multiple parts of the experimental setup (confined geometries, droplet generator, structure containing the bath, ...) as well as very constructive discussions on the feasibility of some experimental setup parts. More generally, I had the opportunity to discuss about technical details with many persons from UCLouvain. I have always been generously helped and I always received the expertise boosts I was looking for.

Finally, I thank my family for their support in my passion and investment in my studies for five years. More particularly, they had to adapt to my working schedule during three entire months of confinement at home. I end with all my friends for their precious support throughout these years of study.

Abstract

The walking droplet experiment has received particular attention in the last fifteen years because it represents the first known example of a macroscopic pilot-wave system that exhibits behaviours thought to be exclusive to the microscopic quantum realm. Most efforts about walking droplets have focused on the experimental analysis in a "fluid mechanics" framework and on its mathematical modeling.
On the other hand, the stadium billiard, one of the first 2D concave chaotic geometries introduced by *Bunimovich*, has been actively studied for these last decades because of the drastic differences observed between classical and quantum particles behaviour in such geometry.
Consequently, the objective of this master thesis is to analyze the behaviour of walking droplets inside the Bunimovich stadium billiard and compare it with the behaviours of classical and quantum particles in similar conditions. To fulfil this objective, a complete low-cost experimental setup has been developed for the observations of walking droplets, comprising : a fabricated bath stuck on the membrane of a loudspeaker for the vertical shaking, a 3-axis accelerometer providing real-time measurements on PC, a droplet generator based on a piezoelectric buzzer and a fixed camera recording top view images of the droplet motion which are post-processed with *Matlab*. The imperfect horizontality of the developed setup is shown to lead to an effective Faraday instability threshold lower than the scientific consensus for the same forcing parameters ($\Gamma_{F,e} = 2.3[g] < \Gamma_F = 4.144[g]$). As it prevents us to correctly estimate the memory parameter Me, the conducted experiments are instead described in terms of shaking amplitude Γ and estimated tilt angles of the bath θ and β. It is observed that the walking droplet long-term evolution in a stadium billiard presents a clear scarring pattern, informing on the existence of preferred "probable positions" of the droplet inside the billiard. The scarring pattern, while very similar to a typical shape found in quantum simulations, is surprisingly much more robust against forcing variations than the scars observed for electrons.

Keywords: Walking droplet, Stadium, Chaotic, Scar

Contents

1 Introduction **1**

2 Chaotic cavities : the stadium case **4**
2.1 Ergodicity in the classical world 5
2.2 Scarring in the quantum world 7

3 State of the art on walkers **8**
3.1 Modeling the walking droplet pilot-wave system 11
3.2 Review of droplet experiments 20
3.2.1 Bouncing and walking regimes 20
3.2.2 Interaction with interfaces 22
3.2.3 Evolution in a varying potential or a confined geometry 25
3.2.4 Interactions between multiple droplets 29

4 Walking droplet experiment **31**
4.1 Experimental setup 31
4.1.1 Vertical oscillations 33
4.1.2 Droplet on-demand generator 36
4.1.3 Surface visualization 40
4.1.4 Droplet tracking 48
4.2 Validation 52
4.3 Results and discussion 53

5 Electronic transport analysis **56**
5.1 Quantum simulations 58
5.2 Results and discussion 60

6 Conclusion and perspectives **63**
6.1 Discussion on the obtained results 63
6.2 Experimental setup improvement 64
6.3 Perspectives for future research 65

Appendices **66**

A Vertical oscillations **67**

B Quantum simulations **69**
B.1 Simplification of the lattice 69
B.2 Simplification of the Schrödinger equation 70

Bibliography **71**

List of Figures

2.1 Stadium billiard geometry. . . . 4
2.2 Stable orbits in the stadium billiard. . . . 5
2.3 Chaotic trajectories in the stadium billiard. . . . 5
2.4 Simulated LDOS for electrons confined in a stadium billiard. . . . 7

3.1 Liquid movement initiation converging to Faraday waves. . . . 8
3.2 Top view of the Faraday instability. . . . 8
3.3 Faraday waves propagation viewed from top. . . . 9
3.4 Decay time τ of an initial disturbance as a function of the γ_m acceleration in the vicinity of the Faraday threshold. . . . 9
3.5 Experimental and simulated liquid surface wavefields. . . . 10
3.6 (f, Γ) curve for different viscosity values. . . . 11
3.7 $(k - \Gamma)$ curve. . . . 11
3.8 Spatiotemporal simulation of the vertical dynamics of a bouncer. . . . 12
3.9 Three spatiotemporal images showing the vertical behaviour of a bouncing droplet. 12
3.10 Bifurcation diagram of the different vertical heights reached by the droplet for various accelerations Γ obtained by simulation. . . . 13
3.11 Simulated liquid surface profiles for two different actuations. . . . 16
3.12 Simulated radial gradient of surface waves versus time and position. . . . 17
3.13 Wave amplitude and trajectories for wall reflection. . . . 19
3.14 Spatio-temporal 3D reconstruction of a wave propagation. . . . 20
3.15 Temporal evolution of the liquid height. . . . 20
3.16 Spatiotemporal diagrams of various observed bouncing modes. . . . 20
3.17 Bouncing mode diagram. . . . 21
3.18 Measured Doppler effect with walkers' wavefields. . . . 21
3.19 Experimental set-ups for single- and double-slit geometries. . . . 23
3.20 Comparison between observed single-slit and double-slit trajectories. . . . 23
3.21 Trajectories of a walker passing through the slit with fixed impact parameter and various amplitudes of forcing. . . . 23
3.22 Dependence on the memory γ/γ_F of the reflection of a walker for a fixed initial angle of incident. . . . 24
3.23 Walker's trajectories in rectangular waveguides. . . . 24
3.24 4 examples of cassinian trajectories. . . . 26
3.25 Circular orbits quantification as Me increases. . . . 26
3.26 Double quantification of the stable orbits. . . . 26
3.27 Observed dependence of the orbital radius r_0 on the rotation rate of the bath Ω 27
3.28 Orbital stability diagram . . . 27
3.29 Walking regime stability diagram . . . 27
3.30 Pictures of a circular corral . . . 28
3.31 2D pdf inside a circular cavity . . . 28

3.32 Observed lattices. 29
3.33 Trajectories along a line of 11 droplets in hexagonal symmetry 29
3.34 Collisions and promenades of interacting walkers 30
3.35 Measured diameter of the orbit of two walkers 30

4.1 Schematic of the experimental setup. 32
4.2 Real experimental setup 33
4.3 Calibration of the Arduino Uno measurement. 35
4.4 Calibration of the myDAQ measurement. 35
4.5 Sensitivity improvement circuit. 35
4.6 Calibration using the myDAQ after signal amplification 35
4.7 Measured vs pure sine normalized acceleration waveforms. 36
4.8 Measured vs pure sine normalized acceleration spectra. 36
4.9 Schematic of the constructed DOD 37
4.10 Square signal that activates the piezoelectric buzzer 37
4.11 Push button montage for generating a droplet. 37
4.12 Pulse widths gap between the Arduino Uno command and the measured pulse applied at the piezoelectric buzzer terminals. 37
4.13 Droplet detection algorithm results for each step. 38
4.14 Multiple estimations of the diameter of the same droplet 39
4.15 Estimations of ten different droplets' diameters generated with the same parameters 39
4.16 Schematic of the setup for ray deviations' based surface reconstruction 40
4.17 Obtained liquid surface wave field for a single walker. 41
4.18 Obtained liquid surface wave field for an orbiting pair of walkers. 41
4.19 Brewster angle method : intensity ratio for varying incidence angle θ_1 42
4.20 Brewster angle method : intensity ratio for varying deviation angles Δ_θ 42
4.21 Schematic drawing of the Schlieren system working in reflection 43
4.22 Conventional Schlieren method. Arrangement of the knife-edge and typical response curve 43
4.23 Schematic of the proposed montage for a 2D free surface recovery with the PSS method. 44
4.24 Three-dimensional ray geometry for a horizontal interface (reference case) 44
4.25 Two-dimensional view of the vertical incidence plane COM 45
4.26 Two-dimensional view of the incidence plane CAM. 45
4.27 Random dot pattern 46
4.28 DIC based surface profile recovery results 47
4.29 Tracking algorithm display 49
4.30 Result of the correlation for the surface reconstruction 50
4.31 Final obtained metric for the surface reconstruction 50
4.32 Comparison between manually and automatically computed trajectories 50
4.33 Histogram of the droplet position error 50
4.34 Tracking algorithm display for the dot pattern case 51
4.35 Comparison between manually and automatically computed trajectories for the dot pattern case 51
4.36 Histogram of the droplet position error for the dot pattern case 51
4.37 Trajectory and density observations in the stadium cavity 53
4.38 Isometric view of the density and speed histogram in the stadium cavity 53
4.39 Other pattern for the walking droplet in the stadium cavity 54
4.40 Robustness of the ∞-like shaped pattern against frequency and forcing amplitude variations 55

5.1 Simulated conductance fluctuations in the stadium billiard 57
5.2 Typical scars in a stadium-shaped graphene confinement 57
5.3 Schematic of the square lattice 58
5.4 Energy dispersion (band structure) 58
5.5 LDOS with Pybinding 60
5.6 pdf with Kwant 60
5.7 Pattern for the recurrence curve 60
5.8 Recurrence curve 60
5.9 Similar pattern for the walking droplet and the electron in stadium cavities . . . 62

A.1 Electrical connections 67
A.2 Front panel of the developped Labview program. 68

B.1 Organization of the atoms in $Al_xGa_{1-x}As$ 69
B.2 Schematic of a square lattice 69

Nomenclature

List of Abbreviations

2DEG	Two Dimensional Electron Gas
AI	Analog Input
AO	Analog Output
dBB	de Broglie-Bohm
DIC	Digital Image Correlation
FFT	Fast Fourier Transform
FS-SS	Free-Surface Synthetic Schlieren
i.i.d	independant and identically distributed
LDOS	Local Density Of States
LED	Light-Emitting Diode
N2DCC	Normalized 2D Cross-Correlation
PDE	Partial Differential Equation
pdf	probability density function
PI	Proportional Integral
PSS	Phase-Shifting Schlieren
ROI	Region Of Interest
RV	Random Variable
SISO	Single-Input Single-Output
std	standard deviation
THD	Total Harmonic Distorsion

Table 1: **List of default parameters.**

Name	Symbol	Value	[Unit]
Fundamental constants			
Gravitational acceleration	g	9.81	$[m/s^2]$
Air properties			
Air density	ρ_a	1.2	$[kg/m^3]$
Air kinematic viscosity	ν_a	15	$[cSt]$=$[mm^2/s]$
Air dynamic viscosity	μ_a	$1.84 \cdot 10^{-5}$	$[Pa.s]$=$[kg.m^3/s]$
Air density	ρ_a	1.2	$[kg/m^3]$
silicone oil properties			
Oil density	ρ	$0.95 \cdot 10^3$	$[kg/m^3]$
Oil kinematic viscosity	ν	20	$[cSt]$=$[mm^2/s]$
Oil dynamic viscosity	$\mu = \rho\nu$	$19 \cdot 10^{-3}$	$[Pa.s]$=$[kg/m.s]$
Surface tension	σ	20.6	$[mN/m]$
Droplet properties			
Droplet diameter	D	$[0.4 - 1.2]$	$[mm]$
Droplet radius	$R_0 = \frac{D}{2}$	$[0.2 - 0.6]$	$[mm]$
Droplet mass	$m = \rho\frac{4\pi R_0^3}{3}$	$[3.2 - 85.6] \cdot 10^{-8}$	$[kg]$
Characteristic drop oscillation frequency	$\omega_D = \sqrt{\frac{\sigma}{\rho R_0^3}}$	$[316.8 - 1646]$	$[rad/s]$
Vertical oscillations and Faraday			
Sample rate	N	10 000	$[-]$
Frequency of forcing	f_0	80	$[Hz]$
Pulsation of forcing	$\omega_0 = 2\pi f_0$	160π	$[rad/s]$
Liquid height	h_0	$[6 - 11]$	$[mm]$
Acceleration peak	γ_m	$[0 - 50]$	$[m/s^2]$
Non-dimensional acceleration peak	$\Gamma = \frac{\gamma_m}{g}$	$0 - 5$	$[-]$
Effective gravity	$g_\Gamma(t) = g(1 - \Gamma cos(\omega_0 t))$	-	$[m/s^2]$
Faraday wavelength	λ_F	4.72	$[mm]$
Faraday wavenumber	k_F	1330	$[rad/m]$
Faraday period	T_F	25	$[ms]$
Faraday threshold	γ_F	40.65	$[m/s^2]$
Non-dimensional Faraday threshold	$\Gamma_F = \frac{\gamma_F}{g}$	4.144	$[-]$
Distance to Faraday threshold	$\mathcal{M} = \frac{\Gamma_F}{\Gamma_F - \Gamma}$	$[0 - (+\infty)]$	$[-]$
Vanishing viscosity wavenumber [68]	$k_0 = k$ s.t. $\Gamma_F \longrightarrow 0$	1319.5	$[rad/m]$
Free damping [68]	$\gamma_0 = \frac{4\nu k_0^2}{\omega_0}$	0.277	$[-]$
Memory [68]	$Me = \frac{\mathcal{M}}{2\pi\gamma_0}\left(1 + \frac{\gamma_0^{1/2}}{2} + \frac{\gamma_0}{4}\right)$	$[0 - (+\infty)]$	$[-]$
Faraday phase velocity	$v_F^\phi = \sqrt{\frac{g}{k} + \frac{\sigma k}{\rho}}$	190.8	$[mm/s]$
Capillary length	$l_c = \sqrt{\frac{\sigma}{\rho g}}$	1.5	$[mm]$
Capillary frequency	$f_c = \sqrt{\frac{\sigma}{m}}$	$[155 - 805]$	$[Hz]$
Vibration number	$\Omega = \frac{\omega}{\omega_D}$	$[0.049 - 0.25]$	$[-]$
Bouncing mode	(m, n)	(-,-)	$[-]$
Drop incoming speed	V_{in}	0.1-1	$[m/s]$
Drop outgoing speed	V_{out}	0.01-1	$[m/s]$
Restitution coefficient	$C_R^N = \frac{V_{\text{in}}}{V_{\text{out}}}$	~ 0.7	$[-]$
Adimensional numbers			
Bond number $= \frac{\text{gravitational forces}}{\text{surface tension forces}}$	$\mathcal{B}o = \frac{\rho g R_0^2}{\sigma}$	$[0.018 - 0.163]$	$[-]$
Weber number $= \frac{\text{inertial forces}}{\text{surface tension forces}}$	$We = \frac{\rho R_0 V_{in}^2}{\sigma}$	~ 0.1	$[-]$
Ohnesorge number $= \frac{\text{viscous forces}}{\sqrt{\text{inertia} \cdot \text{surface tension}}}$	$Oh = \frac{\mu}{\sqrt{\rho\sigma R_0}} = \frac{\sqrt{We}}{Re}$	$[0.175 - 0.3]$	$[-]$
Stokes drag coefficients	$c_{St} = 6\pi R_0 \mu_a$	$[6.94 - 20.81] \cdot 10^{-8}$	$[kg/s]$

Chapter 1

Introduction

Today, the most widely accepted interpretation of the quantum mechanics equations is the *Copenhagen* interpretation [78] which states that physical systems generally do not have definite properties prior to being measured, and that the measurement's possible results only obey a probability distribution that is predicted by quantum mechanics. It stands that this is the measurement which forces the collapsing of the wave function to only one of the possible values. However, many other non rejectable interpretations of quantum mechanics have been proposed. [82] These ones differ on such fundamental questions as whether quantum mechanics is deterministic or stochastic, which elements of quantum mechanics can be considered real, and what is the nature of measurement, among other matters. The *De Broglie* theory (distinguished from the de Broglie-Bohm association as discussed in [9]), on the contrary of the Copenhagen interpretation, is a deterministic theory that associates a real pilot-wave that is created by the particle itself and guides its motion inside the space. It considers that the particle has, at any time, a definite and real position. This particle's position is practically unknown, but can be statistically predicted by the *guiding equation*. [79] In the *De Broglie* theory, the wave function obeying the Schrödinger equation is not real and is only representative of the averaged behaviours of the particle.

The first example of a macroscopic system exhibiting a wave-particle duality has been raised in 2006 by Couder and his team [22] (find a short movie in [55]). This consists in a silicone oil droplet bouncing on a vertically vibrated bath, generally sinusoidally. With an appropriate set of forcing parameters (i.e. frequency and amplitude of the vertical shaking), this droplet can spontaneously start "walking" on the liquid surface (i.e. moving laterally) and in this case exhibits behaviours thought to be exclusive to the microscopic quantum realm such as self-organising lattice structures, single particle diffraction, quantized orbits, orbital level splitting, tunneling effects, and wave-like statistics in confined geometries. Given the contrasting behaviour between classical and quantum particles, one can then naturally wonder whether the droplet "walkers" behaviour will mimic the classical or the quantum behaviour.

The Bunimovich stadium billiard has received particular attention by the scientific community for these last decades because of the drastic differences observed between classical and quantum particles behaviour in such geometry.
On the one hand, the classical ball bouncing elastically on the borders of the stadium tends, over time, to visit the entire 2D geometry except for some unstable regular orbits. The stadium billiard is said *chaotic* due to its exponential sensitivity to initial conditions, leading to practical impossibility to predict the ball trajectories if there exists even an infinitesimal uncertainty on the initial conditions (i.e. initial position and speed). As for meteorology, deterministic systems that are chaotic are usually described by means of statistical tools which can handle

the possibility of some uncertainty on the initial state.
On the other hand, quantum particles like electrons show patterns of higher probability of presence inside the cavity called quantum *scars*, which curiously look like the unstable regular orbits of the classical case. This phenomenon is due to the influence of the stadium chaotic geometry on the wave function, solution of the Schrödinger equation.

In other words, the central question of this master thesis is :

"*How does the behaviour of a walking droplet (a.k.a.* walker*) compare to the classical and quantum particles' behaviours inside a Bunimovich stadium cavity?*".

While this question may seem only academic, it has important consequences. Demonstrating that the walker faithfully reproduces the electronic behaviour, for example, would provide an easy table-top solution for exploring complex physical problems related to electron dynamics, correlated electron behaviour, including many-body effects that are otherwise extremely difficult, if not impossible, to reproduce through simulations.

To explore this issue, we devised an approach relying on one side on experimental observation of walker behaviour inside a macroscopic billiard, and on the other side on quantum simulations of electron dynamics inside a similar billiard. For the observations, an entire experimental setup has been developed to control the forcing parameters as well as to perform the most accurate quantitative measurements possible, given the available means (see details in Section 4). Noteworthy, the proposed setup has been created with very low budget (< 500 euros for all components) and is made up of the following key elements :

- a fabricated bath stuck on the membrane of a simple loudspeaker, itself driven by a PC through a NI myDAQ device.
- a single 3-axis accelerometer fixed at the center of the bath and giving the vertical acceleration voltage measurement as analog input to the same NI myDAQ, after being passed into an amplifier montage aiming at improving the measurement sensitivity (Figure 4.5).
- a *droplet on-demand generator* applying square voltage pulses on a piezoelectric buzzer to induce a pressure variation in a fluid reservoir creating the droplet. This DOD generator is activated by a simple Arduino Uno code when pushing a button mounted on breadboard (Section 4.1.2).
- image post-processing tools developed on *Matlab* for the *droplet tracking* (Section 4.1.4) as well as the *surface visualization* (Section 4.1.3).

In this master thesis, Chapter 2 introduces the main concepts related to chaotic geometries, especially to the one of interest : the Bunimovich stadium billiard. A brief comparison between the behaviour of the classical particle and the quantum particle is presented in Sections 2.1 and 2.2.

Chapter 3 gives a general overview of the state of the art on walking droplets. The evolution of the mathematical modeling of this pilot-wave system is described in Section 3.1 and Section 3.2 synthesizes the experimental observations obtained with walkers.

Chapter 4 describes the experimental setup developed during the thesis and the methods used to analyze the data with a discussion on the rationale behind the made choices made during its conception. It is shown that the low-cost conception does not produce a pure enough uniaxial shaking to give an accurate estimation of the memory parameter Me (introduced in Chapter 3), so the observations are given with an estimate of the tilt angles of the bath and the measured acceleration along the z-axis. This setup is nonetheless already suitable for capturing relevant observations about a robust ∞-like shaped pattern.

Chapter 5 describes the strategy used to simulate the electronic transport behaviour in the stadium cavity with a simplified square lattice and considering a *tight-binding* approximation. The results obtained with two distinct *Python* packages, namely *Kwant* and *Pybinding*, are presented and discussed by comparison to the related literature and more importantly to the observations made with walking droplets in Section 4.3.

Finally, a concluding discussion comprising a synthesis on the obtained results, perspectives for further research in this hot topic and perspectives for a setup enhancement are detailed in Chapter 6.

Chapter 2

Chaotic cavities : the stadium case

In this section, we brief the concept of chaotic geometries by particularizing the discussion on the Bunimovich stadium billiard. The main differences in behaviour between a classical particle and a quantum particle inside the stadium billiard are highlighted.

The stadium billiard is a 2D geometry which consists in two semi-circles separated by a distance $2a$ (where the choice of $2a$ stands for the sake a writing simplicity) along their axis of orthogonal symmetry, as shown in Figure 2.1. This seemingly simple geometry was one of the first shown to be chaotic despite the absence of concave borders by Bunimovich [70], and is thus also called *Bunimovich stadium*.

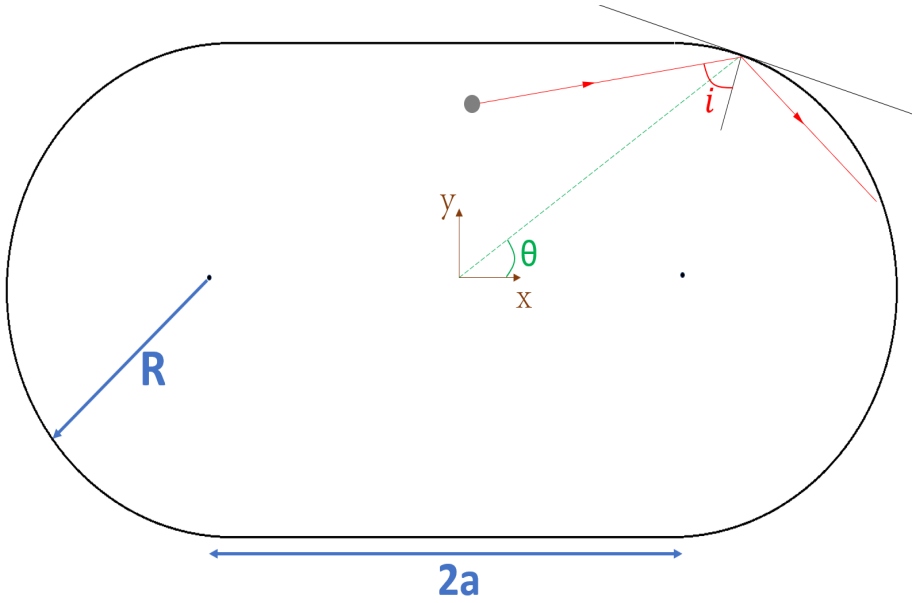

Figure 2.1: Stadium billiard geometry. We consider 2D cartesian frame (x, y) with its origin placed at the center of the stadium.

2.1 Ergodicity in the classical world

In classical physics, if ones considers the perfectly elastic bounces of a ball on the borders of the stadium billiard, this leads to a discrete dynamical system which can be unambiguously described by two quantities. In this case, as illustrated in Figure 2.1, we define the phase space as :

$$(\theta_n, \sin(i_n)) \tag{2.1}$$

which is called the *phase space* representation of the system. Here, θ_n is the angle formed between the impact point and the origin $(0, 0)$ of the stadium, i_n is the angle between the incidence trajectory of the ball on the border and the line normal to the stadium curvature at the impact point and n stands for the n-th bounce of the ball on the stadium borders.

The stadium billiard is said to be *ergodic* because for most of the possible initial conditions $(\theta_0, \sin(i_0))$, a billiard ball will, over time, uniformly explore the real space of the billiard and almost uniformly explore the phase space (Figure 2.3). However, it is not uniquely ergodic as there do exist some exceptional choices of initial position and velocity for which one does not have uniform distribution. (Figure 2.2).

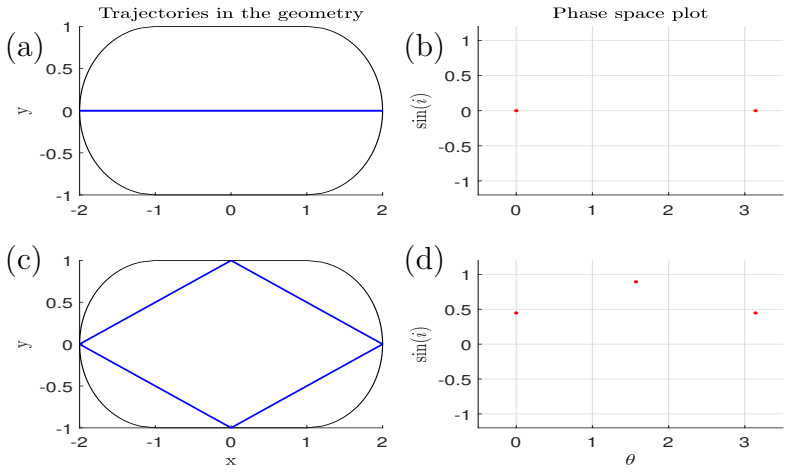

Figure 2.2: Two examples of stable orbits in the stadium billiard simulated with "*classorbits.m*" (see the supplementary materials [35]). (a)-(c) Trajectories in the physical space. (b)-(d) Phase space states corresponding to (a)-(c). More sophisticated examples are given in [33].

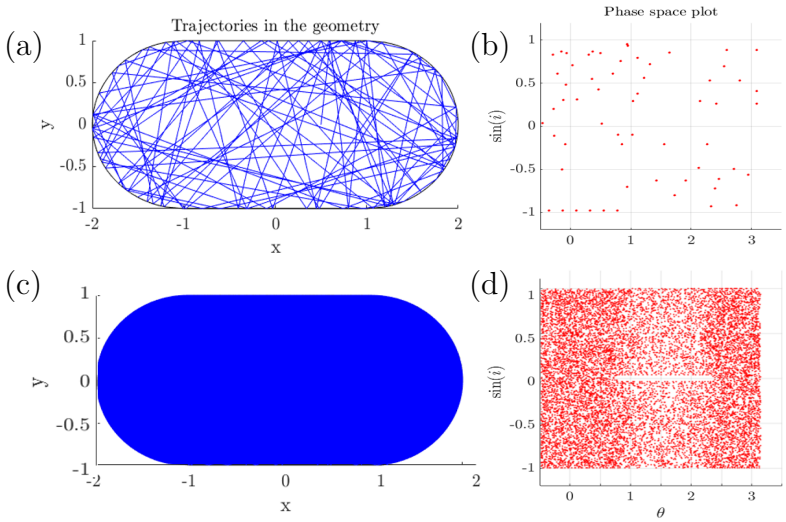

Figure 2.3: Growth of chaos inside the stadium billiard simulated with "*classorbits.m*". (a)-(c) Trajectories in the physical space. (b)-(d) Phase space states corresponding to (a)-(c).

Let us consider the discrete dynamical system :

$$(\theta_{n+1}, \sin(i_{n+1})) = \Psi(\theta_n, \sin(i_n)) \tag{2.2}$$

with Jacobian :

$$\mathbf{J}(\theta_n, \sin(i_n)) \tag{2.3}$$

Despite the existence of an infinite number of such orbits in the chaotic stadium geometry, it has been proven [36] that for one special kind of cyclically ordered orbits[1], they are hyperbolic (i.e. the Jacobian matrix $\mathbf{J}(\theta_n, \sin(i_n))$ contains one unstable eigenvalues $\lambda_1 < -1$ that implies an exponential sensitivity to even a tiny deviation from the initial conditions), and that their stable and unstable manifolds intersect transversely in the phase space. Hence the stadium billiard contains a Smale horseshoe in the phase space, typical for chaotic systems. [81] This fact is thought to also hold for any type of orbit. This property justifies the appellation *chaotic* for the stadium.

The *Lyapunov exponent* of a dynamical system is a quantity that characterizes the rate of separation of infinitesimally close trajectories. Quantitatively, two trajectories in phase space with initial separation vector $\delta\mathbf{Z}_0$ diverge at a rate given by :

$$|\delta\mathbf{Z}(t)| \approx e^{\lambda t}|\delta\mathbf{Z}_0| \tag{2.4}$$

Where λ is the Lyapunov exponent.

In our case, considering a normalized height of the stadium, we have chosen the normalized width $2a = 1$ leading to the maximum Lyapunov exponent, hence the most chaotic behaviour of the ball trajectories. [38]

[1] cyclically ordered orbits with exactly one point on a straight segment between each pair of points in different half circles, said *1-CO* orbit in short.

2.2 Scarring in the quantum world

Compared to the classical bouncing ball case, it was observed [5, 26, 29] that the electrons behaving in such geometry led to the apparition of *scars*, i.e. the concentration of the wave function about classical periodic orbits, as depicted in Figure 2.4. This highlights a completely different behaviour, where there is no more ergodicity in this chaotic geometry.

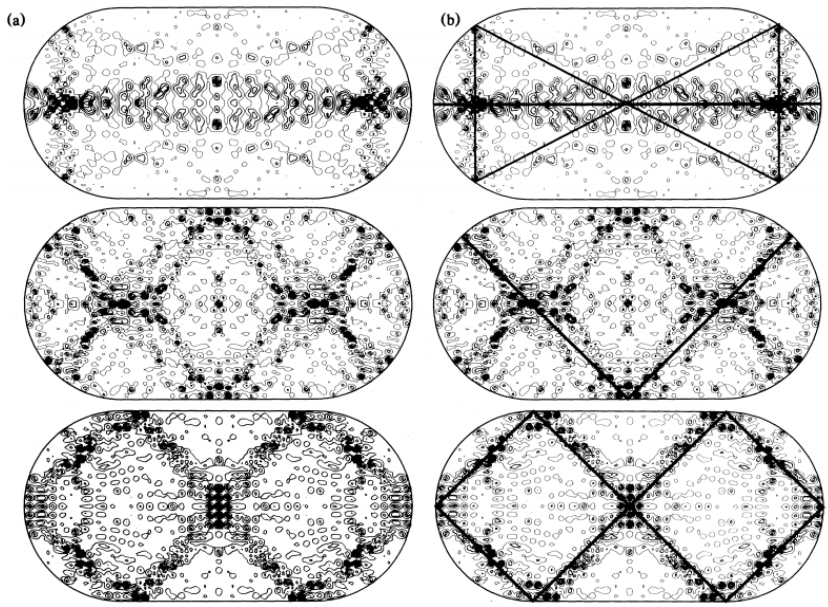

Figure 2.4: Simulated local density of states for electrons confined in a stadium billiard at different energies showing scarred states. Left column, three scarred states of the stadium; right column, the isolated, unstable periodic orbits corresponding to the scars. From [29].

Quantum and semiclassical analyses of the chaos present in the Bunimovich stadium are beyond the scope of this master thesis. The conclusions given by G. Tanner in [69] are still reported to avoid bad intuitive thoughts about the existence of quantum scars :
"The belief that the spectrum of the stadium billiard can be adequately described, semiclassically, by the Gutzwiller periodic orbit trace formula[2] [NB : a formula that approximates the density of states of a quantum system in terms of classical orbits] together with a modified treatment of the marginally stable family of bouncing-ball orbits [as in Figure 2.2] is shown to be erroneous. Unstable periodic orbits close to the marginally stable family in phase space cannot be treated as isolated stationary phase points when approximating the trace of the Green's function[3]. Semiclassical contributions to the trace show an $\hbar$-dependent transition from hard chaos to integrable behaviour for trajectories approaching the bouncing-ball orbits. A whole region in phase space surrounding the marginal stable family acts, semiclassically, like a stable island with boundaries being explicitly $\hbar$-dependent. The localized bouncing-ball states found in the billiard derive from this semiclassically stable island. The bouncing-ball orbits themselves, however, do not contribute to individual eigenvalues in the spectrum."

[2]the quantum spectral determinant is written as $D(E) = \exp \int_0^E dE' TrG(E') = \Pi_n(E - E_n)$ where $G(q, q', k) = G_{bb}(q, q', k) + G_r(q, q', k)$ is a Green's function divided into a bouncing-ball part and the rest. The complete Gutzwiller trace formula is given in [7].

[3]a Green's function is the impulse response of an inhomogeneous linear differential operator defined on a domain with specified initial conditions or boundary conditions. In this case, the operator gives the spectrum of the stadium billiard as a function of the initial and final positions in the phase space q and q' and the wavenumber k.

Chapter 3

State of the art on walkers

Faraday discovered in 1831 that, above a critical acceleration threshold γ_F, stationary waves can appear on the surface of a liquid shaken with an acceleration $\gamma = \gamma_m \cos(\omega_0 t)$. This phenomenon depicted in Figures 3.1 and 3.2 has been called the *Faraday instability*. The produced waves are subharmonic, with half the frequency of the vibrational forcing $\omega_F = \omega_0/2$. The wavelength k_F of these waves can be deduced from the usual dispersion relation of waves at the surface of a fluid which links the pulsation ω_F to the wavevector k_F. In case of gravity-capillary waves, the dispersion relation becomes [58] :

$$\omega_F^2(k_F) = \left(\frac{\omega_0}{2}\right)^2 = \left(gk_F + \frac{\sigma}{\rho}k_F^3\right) tanh(k_F h_0) \tag{3.1}$$

Where g is the gravitational acceleration constant, σ, ρ, h_0 are the surface tension, mass density and height of the liquid, respectively.

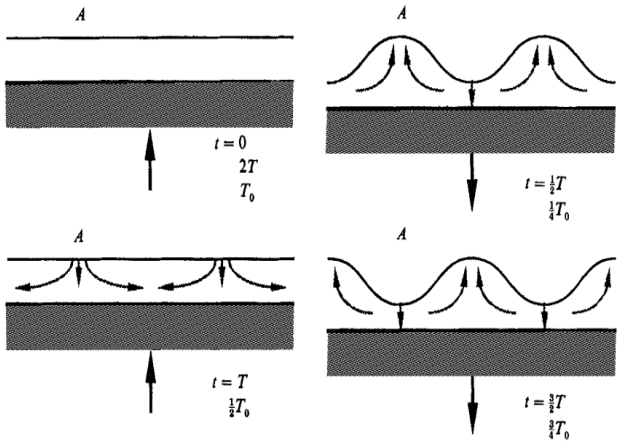

Figure 3.1: Liquid movement initiation converging to Faraday waves. Taken from [13].

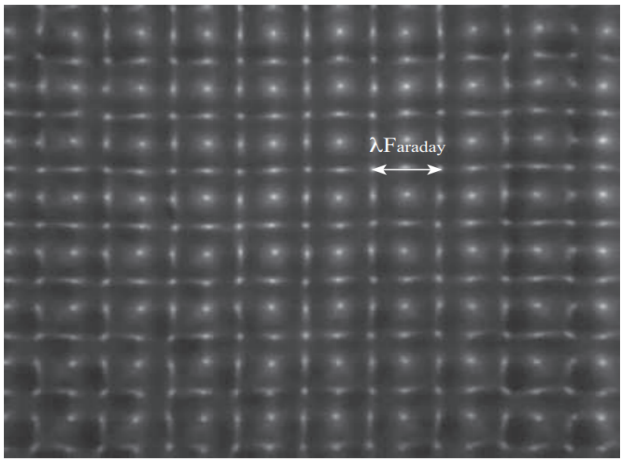

Figure 3.2: Top view of the Faraday instability. Taken from [59].

If a viscous liquid is sinusoidally vibrating along the vertical axis below the acceleration threshold (or Faraday threshold), i.e. $\gamma_m < \gamma_F$, the equilibrium configuration of the liquid surface is to be plane. If at an initial instant, the surface is disturbed, this disturbance is propagated as a wave (see examples in Figure 3.3) that decays with a certain characteristic time τ [19]. As shown in Figure 3.4, this time τ directly depends on the vertical acceleration of the liquid bath. For an acceleration $\gamma_m > \gamma_F$ above the instability threshold, a initial perturbation at the liquid surface will be amplified until reaching a saturation amplitude which depends on γ_m.

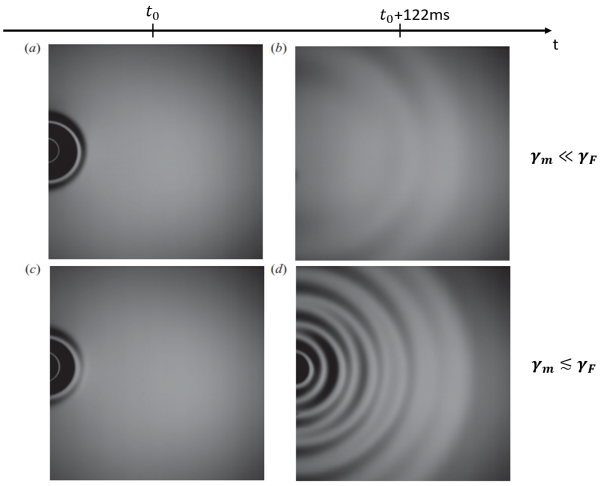

Figure 3.3: a), b) Non-vibrated bath case : a) Dropping of a steel ball, b) observation of a capillary gravitational wave. c), d) Case of a bath vibrated slightly under the Faraday threshold $\frac{\Gamma_F}{\Gamma_F - \Gamma} = 100$: c) Dropping of a steel ball, d) The capillary gravitational wave has excited the Faraday modes : a Bessel function centered at the impact point is observed. Adapted from [19].

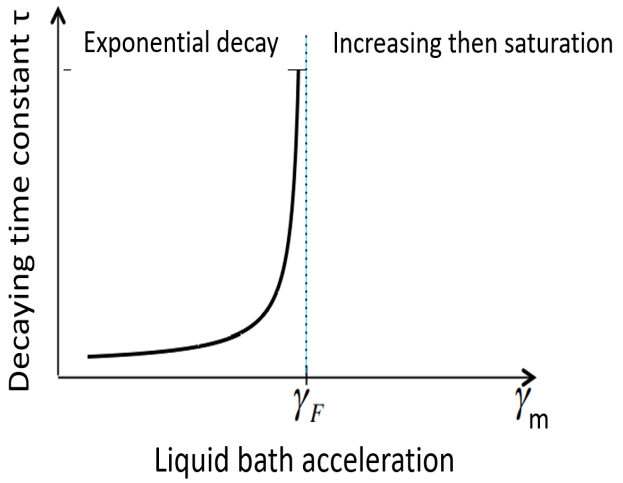

Figure 3.4: Decay time τ of an initial disturbance as a function of the γ_m acceleration in the vicinity of the Faraday threshold. The damping time of a disturbance diverges at the Faraday instability theshold. Adapted from [56].

In 2004, C-H Gautier, supervised by E. Fort and Y. Couder from Paris-Diderot university discovered that it was possible for a droplet to bounce indefinitely on the surface of a liquid bath oscillating vertically. Under certain conditions, this droplet can spontaneously move horizontally under the influence of the wave it generated itself. These two possible modes for a droplet have led to the names *bouncing* and *walking* droplet (or *walker*). Since this discovery, research laboratories (mainly at MIT, Paris VII and ULiège) focused their efforts in the understanding of this rich dynamical system, exhibiting many features of low-dimensional chaotic oscillators. One key feature that raised the attention on these walkers is that they represent the first known example of a macroscopic pilot-wave system, and exhibit behaviours thought to be exclusive to the microscopic quantum realm such as self-organising lattice structures, single particle diffraction, quantized orbits, orbital level splitting, tunneling effects, and wave-like statistics in confined geometries.

As under the Faraday threshold, all the perturbations undergo an exponential decay with time constant τ, τ is considered as representative of the *memory* of the system. We "adimensionalize" it with the Faraday period to define the *memory* parameter :

$$Me = \frac{\tau}{T_F} \tag{3.2}$$

Where T_F is the Faraday period. With the definition of eq. (3.2), if we consider such a *walker* which bounces in phase with the Faraday period T_F, the memory parameter Me can be interpreted as the number of previous droplet bounces whose generated waves are still present inside the current liquid surface profile when the droplet bounces again.
The Faraday instability is a Hopf bifurcation [80], whose theory shows that the *distance to Faraday threshold* $\mathcal{M}$ evolves as :

$$\mathcal{M} = \frac{\gamma_F}{\gamma_F - \gamma_m} = \frac{\Gamma_F}{\Gamma_F - \Gamma} \tag{3.3}$$

In 2018, Gilet and his associates [68] proved that the *memory* parameter is directly proportional to this *distance to Faraday threshold* and can be approximated as :

$$Me = \frac{\mathcal{M}}{2\pi\gamma_0}\left(1 + \frac{\gamma_0^{1/2}}{2} + \frac{\gamma_0}{4}\right) \tag{3.4}$$

Where γ_0 is the bath acceleration amplitude leading to $k = k_0$ such that $\Gamma_F \to 0$ and $\omega_F^2 = \omega_{k_0}^2 = 1$ (see eq. (3.1)) in the limit of vanishing viscosity ν. [68]

In the case where the acceleration of the bath γ_m is weak compared to the Faraday acceleration, the memory time τ is weak and the standing wave attenuates quickly. Otherwise, the standing wave survives a certain period of time, τ defining a measure of this persistence time.

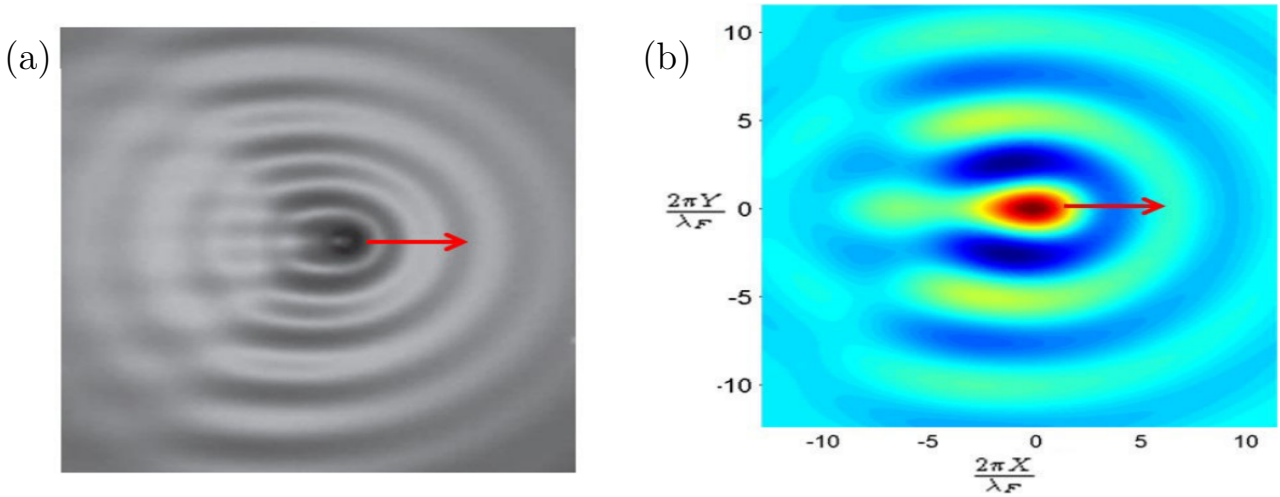

Figure 3.5: (a) Experimental image of a walker and its wave field with $\mathcal{M} = 55$ taken from [19]. (b) Simulated wave field taken from [34].

A prediction for an approximate value of Γ with which we need to shake the bath so as to observe neutrally stable surface waves, (a.k.a. the Faraday instability Γ_F) for a given wavenumber k is given in [63] :

$$\Gamma^2 = \frac{4}{g^2k^2}\left[\left(2\nu k^2 + i\frac{\omega_0}{2}\right)^2 + k\left(-g + \frac{\sigma}{\rho}k^2\right)\right]\left[\left(2\nu k^2 - i\frac{\omega_0}{2}\right)^2 + k\left(-g + \frac{\sigma}{\rho}k^2\right)\right] \tag{3.5}$$

Mixing eq. (3.1) with eq. (3.5) allows to determine the Faraday waves' configuration (ω_F, k_F, Γ_F) for a given liquid with a given frequency of forcing f_0.

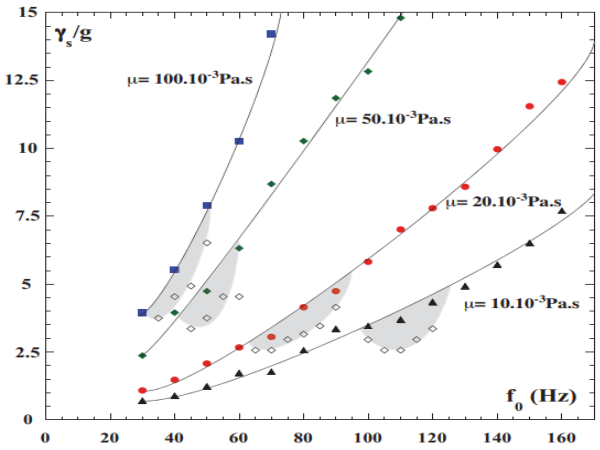

Figure 3.6: (f, Γ) curve for different viscosity values. The walking regimes are colored in light blue. Taken from [59].

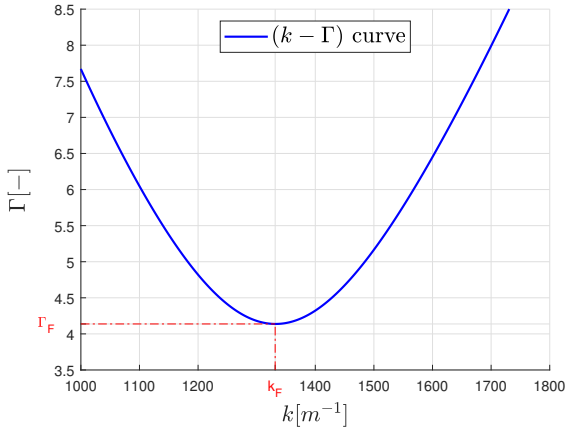

Figure 3.7: Obtained $(k - \Gamma)$ curve applying eq. (2.32) in [68] for the values given in Table 1. The Faraday instability appears at the wavenumber k_F for which the acceleration limit is the lowest $\frac{\partial \Gamma}{\partial k}\Big|_{k_f} = 0$.

This introduction served to point out the possibility for droplets to bounce indefinitely on a sinusoidally oscillating liquid bath and the main quantities that have to be controlled in order to choose the evolution of these droplets, namely the height of the liquid h_0 and more importantly the amplitude γ_m and frequency f_0 of the forcing. It is the intrinsic wave-particle duality of this interacting droplet-surface wave system that motivated the analysis of the droplets' behaviour in a confined chaotic geometry in order to make comparisons with existing electronic transport experiments and simulations.

3.1 Modeling the walking droplet pilot-wave system

To derive a good mathematical model of the wave-particle dynamics of the walking droplet is essential to compare with experimental results, understand the physical mechanisms yielding a given observation and furthermore make predictions. In the last 15 years, different analytical models have been proposed in the literature to describe this particular pilot-wave system, ranging from simpler to more sophisticated ones. In this section, the evolution from simple approximate models to more evolved complex ones is described in details, with some intermediate model examples whose pros and cons are discussed. In these models, three interdependent dynamics have to be taken into account, the liquid surface **wave dynamics** and the **vertical** and **horizontal droplet dynamics**. As they will be regularly mixed, it is important for the reader to identify to which of these three dynamics do the following descriptions and equations belong.
The various deformations modes of these droplets have been carefully analyzed in [12, 88]. However, with an Ohnesorge number (adimensional number characterizing the ratio between the viscous forces and both the inertia and surface tension) $Oh \in [0.175 - 0.3] \sim 1$, and $f < f_c$ as shown in Table 1, the droplet will generally be considered to remain perfectly spherical in good approximation. Exceptions to this assumption will consider up to the first two spherical harmonics. Finally, most of the described models contain lots of parameters whose values are not necessarily given if it does not contribute to additional information in their understanding.

As a simple first model, one can mention the inelastic ball on a sinusoidally oscillating plate given in [59, 60]. In this model, the surface of the liquid is considered as a rigid plate and assumed to perfectly follow the actuation hence its height only varies with time. The surface

height is independent from the droplet and constant everywhere :

$$z_{plate} = A\cos(\omega t) \tag{3.6}$$

Where the ball takes off when the acceleration is :

$$\gamma_{plate}(t_0) = \frac{d^2 z_{plate}}{dt^2}(t_0) = -A\omega^2\cos(\omega t_0) = -g \tag{3.7}$$

Between two bounds on the plate, the droplet follows a parabolic trajectory given by :

$$z(t) = z_0 + v_0(t - t_0) - \frac{1}{2}g(t - t_0)^2 \tag{3.8}$$

With :

$$\begin{cases} t_0 = \frac{1}{\omega} arcos(\frac{g}{A\omega^2}) \\ v_0 = A\omega\sqrt{1 - \frac{g^2}{A^2\omega^4}} \\ z_0 = \frac{g}{\omega^2} \end{cases} \tag{3.9}$$

The height reached by the droplet corresponds to the maximum of the parabolic trajectory :

$$h = z_0 + \frac{v_0^2}{2g} = \frac{g}{2\omega^2}\left[1 + \left(\frac{\gamma_m}{g}\right)^2\right] \tag{3.10}$$

The vertical behaviours of bouncing droplets are shown in Figures 3.8 and 3.9. In both figures, the upper line corresponds to the droplet's trajectory while the lower one corresponds to the liquid surface. From this point, it is useful to introduce the notion of bouncing mode. Let us define the pair (m, n) where $m/(f/2)$ represents the half period of the bouncing mode (i.e. the number of elapsed half periods of vertical oscillations), during which the drop contacts the surface n times.

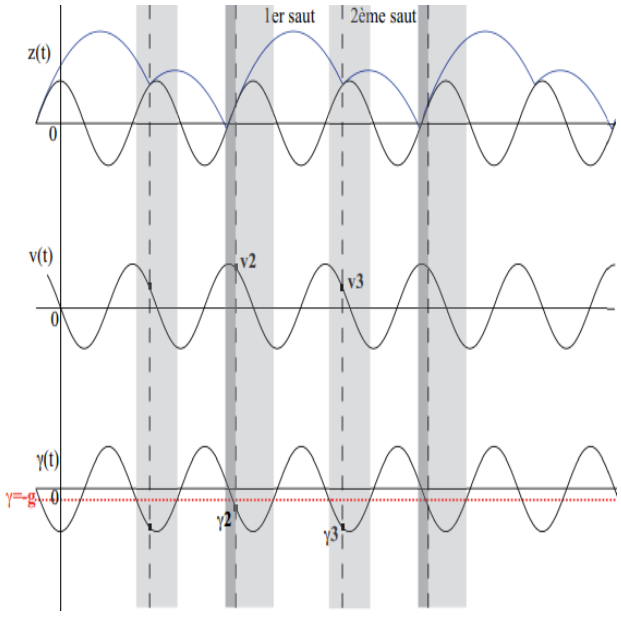

Figure 3.8: Spatiotemporal simulation of the vertical dynamics of a bouncer using eq. (3.8) and eq. (3.9), taken from [59].

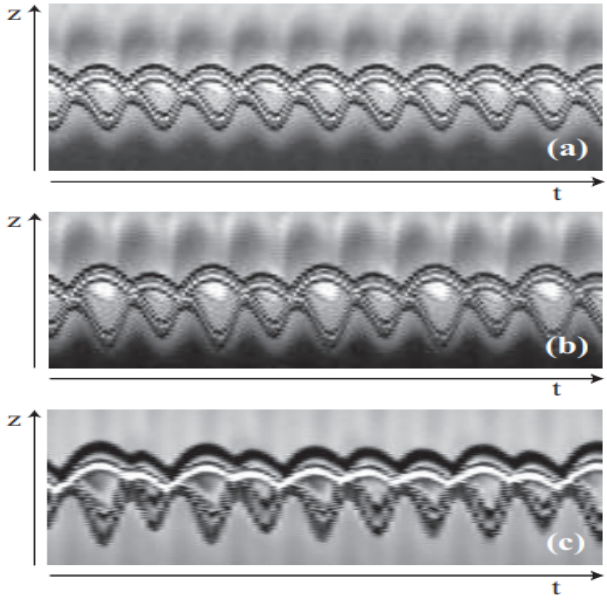

Figure 3.9: Three spatiotemporal images showing the vertical behaviour of a bouncing droplet. (a) Simple bouncing in $(1, 1)$ mode. (b) Period doubling in $(2, 2)$ mode. (c) chaos in the bouncing mode. Taken from [59].

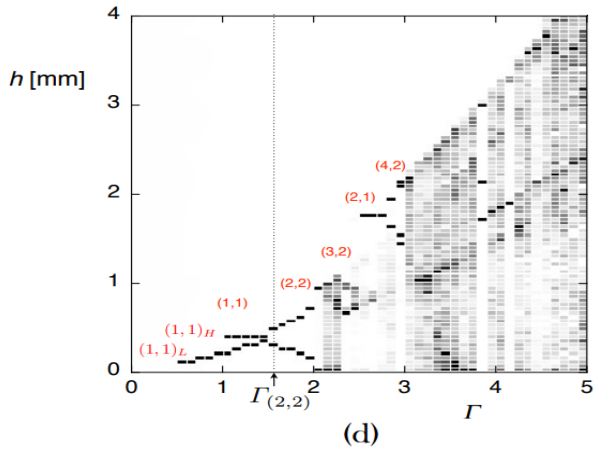

Figure 3.10: Bifurcation diagram of the different vertical heights reached by the droplet for various accelerations Γ obtained by simulation. The bouncing modes (m, n) are given in red. Taken from [71].

Regarding the horizontal dynamics, the model is based on Newton's law and takes two forces into account :

$$m\ddot{x} = \underbrace{F^b \sin\left(2\pi \frac{\dot{x}}{V_F^\phi}\right)}_{Propulsion} - \underbrace{f^\nu \dot{x}}_{Drag} \tag{3.11}$$

Where :

$$f^\nu \approx \frac{\mu_a s}{h_f} \frac{\tau}{T_F} \tag{3.12}$$

is the effective damping, taking into account the viscosity of the air μ_a, the surface of contact between the droplet and the bath $s \sim 1[mm^2]$, the typical thickness of the air film $h_f \sim 2[\mu m]$. [59] And :

$$F^b \approx m\gamma_m \frac{A_F}{\lambda_F} \frac{\tau}{T_F}[N] \tag{3.13}$$

is a first order approximation for the effective force, proportional to the vertical acceleration γ_m, the slope of the wave at the impact location $\frac{A_F}{\lambda_F}$ and the duration of collision over one period $\frac{\tau}{T_F}$. By looking for steady regime ($\ddot{x} = 0$) solutions of eq. (3.11) and considering a 3^{rd} order Taylor approximation of the first term in the right hand side, the authors obtain two stable solutions : $V_w = \pm V_F^\phi \frac{\sqrt{6}}{2\pi}\sqrt{(F^b - F_c^b)/F^b}$. This result introduces a forcing acceleration threshold F_c^b for which the droplet leaves the bouncing mode and starts walking.

Despite the simplicity of this model, it already captures three important features : the existence of the walking regime, a duration of contact between the droplet and the wave and the existence of chaotic vertical dynamics as the vertical acceleration increases as depicted in Figure 3.10. However, it has many defaults that make it wrong. It neglects the deformation of the droplet, the energy loss due to air and due to contact with the liquid surface, the influence of the droplet on the liquid surface hence the interactions between multiple droplets and more generally all the fluid mechanics aspects.

In 2013, ref. [71] built model based on two masses m_1 and m_2 linked by a spring of stiffness k in parallel to a dashpot with a damping coefficient c. The authors added the contribution of energy loss during contact with the liquid surface, with σX^2 being the *surface energy* where X is the horizontal length increment of the droplet's diameter at impact wrt its diameter in fly.

In 2015, ref. [21] added the effect of the droplets on the liquid surface by proposing a linear combination of spatio-temporally damped sine waves whose centers are the positions of the previous impacts of all the droplets on the surface :

$$u^i_{n+1} - u^i_n = -f^\nu u^i_n - \frac{\partial}{\partial s}\left(C_0\xi^{ii} + C_1\sum_{j\neq i}\xi^{ij}\right)\Bigg|_{n+1} \tag{3.14}$$

With :

$$\xi^{ij}(s^i_{n+1}, t) = \xi_0 \sum_{p=-\infty}^{n} \cos\left(\frac{2\pi(s^i_{n+1}(t) - s^j_p)}{\lambda_F}\right)\exp\left(-\frac{s^i_{n+1}(t) - s^j_p}{\delta}\right)\exp\left(-\frac{t - t^j_p}{\tau}\right) \tag{3.15}$$

Where u^i_{n+1} is the speed of droplet i after its $(n+1)$-th impact, and s^i_{n+1} is its position in the 1D string space, ξ^{ij} is the height of the wave created by the impacts of droplet j at droplet i's position, δ is a viscous length, τ is the memory time, f^ν is a dissipation parameter and C_0, C_1, ξ_0 are scaling coefficients.

For the following models, it is useful to introduce the concept of *Hypothetical surface*. [63] The hypothetical surface is obtained by computing the surface evolution without applying the pressure of the ongoing impact. This auxiliary surface will in fact have two uses. The first is to calculate droplet penetration inside the wave field to deduce the pressure field that will affect the droplet's motion and the second is to obtain the gradient at the point of contact, yielding the horizontal component of the wave force.

In reference [48], the vertical dynamics is described by an ordinary differential equation, modeling the interaction between the droplet and fluid bath as a linear spring.
The crucial assumption underlying this model is that, each time the drop strikes the vibrating bath, the disturbances created by its previous impacts have decayed sufficiently to be negligible. It was assumed that any distortions and internal motions of the drop have decayed enough s.t. we can approximate the drop at impact as being spherical and in rigid-body motion. The condition for this assumption to be valid can be written as :

$$Oh > \frac{\Omega}{4\pi} \tag{3.16}$$

Unfortunately, the linear spring models do not provide satisfactory quantitative agreement with the experiments, they although allow to obtain an analytic expression for the drop motion during both flight and contact. "It is thus only necessary to obtain numerically the points of first impact and detachment; the motion in between can then be calculated with great speed, which makes it possible to obtain qualitatively correct regime diagrams with great resolution".

Later in reference [48], as well as in [49, 88, 89], on the other hand, the vertical dynamics is described by an ODE, here modeling the interaction between fluid bath and drop as a logarithmic spring. The model has been derived assuming a small *Weber number* (see Table 1) $We \ll 1$, which indicates that the inertial forces are small compared to surface tension forces, and means that the impact dynamics is slow compared to the surface wave dynamics. It was derived using a variational approach by assuming a quasi-static form for both the drop and interface shapes during impact. In this model, the air drag is proved negligible in front of the others contributions and is thus discarded [49].
The vertical dynamics equations are written in two parts :

$$\begin{cases} m\ddot{z} = -mg^*(t) & \text{in free flight } (\mathcal{Z} \geq 0 \text{ or } F_N \leq 0) \\ \left(1 + \frac{c_3}{ln^2|\frac{c_1 r_0}{\mathcal{Z}}|}\right) m\ddot{z} + \frac{4}{3}\frac{\pi\mu r_0 c_2(\nu)}{ln|\frac{c_1 r_0}{\mathcal{Z}}|}\dot{\mathcal{Z}} + \frac{2\pi\sigma\mathcal{Z}}{ln|\frac{c_1 r_0}{\mathcal{Z}}|} = -mg^*(t) & \text{during contact} \end{cases} \tag{3.17}$$

where m is the droplet mass, z is its center of mass vertical position and $\mathcal{Z} = z - h$ is the height of the drop above the bath surface, $g^*(t) = g + \gamma \sin(\omega t)$ is the effective gravitational acceleration in the vibrating bath frame of reference, $F_N = m\ddot{z} + mg^*(t)$ is the normal component of the reaction force acting on the drop and the three coefficients c_0, c_1, c_2 were fixed using experimental data.
During contact, the drop feels a reaction force dependent on $\mathcal{Z}$, as well as a drag dependent on the relative speed of the drop and bath $\dot{\mathcal{Z}}$. This nonlinearity due to logarithmic correction has the effect of reducing dissipation and prolonging contact for smaller impact speeds. There is also a correction to the drop inertia coming from the drop's internal fluid motion.

Next we introduce to the models based on Navier-Stokes equations. We associate a cartesian frame (x, y, z) centered at the liquid surface at rest in the center of the bath. $z = 0$ thus corresponds to the liquid surface at rest and $z < 0$ corresponds to the liquid contained in the bath under the surface. The wave model in eq. (3.25), representative of the global form of the wave contribution induced by one impact [2, 49, 63, 68], has been obtained starting from the Navier-Stokes equations by considering silicone oil to be an incompressible fluid with velocity $\vec{u} = [u_x, u_y, u_z]^T$, uniform density ρ and small waves amplitude wrt the characteristic wavelength and boundary layer thickness.
We consider an asymptotic decay :

$$\vec{u} \xrightarrow{z->-\infty} 0 \tag{3.18}$$

Asymptotic considerations that suit the typical set up for bouncing droplet experiments lead to the following linearized system :

$$\begin{cases} \frac{\partial \vec{u}}{\partial t} = \vec{g} - \frac{\Delta p}{\rho} + \nu \Delta \vec{u} \\ \nabla \cdot \vec{u} = 0 \end{cases} \tag{3.19}$$

with the fluid initially occupying the negative half-space, i.e. in :

$$D = \{(x, y, z); z < 0\} \tag{3.20}$$

subject to the linearized kinematic boundary condition :

$$\frac{\partial \eta}{\partial t} = u_z \tag{3.21}$$

and the linearized dynamic boundary conditions :

$$\begin{bmatrix} 0 \\ 0 \\ \sigma\kappa\eta - p_d \end{bmatrix} = \begin{bmatrix} \rho\nu(\frac{\partial u_x}{\partial z} + \frac{\partial u_z}{\partial x}) \\ \rho\nu(\frac{\partial u_y}{\partial z} + \frac{\partial u_z}{\partial y}) \\ -p + 2\rho\nu\frac{\partial u_z}{\partial z} \end{bmatrix} \tag{3.22}$$

on :

$$\partial D = \left\{(x, y, z) \in \mathbb{R}^3; z = 0\right\} \tag{3.23}$$

In particular, it is with this starting point that the dispersion relation in eq. (3.1) is derived.
To consider the two-dimensional horizontal drop motion, the total height of the standing waves in the bath frame of reference is written as $h(\mathbf{r}, t)$ with $\mathbf{r} = [x, y]^T$. It is shown that it can be expressed as the sum of contributions from all previous impacts:

$$h(\mathbf{r}, t) = \sum_{n=1}^{N} h_0(\mathbf{r}, \mathbf{r}_n, t, t_n) \tag{3.24}$$

Where the contribution $h_0(\mathbf{r}, \mathbf{r}_n, t, t_n)$ resulting from a single drop impact at $(\mathbf{r}, t) = (\mathbf{r}_n, t_n)$ is approximated, in the long-time limit, by a standing wave decaying exponentially in time with a spatial profile prescribed by a zero-th order Bessel function of the first kind, $J_0(x)$ (see developments in [49]):

$$h_0(\mathbf{r}, \mathbf{r}_n, t, t_n) \approx \sqrt{\frac{2}{\pi}} \frac{k_F R_0}{3k_F^2 R_0^2 + \mathcal{B}o} \frac{R_0 k_F^2 \mu_{\text{eff}}^{1/2}}{\sigma} \frac{cos(\pi f t)}{\sqrt{t - t_n}} \left[\int F_N(t') \sin(\pi f t') dt' \right] \\ \text{x } \exp\left(\left[\frac{\Gamma}{\Gamma_F} - 1 \right] \frac{t - t_n}{T_d} \right) J_0(k_F |\mathbf{r} - \mathbf{r}_n|) \tag{3.25}$$

Where the wavenumber at contact k_C has directly been approximated by k_F, μ_{eff} accounts for an effective viscosity and $\mathbf{r}_n$ and t_n are taken as the weighted averages of $\mathbf{r}$ and t over the contact time t_C :

$$\mathbf{r}_n = \frac{\int_{t_C} F_N(t') \mathbf{r}(t') dt'}{\int_{t_C} F_N(t') dt'}, \qquad t_n = \frac{\int_{t_C} F_N(t') t' dt'}{\int_{t_C} F_N(t') dt'} \tag{3.26}$$

The liquid surface height from eq. (3.25) is depicted in Figure 3.11.

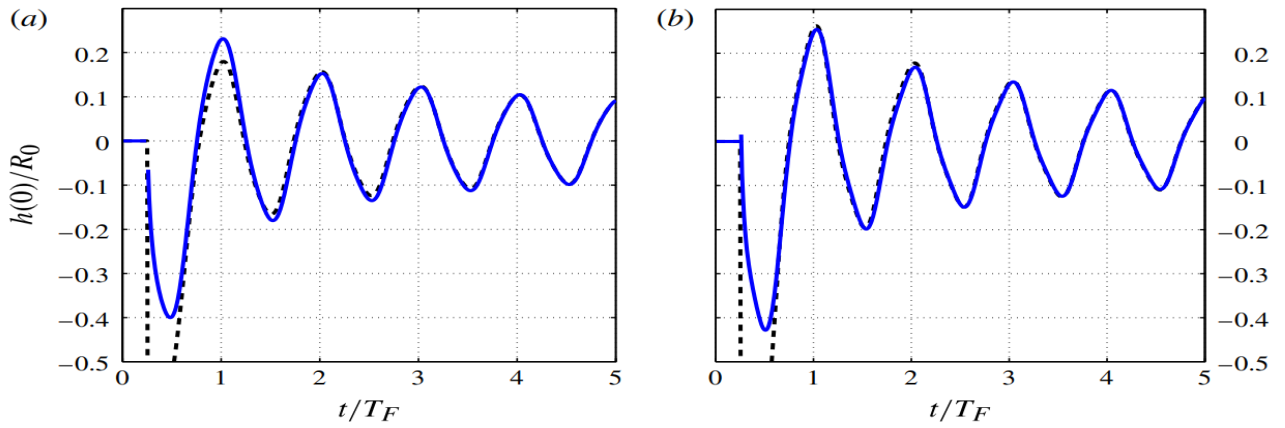

Figure 3.11: Full (dashed line) and long-term approximation (solid line) numerical models predictions of the dimensionless height of the surface $\frac{h(0,\tau)}{R_0}$ as a function of time non-dimensionalized by T_F for (a) 20 [cSt] oil at 80 [Hz] and (b) 50 [cSt] oil at 50 [Hz]. The surface is forced at $t = T_F/4$ and then evolves freely. Taken from [49].

Note that treating fluid as being of infinite depth is a valid approximation for depths greater than half a wavelength, as is typically the case in the experiments of interest. [2]

In 2018, reference [68] showed that the single impact of a small droplet leads to a wave dynamics solution of the form :

$$h(r, t) \approx B_F^+(t_i) k_F \sqrt{\frac{\pi}{D(t - t_i)}} \cos(t + \theta_F^+) J_0(k_F r) \exp\left[-\frac{t - t_i}{2\pi M e} - \frac{r^2}{4D(t - t_i)} \right] \tag{3.27}$$

Where t_i is the impact time instant, $J_0(\,\cdot\,)$ is the zero-th order Bessel function of the first kind, $r = |\mathbf{r}|$ being the distance to the impact with $\mathbf{r} = [x - x_i, y - y_i]^T$ and we assume $t - t_i > 0$ and $k_F r \ll 1$ or $k_F r \gg 1$.
The main additions highlighted by ref. [68] wrt eq. (3.25) are (i) the phase shift θ_F^+ between the impact and the resulting wave, (ii) a diffusive spreading in the exponential decay (diffusion coefficient D) and (iii) a well-defined amplitude B_F^+ that depends on the impact phase τ_i in eq. (2.50) of the same paper.

The extension of this solution to derive the surface waves emitted by a walker assuming the walker lies in the $(m, n) = (1, 1)$ mode and moves in a straight line at constant speed V_w is also

described in ref. [68] and yields the results depicted in Figure 3.12. In the limit of small walking speed and low memory ($2\pi Mek_F v \ll 1$), the following analytical solution can be obtained :

$$h_w(\mathbf{r},t) = \frac{B_F^+ k_F}{\sqrt{v^2 + \frac{2D}{\pi Me}}} \cos(t+\theta_F^+) J_0\left(k_F \left|\mathbf{r} + \frac{r}{\sqrt{v^2+\frac{2D}{\pi Me}}}\mathbf{v}\right|\right) \exp\left[-r/l(\theta)\right] \tag{3.28}$$

Where the term inside the Bessel function $J_0(\,\cdot\,)$ takes into account a Doppler effect in the walking regime, which grows with higher speeds v. This Doppler effect implies that the wavelength will appear slightly smaller than λ_F ahead of the droplet and slightly larger behind it, as shown in Figure 3.18.

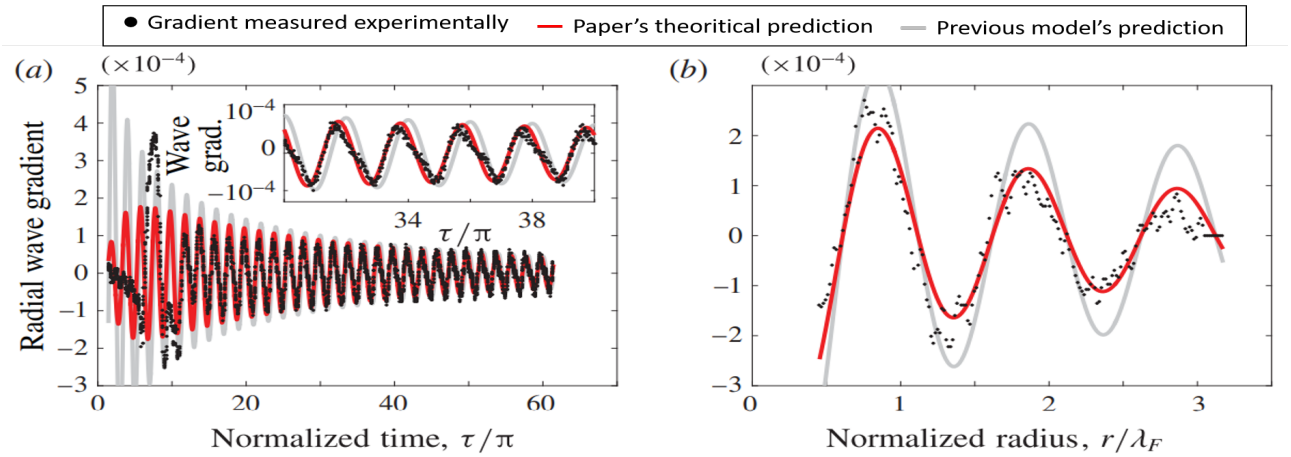

Figure 3.12: Radial gradient of surface waves, (a) versus time at a fixed distance $r = 1.32$ [cm] from the impact, and (b) versus position at a fixed time, $t = 0.233$ [s] after impact. The present model (red curve) predicts a phase shift of $+\pi/4$ between the Faraday waves and the forcing signal, which is in better agreement with experiments than previous models (grey curve). Results obtained in [68].

With a reasoning similar to the one given for the first model presented in this section, ref. [49] was able to obtain an approximation to the walking memory threshold Me^c :

$$Me^c = \left[\frac{5\sqrt{2}\pi \sin(\Phi_i)(k_F R_0)^5}{6(3k_F^2 R_0^2 + \mathcal{B}o)}\sqrt{\frac{\mu_{eff} g^2 T_F^3}{\sigma R_0}}\right]^{-2/3} \tag{3.29}$$

where a $(m,n) = (2,1)^2$ bouncing mode is considered and a constant horizontal speed. Φ_i is the phase of impact. A normalized acceleration threshold Γ_W can then be obtained from eq. (3.29) and eq. (3.4).

Finally, assuming the droplet to be in resonance with the bath, i.e. it is bouncing periodically in the vertical direction with period $T = \frac{4\pi}{\omega}$ (i.e. bouncing period is double of the forcing period). the horizontal dynamics equation is :

$$m\ddot{\mathbf{x}} + D(t)\dot{\mathbf{x}} = -\overline{\nabla h(\mathbf{x},t) F_N(t)} \tag{3.30}$$

Where $D(t) = C\sqrt{\rho R_0/\sigma} F_N(t) + 6\pi R_0 \mu_a$ is the total instantaneous drag coefficient and C is the proportionality constant for the tangential drag force. The first term of $D(t)$ represents the momentum drag induced during impact and the second term represents the aerodynamic drag due to air friction induced during flight. The overlining on the right hand side means that we take the time average of the term over one period T.

In 2017, reference [15] added the possibility to handle an external potential field $\mathcal{V}(\mathbf{x}(t),t)$ in the droplet's horizontal dynamics (e.g. a harmonic potential, but still considering an infinitely large space in the horizontal plane thus no reflections of the waves). The droplet dynamics writes here as :

$$\begin{aligned} m\ddot{\mathbf{x}}(t) + D(t)\dot{\mathbf{x}}(t) &= -\nabla\mathcal{V}(\mathbf{x}(t),t) - \overline{\nabla h(\mathbf{x},t)F_N(t)} \\ m\ddot{\mathbf{z}}(t) + c_{St}\dot{\mathbf{z}}(t) &= -mg_\Gamma(t) + F_N(t) \end{aligned} \tag{3.31}$$

Where the air friction was also considered for the vertical dynamics with $c_{St}\dot{\mathbf{z}}(t)$.
Taking $\mathcal{V} = \frac{1}{2}\kappa|\mathbf{x}(t)|^2$ (resp. 0) for dynamics in a harmonic potential well (resp. free walking dynamics), the authors obtain the following dimensionless system :

$$\begin{aligned} 0 &= \mathcal{L}_k a_m(t;k), && \forall t \neq t_n \\ 0 &= \mathcal{L}_k b_m(t;k), && \forall t \neq t_n \\ \mathbf{0} &= \mathbf{X}^{"}(t) + \tilde{\nu}_p\mathbf{X}^{'}(t) + \tilde{\kappa}\mathbf{X}(t), && \forall t \neq t_n \\ \left[a_m^{'(t_-;k)}\right]_-^+ &= -P_m(k)\Phi_m(\mathbf{X}(t_n);k) \\ \left[b_m^{'(t_-;k)}\right]_-^+ &= -P_m(k)\Psi_m(\mathbf{X}(t_n);k) \\ \left[\mathbf{X}^{'}(t_n)\right]_-^+ &= -F(c)\left(\tfrac{1}{c}\sqrt{\tfrac{B}{R}}\nabla\eta(\mathbf{X}(t_n),t_n) + \mathbf{X}^{'}(t_n^-)\right) \end{aligned} \tag{3.32}$$

Discretizing the harmonic potential well problem yields the following algorithm for the horizontal dynamics numerical simulation:

Algorithm 1

1. Use $\mathbf{X}_n$ and $\mathbf{X}_n^{'}$ to compute $\mathbf{X}_{n+1}$ and $\tilde{\mathbf{X}}^{'} = \mathbf{X}^{'}(t_{n+1}^{'})$:

$$\begin{bmatrix} \mathbf{X}_{n+1} \\ \tilde{\mathbf{X}}^{'} \end{bmatrix} = \mathbf{F}(\tilde{\kappa}) \begin{bmatrix} \mathbf{X}_n \\ \mathbf{X}_n^{'} \end{bmatrix} \tag{3.33}$$

2. Update wave amplitudes including jump conditions $\forall k > 0$ (similarly for $\mathbf{b}_n(k)$):

$$\begin{bmatrix} \mathbf{a}_{n+1}(k) \\ \mathbf{a}_{n+1}^{'}(k) \end{bmatrix} = \mathbf{M}_k(\Gamma) \begin{bmatrix} \mathbf{a}_{n+1}(k) \\ \mathbf{a}_{n+1}^{'}(k) \end{bmatrix} - \begin{bmatrix} \mathbf{0} \\ \mathbf{P}(k)\Phi(\mathbf{X_{n+1}};\mathbf{k}) \end{bmatrix} \tag{3.34}$$

3. Apply droplet jump conditions:

$$\mathbf{X}_{n+1}^{'} = (1 - F(c))\tilde{\mathbf{X}}^{'} - \frac{F(c)}{c}\sqrt{\frac{B}{R}}\nabla\eta(\mathbf{X}_{n+1},t_{n+1}) \tag{3.35}$$

Reference [39] proposed a model allowing simulations of walkers in a variable topography, i.e. with the liquid depth varying in space. The authors managed to simulate the reflection of a walking droplet arriving at a deep-shallow water interface, as shown in Figure 3.13.

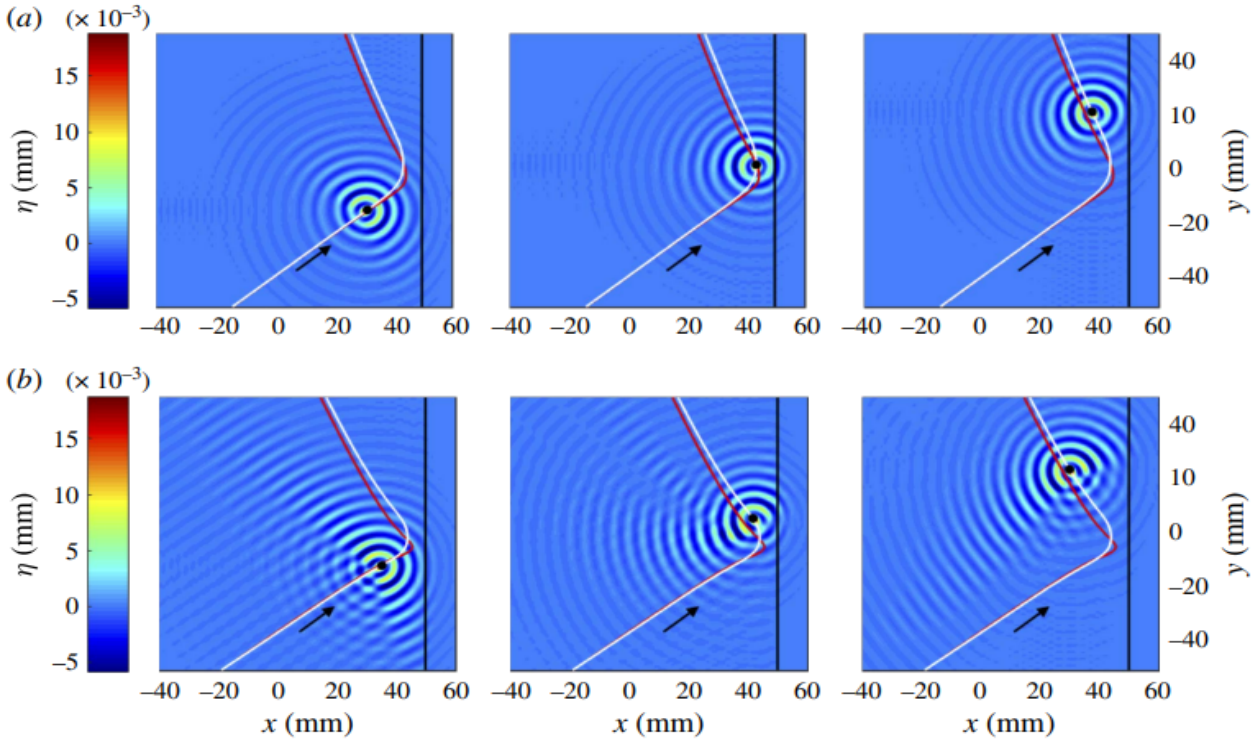

Figure 3.13: Wave amplitude (contour plot) and trajectories (white line) for wall reflection. The red line represents the corresponding experimental data. (a) $\Gamma/\Gamma_F = 0.90$, (b) $\Gamma/\Gamma_F = 0.99$. From [39].

An overview of the current state of the art regarding the mathematical modelling of the walking droplet pilot-wave system dynamics was given. Despite numerous improvements in the models reliability, obtaining and explanation of some experimentally observed phenomena such as the bouncing and walking regime, Doppler effect, orbital and promenade pairs, double quantization for a droplet in a harmonic potential, the current models are restricted to the (2,1) bouncing mode with prescribed impact phase, it still remains to develop models that can handle different bouncing modes. Reference [39] investigated what happens with a variable topography, nevertheless with significant additional computational cost due to a non constant liquid depth. As the objective was to obtain a general and complete model of the system, the numerous simplified models that were proposed to explain some specific behaviours of walkers were not described in this section.

Except for an analytical solution based on Green functions proposed in ref. [14] for the single slit experiment, none of the current models are able to handle eventual reflections of the waves in case of a small size bath, which the situation of interest in this work. This means that no numerical simulation of the droplets dynamics was possible to confront to the experimental results presented in Section 4.3. This gives room for further research in the study of the wave reflection on a bath border and further development of such a mathematical model.

To conclude, it is important to point out the possibility to combine the dynamics equations coming from different models. For example, a very complete model of this pilot-wave system may use eq. (3.17) for the vertical dynamics, eq. (3.31) for the horizontal dynamics and eq. (3.27) for the wave dynamics. This choice may rely on specific criteria such as the accuracy or the computational cost.

3.2 Review of droplet experiments

The objective of this section is to present a short review of all the phenomena that have been observed experimentally with walking droplets. Some illustrative movies can be found online (e.g. [25, 77]).

3.2.1 Bouncing and walking regimes

Here we synthesize the numerous experiments that have been conducted on the dynamics of bouncing and walking droplets. Intensive research has been conducted on the characterization of the different bouncing modes as a function of the forcing parameters [48, 49, 59, 89] and the walking speeds in the walking regime [49, 59].

In 2011, reference [19] investigated the nature of a walker's wave field. The authors showed that each shock emits a radial travelling wave, leaving behind a localized mode of slowly decaying Faraday standing waves. For rectilinear trajectories, the linear superposition of the waves generated results in a Fresnel interference pattern of the global wave field.

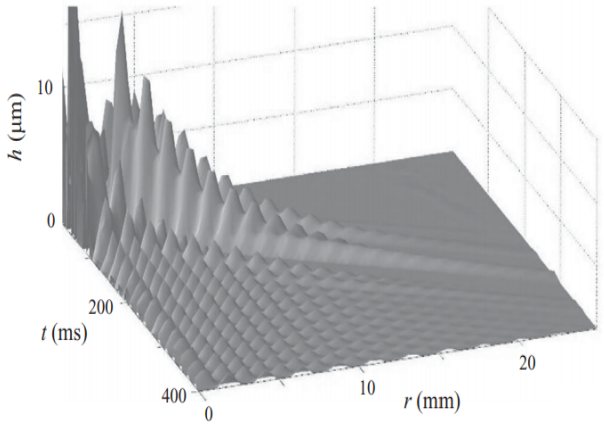

Figure 3.14: Spatio-temporal 3D reconstruction of the wave propagation away from the point of impact of a steel ball on the bath (at time $t = 0$) with $\Gamma^{-1} = 32$. Taken from [19].

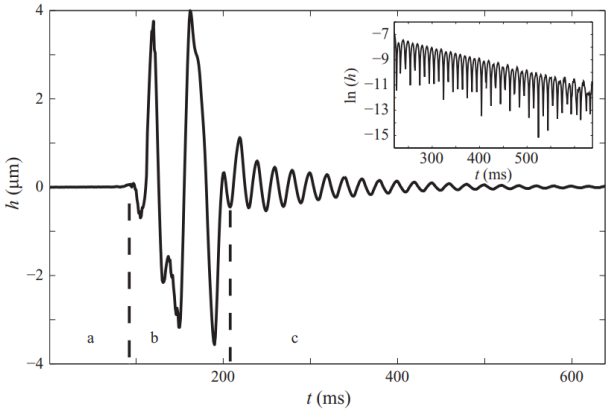

Figure 3.15: The temporal evolution of the liquid height at a point located 5.3 [mm] away from the ball impact. The measured non-dimensional damping time $\tau/T_F = 6.25$ is the real value of the memory parameter. It is close to the expected value $\Gamma^{-1} = 5$. Taken from [19].

In addition to the observations made on the wave emitted by the bouncing and walking droplets, it has been observed that the bouncing mode of these latter could be very exotic. The examples of three different bouncing modes are given in Figure 3.16.

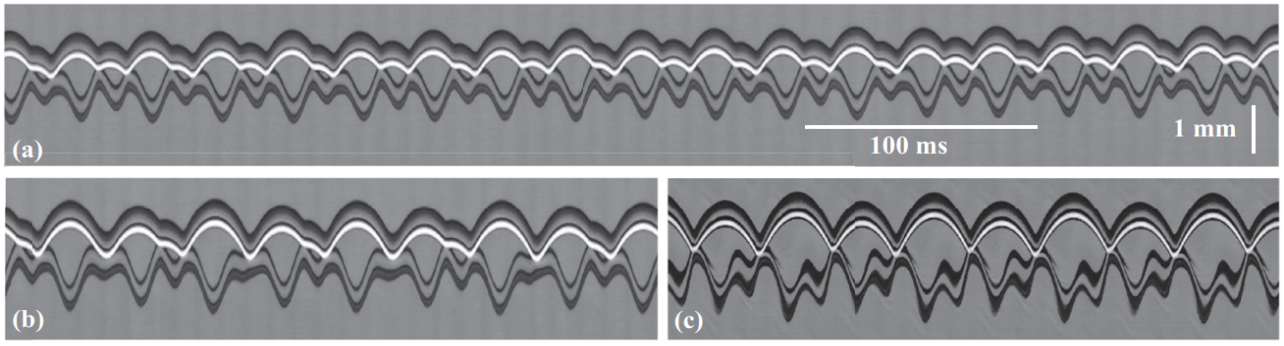

Figure 3.16: Spatiotemporal diagrams of the bouncing modes observed for the $20[cSt] - 80[Hz]$ combination. (a) Bouncing mode (4,4), $\Gamma = 2.3$, $\Omega = 0.45$. (b) Bouncing mode (4,3), $\Gamma = 2.7$, $\Omega = 0.45$. (c) Bouncing mode (4,2), $\Gamma = 3.5$, $\Omega = 0.42$. From [89].

Where the bouncing mode is also correlated to the contact time t_c of the droplet in the liquid bath, which has been measured for various droplet radii R_0, acceleration peaks Γ and Webber numbers We in refs. [48] and [49].

The dependency of the bouncing mode on the system parameters has also been examined to allow for a more deterministic control of the experiments conducted on walkers. In most cases, this dependency is presented in a *phase diagram* where the two parameters are the vibration number Ω and the non-dimensional acceleration peak Γ, as depicted in Figure 3.17.

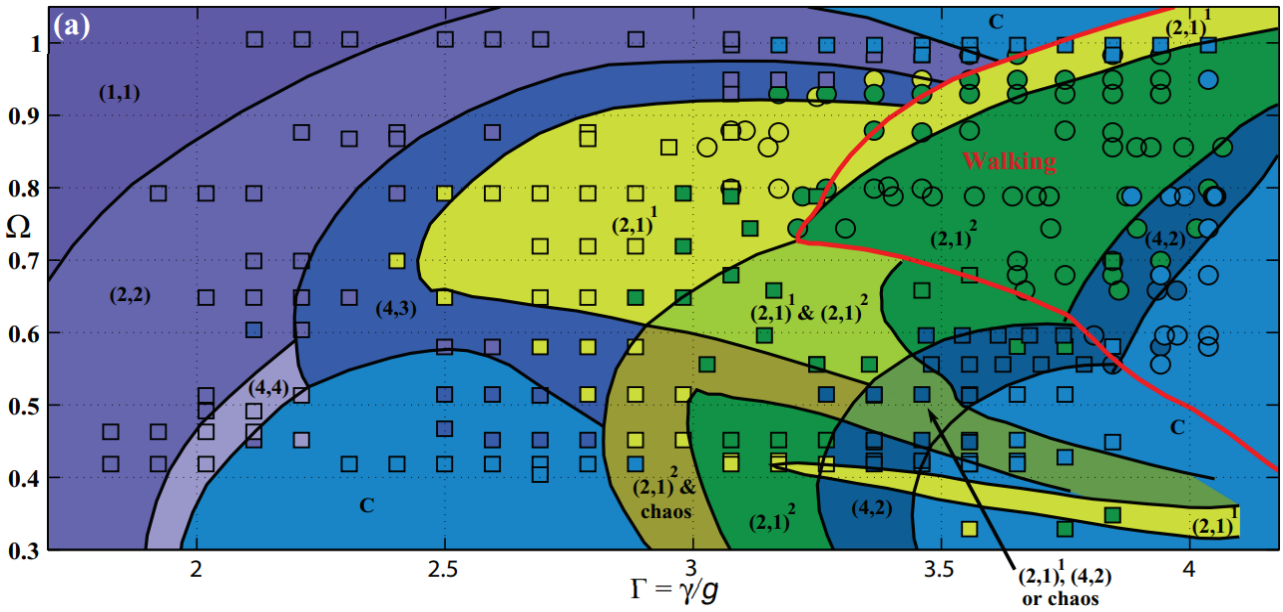

Figure 3.17: Bouncing modes diagram for $f = 80$ [Hz] and $\nu = 20$ [cSt] taken from [89]. Also obtained in [49].

The walking regime is surrounded in red in Figure 3.17. This highlights the existence of a bifurcation where the droplet jumps from a simple bouncing regime to a walking regime where it moves horizontally at the surface of the bath. The walking regime is not straightforward to obtain and it has been shown that choosing $f = 80[Hz], \nu = 20[cSt]$ was optimal for reaching it (see Figure 3.6). [59] The droplet's walking speed V_W and impact phase ϕ have also been measured vs the distance to Faraday threshold $\mathcal{M}$ and for some droplet radii [2, 59].

In the walking regime, as the droplet plays the role of a moving wave source, a Doppler effect has been observed experimentally [19, 63]. From Figure 3.18, it can be seen that the wavelengths ahead and beyond of the walker deviate from the Faraday wavelength λ_F with a deviation linearly dependant on the walker's speed.

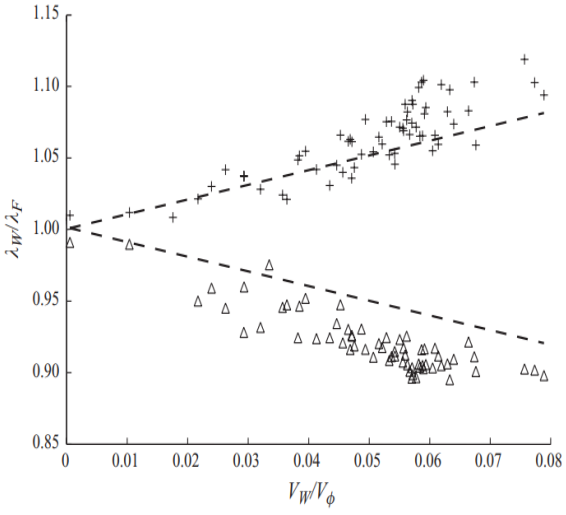

Figure 3.18: Doppler effect measured in [19].

It has to be noted that ref. [51] recently discovered a new class of walking droplets called *superwalkers* by the authors. These superwalkers appear in the presence of two driving frequencies and can be more than double the size of the largest walkers. They can also travel at more than triple the speed of the fastest walkers. With these superwalkers, the authors could observe some interesting behaviour. Among them can be cited droplets orbits with intermittent reversals of the orbiting direction as well as stop and go motions.

3.2.2 Interaction with interfaces

From here, the described experiments will be on the non-classical behaviour of walking droplets in their horizontal dynamics. The following observations are the reasons that raised the interest for making analogies between the walking droplet system and the quantum world.

Due to the intrinsic wave-particle duality of walkers, the presence of interfaces, i.e. walls (borders of the bath) or barriers (liquid depth variation) has a strong influence on the way they behave. Indeed, changing the local depth of the bath hence changes the dispersion relation for the Faraday waves. For a sufficiently small depth these waves are so strongly damped that this effectively leads to a region into which the walking droplets generally cannot go even though surface waves may slightly penetrate this region. One of the first experiments that were conducted on the interaction with an interface was to observe the diffraction of a walker through a single slit. [22]

Diffraction Reference [22] presented the first experimental measurements conducted on single and double slit diffraction. The authors claimed the proximity between the interference pattern obtained behind the slits and the quantum equivalent with electrons. These results were contested [6], especially due to the symmetrization of the presented histogram plots and the lack of reproductibility of the results due to poor exploration of the parameters space.

The experimental setup for the measurement is shown in Figure 3.19. Reference [62] recently revisited the discussions given in [6] and [22] to claim the following. "Unlike the diffraction patterns arising in optics and quantum mechanics, the number of peaks in the walking droplet system is not expected to depend on the relative magnitudes of the wavelength and the slit width. The droplet trajectories in the single- and double-slit geometries with the same initial conditions can be markedly different (Figure 3.20), showing that it is influenced by both slits. As pointed out by ref. [6], this influence does not necessarily mean that the wave passes through both slits and then affects the drop motion. Rather, it results from the spatial extent of the pilot-wave field, which allows the walker to be influenced by both slits".

As shown in Figure 3.21, the deflection angle α behind the slit(s) is strongly dependent on the forcing parameters. In the low-memory regime, the relationship between the impact parameter y_i and the deflection angle is deterministic and there is thus no uncertainty. However, this determinism disappears for sufficiently high memory regimes (namely $Me \simeq 0.99$).

Reference [14] proposed an analytical model based on Green functions to take the presence of boundaries into account. Their model suggests three preferred deflections angles behind the slit, as observed in [62].

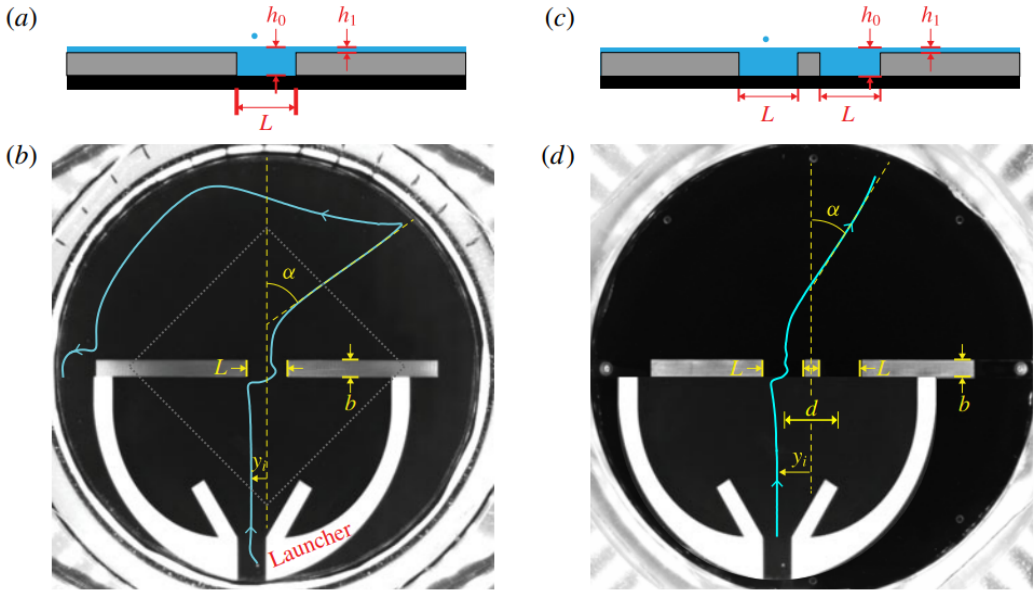

Figure 3.19: Experimental set-ups for single- and double-slit geometries. (a) (c) Side view of the submerged slit geometries. (b) (d) Plan view. From [62].

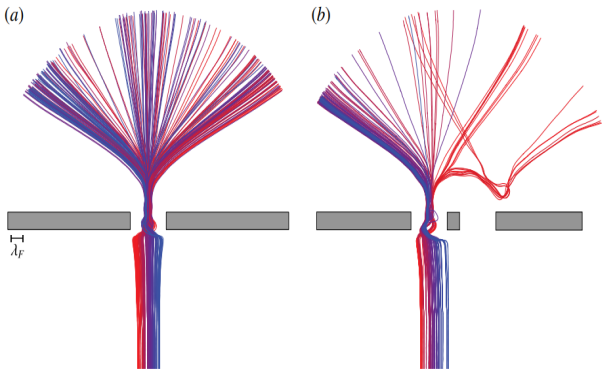

Figure 3.20: Comparison between observed (a) single-slit and (b) double-slit trajectories, with forcing $\Gamma/\Gamma_F = 0.998 \pm 0.002$ and free walking speed $u_0 = 6.8 \pm 0.2$ [mm/s]. The marked difference between the two indicates the influence of the second slit. From [62].

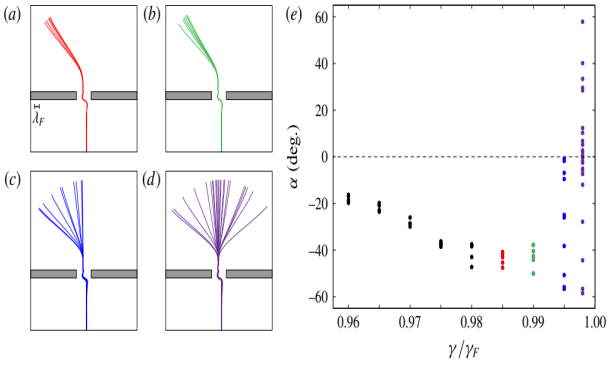

Figure 3.21: Trajectories of a walking droplet passing through the slit with fixed impact parameter $y_i = +0.17L$, and with respective forcing and free speed: $(\gamma/\gamma_F, u_0[mm/s]) =$ (a) (0.985, 6.4), (b) (0.990,6.6), (c) (0.995,6.8) and (d) (0.998,6.9). (e) Dependence of the deflection angle α on the forcing γ/γ_F for $y_i = +0.17L$. From [62].

Reflections on barriers Reference [61] realized exhaustive measurements of the reflection of a walker on a barrier with shallow liquid height. This work highlighted the non-specular character of the reflections, i.e. the reflection angle θ_r is in general different from the incidence angle θ_i. For a fixed memory parameter, we observe that a wide range of θ_i converges to a narrow band of θ_r in the vicinity of 70°. For a fixed incidence angle, the memory parameter variation induces some variations of the reflection angle. Finally, for very high memory regimes, the droplet can eventually execute a loop due to a transient self-confinement in its own wave, and thus be reflected almost towards its incidence direction, as depicted in Figure 3.22 (b).
On the other hand, reference [76] studied the dependency of a droplet reflection in a periodic potential well created by the jumping between two different liquid heights as a square signal along the space. The authors observed that the probability of reflection was directly associated to the ratio between the well spatial period p and the Faraday wavelength λ_F.
The interacting with a submerged pillar was also studied in [42].

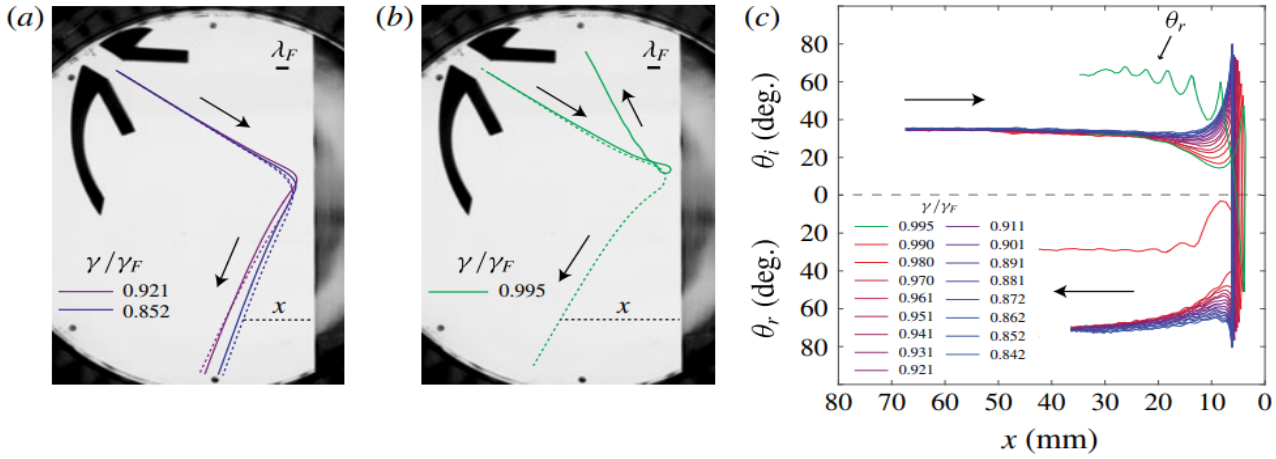

Figure 3.22: Dependence on the memory γ/γ_F of the reflection of a walker for a fixed initial angle of incident $\theta_i = 34.9 \pm 0.6°$. Comparison of experimental (solid line) and theoretical (dashed line) trajectories at (a) two low memories and (b) one very high memory (c) Local measurement of the angle of incident $theta_i$ and the reflected angle θ_r as a function of the distance x from the barrier at different memories. From [61].

Tunnel effect In 2009, ref. [18] recorded evidence for a tunneling effect, where the reflection or transmission of a given incident walker on a submerged barrier is unpredictable. However, the crossing probability decreases exponentially with increasing barrier width. This shows that this wave-particle association has a nonlocality sufficient to generate a quantumlike tunneling at a macroscopic scale. Reference [28] revisited this experiment both theoretically and experimentally. Based on a simple model taking into account both a self-propulsion implemented by means of Rayleigh-type friction force and a repulsion force due to the increasing potential of the submerged barrier, they prove the existence of two stable solutions for the walker's speed after the contact with the barrier, it can either be reflected or transmitted. They show that the non-Hamiltonian self-propulsion properties of walkers are sufficient to rationalize their crossing of submarine barriers of potential. However, they introduce the randomness of initial conditions, namely the angle of incidence, as an ad hoc ingredient.

Waveguide analogy The confinement of a walker in different rectangular cavities, used as waveguides for the Faraday waves emitted by successive droplet bounces was investigated in [27].
For well widths smaller than the Faraday wavelength $D < \lambda_F$, the droplet can only bounce and thus never walks. It is observed that a one-dimensional confinement is optimal for narrow channels of width of $D = 1.5\lambda_F$. It is shown, due to an energetic study, that the optimal width maximizing the longitudinal speed v_y is around $2\lambda_F$ such that applications can be designed. The longitudinal walking speed is found to be:

$$v_y = \pm v_y^{(0)} \sqrt{1 - \left(\frac{\lambda_F}{D}\right)^2} \tag{3.36}$$

In addition, upon shedding light on the question of how straight the walker's motion can be in a 1D channel, this study complements the works based on walkers in confined geometries.

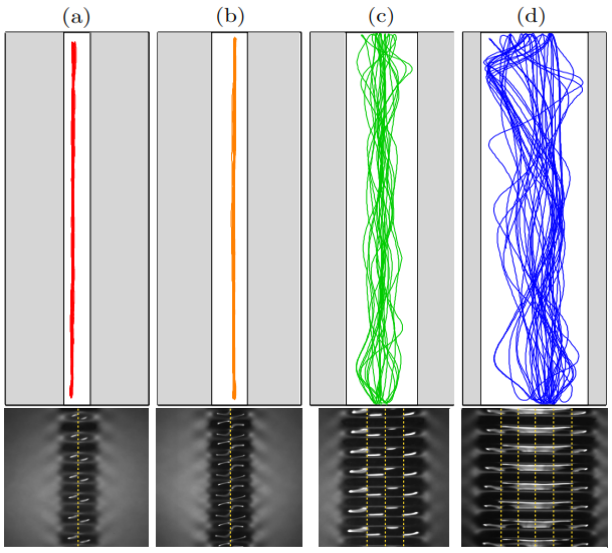

Figure 3.23: Typical trajectories of a walker in four channels (a) $D/\lambda_F \simeq 1.5$, (b) $D/\lambda_F \simeq 2$, (c) $D/\lambda_F \simeq 4$ and (d) $D/\lambda_F \simeq 5.5$. From [27].

3.2.3 Evolution in a varying potential or a confined geometry

In the case of experiments conducted on walkers, what is called *potential* is related to the ability for an amnesic (i.e. low memory) walker to go in a given region of the system, analogous to the energy level potential of quantum systems. Three techniques have been used to control the potential inside a walking droplet system : (i) Vary the liquid height [18, 76] (ii) Rotate the whole system to induce a fictive centripetal force and then obtain a harmonic potential [44, 56, 74, 75] (iii) Magnetize the droplet by using ferrofluid and impose a magnetic field transverse to the 2D system. [56, 73]
The interesting features of these techniques is that it allows to confine the walker in a given spatial region of the system, thus leading to an effective confined geometry. [23, 24, 73] Hence, the experiments realized on walkers with confined geometries or confining potentials led to very similar observations. Under this condition, there will be a mixing between confined geometry and confining potential in the following presented results, which intuitively could be obtained in both cases.

When a walker evolves in a system whose dimensions are comparable to a couple Faraday wavelengths (named here a *confined geometry* or *cavity*) and if the memory Me is high enough, the interaction of the created waves with the borders of the system will amplify the eigenmodes of this cavity and several new behaviours appear. Before describing these latter, let us inspire from ref. [56] to define some quantities (or *observables*) :

$$\overline{R} = \sqrt{\frac{1}{N}\sum_{k=0}^{N}\frac{r_k^2(t)}{\lambda_F^2}} \tag{3.37}$$

is a normalized mean spatial extension, where $\{r_k\}$ denotes the ensemble of droplet's horizontal positions wrt the cavity/potential center and N is the number of recorded positions. The advantage of choosing a quadratic mean is that it allows to associate a mean potential energy $\overline{E}_p$ to the droplet's move as :

$$\overline{E}_p = \frac{\overline{R}^2}{\Lambda^2} = \frac{1}{N}\sum_{k=0}^{N}\frac{\omega_r^2 r_k(t)^2}{V^2} \tag{3.38}$$

The second observable is a normalized angular momentum $\overline{L}$ defined as :

$$\overline{L} = \frac{1}{N}\sum_{k=0}^{N}\frac{\vec{r_k}}{\lambda_F}\times\frac{\vec{V}_k}{V_0} \tag{3.39}$$

Where V_0 is the droplet velocity in the free walking case (assuming an infinitely large system), $\vec{V}_k$ is the droplet velocity vector at a given time instant k and $\Lambda = V/(\lambda_F\omega_r)$ is the non-dimensionalized size of the confinement, where $\omega_r \simeq 1.2\omega$ corresponds to the characteristic pulsation of the confined walker.

Harmonic potential [34, 56] studied the confinement of a walker inside a harmonic potential created with an externally applied magnetic field. In the low-memory regime, the walker is said to be amnesic and inevitably converges to a circular orbit where the radius of this orbit is directly related to the harmonic potential width. The stability of the orbits has been analyzed in [34, 73].

When increasing the memory Me such that some wave perturbations due to previous bounces of the droplet are still present after one traveled orbital revolution, the walker starts doing messy loop trajectories that at first glance look random. However, when looking closer at the long-term statistics of these trajectories, one can observe the emergence of new stable trajectories (Figure 3.24). They form a set of geometrical curves called *Cassinians*, which all obey to the following equation in polar coordinates (r, θ) :

$$r^{2k} = -2e^k r^k \cos(k\theta) + e^{2k} - r_0^{2k} = 0 \quad (3.40)$$

Where the integer k corresponds to the Cassinian order, r_0 its size and e its excentricity, i.e. the relative distance between the fixed points wrt the extension r_0.

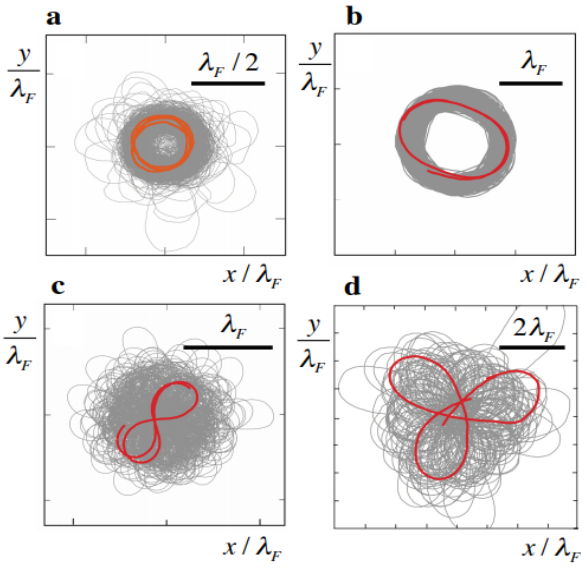

Figure 3.24: 4 examples of cassinian trajectories. (a) circular orbit ($Me = 100, \Lambda = 0.42$), (b) oval ($Me = 60, \Lambda = 0.8$), (c) lemniscate ($Me = 50, \Lambda = 0.7$), (d) trifolium ($Me = 60, \Lambda = 1.2$). From [56].

Moreover, the results shown in Figures 3.25 and 3.26 give experimental evidence of a double quantification (both for $\overline{R}$ and $\overline{L}_z$) as the memory increases.

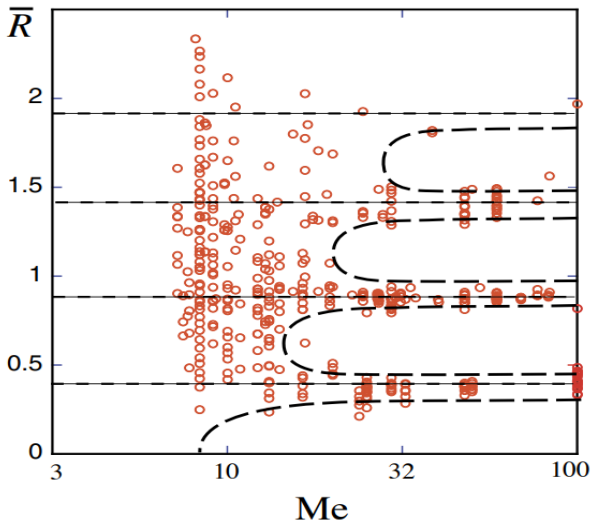

Figure 3.25: Circular orbits quantification as Me increases. Taken from [56].

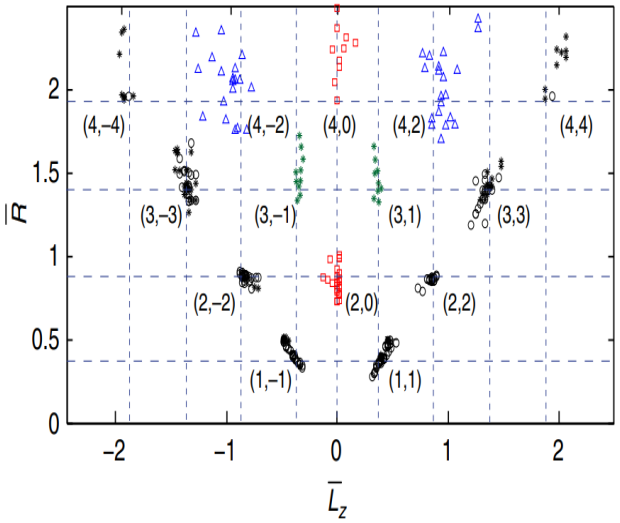

Figure 3.26: Double quantification of the stable orbits. Evolution of the mean spatial extent $\overline{R}$ as a function of the average kinetic momentum. Taken from [56].

It is observed that the trajectories at high memory Me correspond to chaotic regimes characterized by intermittent transitions between a discrete set of states. [56, 57] At any given time, the system is in one of these states characterized by a double quantization of size and angular momentum. A low dimensional intermittency determines their respective probabilities. They thus form an eigenstate basis of decomposition for what would be observed as a superposition of states if all measurements were intrusive.

References [44, 74, 75, 88] investigated the case of a harmonic potential induced by the rotation of the vibrated bath around the vertical axis. One observes in Figure 3.27 the quantification

of the orbital radius r_0 as the memory parameter increases. Moreover, the tendency of r_0 to diminish as Ω increases is reminiscent of the narrowing of the harmonic potential induced by the coriolis effect.

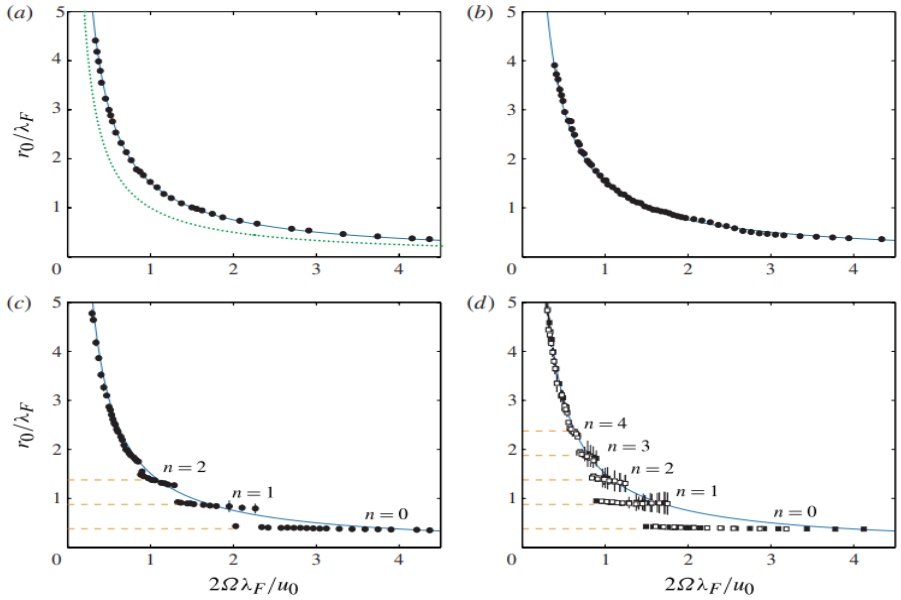

Figure 3.27: Observed dependence of the orbital radius r_0 on the rotation rate of the bath Ω: $\gamma/\gamma_F = (0.822, 0.922, 0.954, 0.971)$ for (a), (b), (c), (d), respectively. Taken from [44].

The emergence of those quantized orbits can be explained by the orbital stability diagram derived in [74] shown in Figure 3.28. This diagram has been extended to predict the resulting walker's exotic trajectories numerically explored and described in [75] and is shown in Figure 3.29.

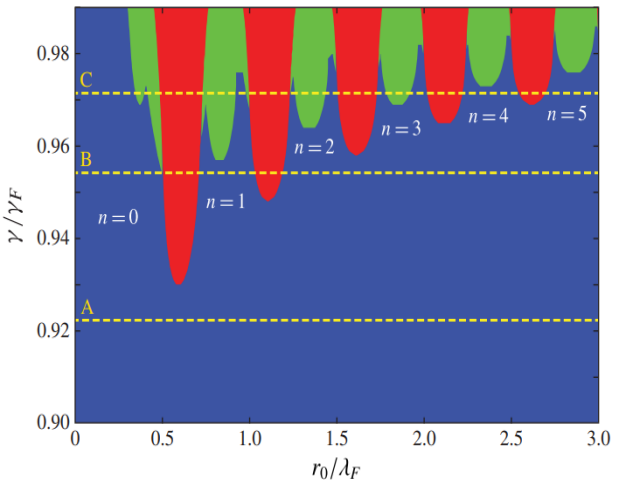

Figure 3.28: Orbital stability diagram for a walker of radius $R_0 = 0.4$ [mm], phase $\sin\Phi = 0.16$, viscosity $\nu = 20.9$ [cSt] and forcing frequency $f_0 = 80$ [Hz]. The blue region denotes the stable regions while the green and red ones stand for unstable regions. Taken from [74]. Also obtained in [34].

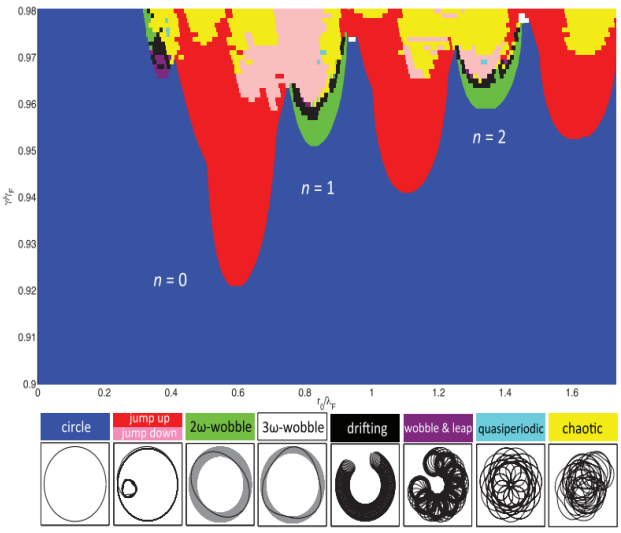

Figure 3.29: Regime diagram delineating the dependence of the walker's trajectory on the initial orbital radius r_0 and vibrational forcing γ. Taken from [75].

As the forcing acceleration is progressively increased, stable circular orbits give way to wobbling orbits, well depicted in Figure 3.29 and Fig. 2 of [75], which are succeeded in turn by instabilities of the orbital center characterized by steady drifting then discrete leaping.

Corrals As intuitively predicted in the beginning of this section and shown in [11, 41], a walking droplet confined in a circular cavity exhibits the same behaviours as when a harmonic potential is imposed. Indeed, we recover cassinian curved trajectories and the double quantification of the radial distance $\overline{R}$ and the angular momentum $\overline{L}$.
In Figure 3.31, dark circular strips indicate more frequent impacts at certain radial positions. The corresponding probability distribution function $\rho(r)$ shows a series of extrema at specific radii. The radial position oscillates intermittently between these preferred radii.
Some tools for a fair comparison between a walker and a quantum particle are given in [24]. It is shown that the chaotic trajectories of confined walkers are ballistic on the short term and diffusive on the long term. "The coherence distance, beyond which the ballistic behavior is lost, corresponds to half the Faraday wavelength. The Faraday wavelength is at the heart of most quantumlike behaviors of walkers; it is identified as equivalent to the de Broglie wavelength for a quantum particle. Our analysis of the diffusive motion in a circular corral has suggested another equivalence, between the diffusion coefficient D and the factor $\hbar/m$ in the Schrödinger equation. The walker behavior thus becomes apparently random only when it is analyzed at a length scale larger than $\lambda_F/2$. This analogy is confirmed by the observed ballistic speed of the walker, which corresponds closely to the de Broglie speed $\hbar k/m$. Similarly, the average kinetic energy of the walker matches Schrodinger's prediction over several orders of magnitude."

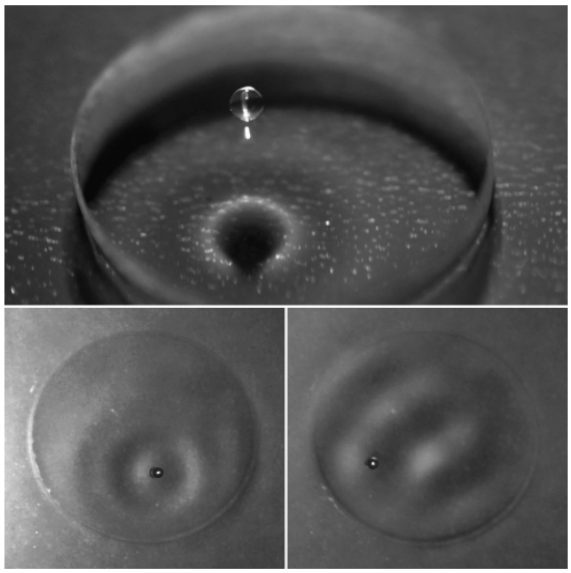

Figure 3.30: Pictures of the circular corral used in [24].

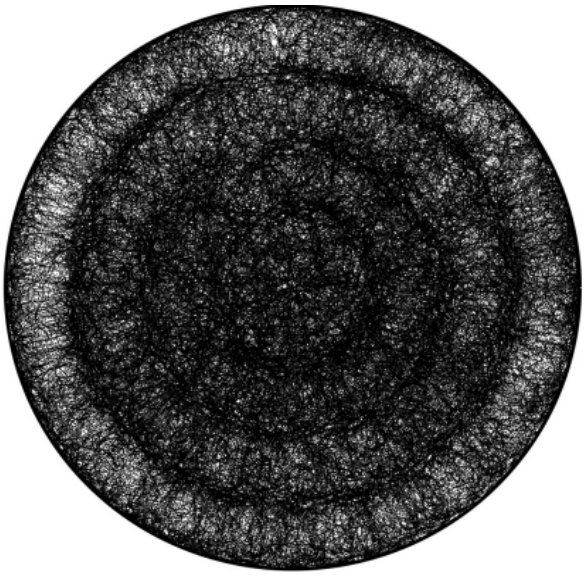

Figure 3.31: Two-dimensional probability distribution function obtained by superimposing half a million impact positions issued from 78 independent trajectories. From [24].

The case of the circular corral was extended to an elliptical corral in [10]. They showed that placing a circular well at one of the foci of the ellipse, a mode with maxima near the foci is preferentially excited, leading to a projection effect in the walker's position histogram towards the empty focus, an effect strongly reminiscent of the *quantum mirage*. [47] They have demonstrated that a localized irregularity in the medium can drastically change the relative weight of the resonant modes and thus the statistical response of the confined droplet. As in the quantum corral experiments, they have shown that the position of the irregularity plays a critical role in the resulting statistical behaviour.

3.2.4 Interactions between multiple droplets

If several droplets evolve in the same environment and sufficiently close to each other, they become coupled by the intermediary of the wave which they created and which guides them. This coupling can take different forms, and if often dependent on the relative phase between them.

Lattices

Bouncing droplets on a vibrated liquid bath that interact through the surface waves they emitted can form various types of stable crystalline clusters. Examples of such clusters are shown in Figure 3.32. Such clusters have been studied in [16, 17, 59]. When increasing the forcing acceleration over an onset value, the aggregates present a global and spontaneous vibration mode where all droplets vibrate around their equilibrium positions. These oscillatory modes are similar to the phonons of a solid crystal. Finally, when the period doubling is complete, the droplets become walkers. The crystal is usually destroyed but small crystallites sometimes undergo a transition to global rotation.

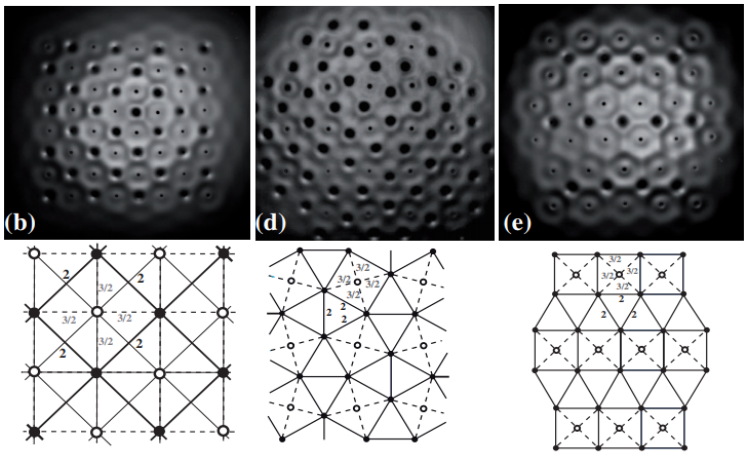

Figure 3.32: The observed 2D periodic organizations of droplets of two different phases and their interpretation. A sketch of the relation between the two sub lattices is given below each photograph. (b) Two identical square sub-lattices (4^4). Each square is stabilized by a central drop of the other phase. (d) A snub square (3^2, 4, 3, 4) associated to a square sublattice. (e) An elongated triangular lattice ($3^3, 4^2$) associated to a monoclinic sublattice. Taken from [17].

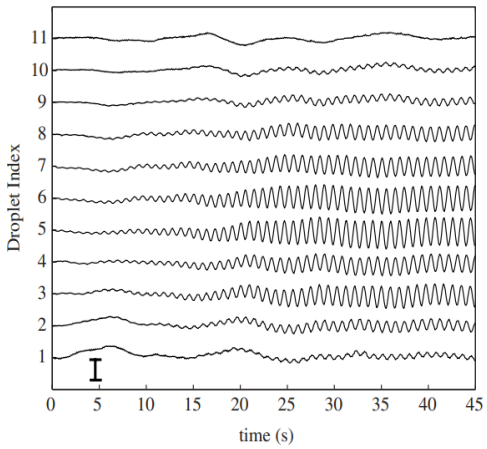

Figure 3.33: Trajectories along a line of 11 droplets in hexagonal symmetry illustrating their vibration mode similar to phonons in solid-state crystals. Each droplet is moving in phase opposition with its neighbours. From [16].

Collisions and promenades

If two walkers with identical sizes are projected in parallel towards each other, we talk about a *collision*. The distance between the two parallel lines formed by the initial trajectories of both droplet is called the *impact parameter* and writes y_i. Depending on y_i, there are two possible issues (1) the meeting results in a *constructive* collision where the walkers are attracted and either start orbiting around each other or start walking in the same direction with their interdistance oscillating along the path. This second case is called a *promenade*. (2) the meeting results in a *destructive* collision where they are repulsed and follow their newly deviated trajectories.

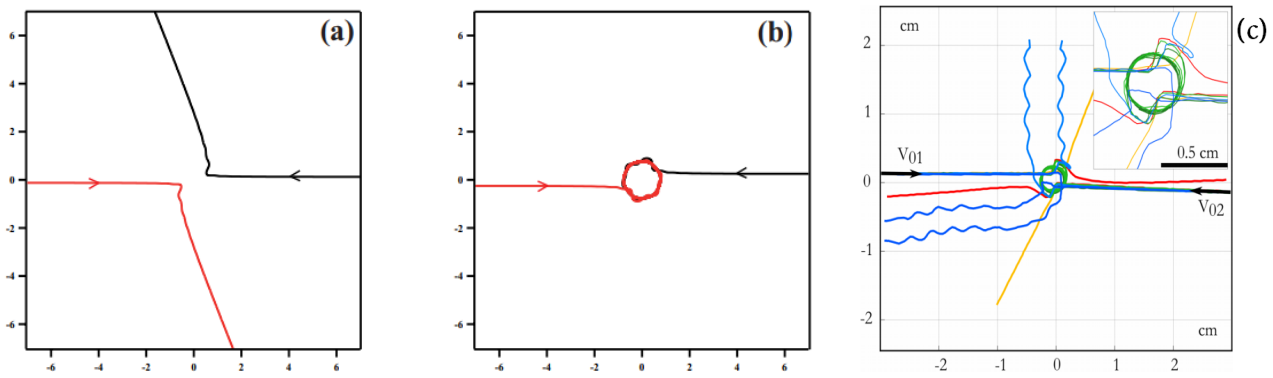

Figure 3.34: (a) Repulsive collision. (b) Attractive collision leading to an orbiting pair. From [59]. (c) Superposition of 6 experiments with approximately the same initial conditions and markedly different outcomes: scattering (red and yellow), orbiting (light and dark green), and promenades (light and dark blue) from [67].

Moreover, it has been observed that the distance d_n^{orb} between two droplets orbiting around each other takes discrete values :

$$d_n^{orb} = (n - \epsilon_0)\lambda_F \tag{3.41}$$

Where n is (half) an integer if the droplets bounce in (opposition of) phase and $\epsilon_0 \approx 0.2$ is a constant shift hiding more complex interactions (partly interpreted in references [59, 60]).

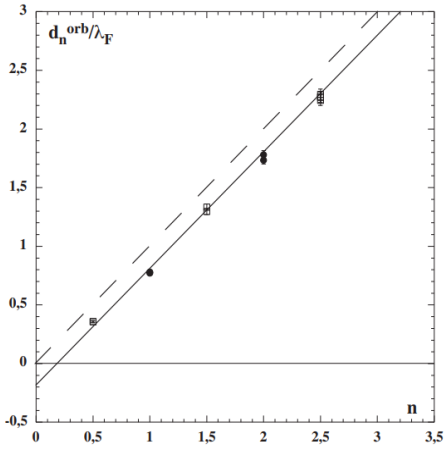

Figure 3.35: Measured diameter of the orbit of two walkers as a function of their order n. Taken from [59].

A theoretical and numerical investigation made in [50] revealed the existence of more exotic behaviors for two identical in-phase bouncing droplets, synthetized in their Fig. 1.

Other phenomena can appear if droplets of different sizes interact. Among them, we can mention the *epycicles* and the *orbiting promenades* studied in [59].

Trains of droplets were experimentally studied in [21] in an annular cavity forming an equivalent infinite 1D system. It was shown that the walkers there spontaneously synchronize to share a common coherent wave propelling the group at a speed faster than single walkers. This group speed in monotonically increasing with the number of droplets yet saturating around $v_N = 1.22v_1$ where v_N is the group speed and v_1 is the speed of one only walker. For a pair of walkers, the pair speed increases as their interdistance, which can take only specific values as written in eq. (3.41), diminishes.

Chapter 4

Walking droplet experiment

The complete description and validation of the experimental setup is given in this section. Additionally, the obtained observations are reported and discussed based on the state of the art and the quality of the setup.

4.1 Experimental setup

This section aims at describing the low-cost self-developed setup and justifying the choices made in its conception. The different software programs as well as 3D drawings made with *Solidworks* are available in open-source in the *Supplementary materials* [35].

A schematic of the experimental setup in shown in Figure 4.1. A stadium-shaped bath made out of plexiglas has been fabricated and fixed on the membrane of a loudspeaker. The bath is attached to the membrane of a loudspeaker playing the role of an electromagnetic shaker which oscillates vertically with acceleration $\gamma(t) = \gamma_m \cos(\omega_0 t)$ where γ_m and $f_0 = \frac{\omega}{2\pi} = 80$ [Hz] are the prescribed maximum acceleration and frequency, respectively. The stadium of width $W = 38$ [mm] and length $L = 2W = 76$ [mm] has been designed such that $W \approx 8\lambda_F$ with the parameters in Table 1. It is filled of silicone oil to a height $h_0 \in [6 - 11]$ [mm] (depending on the used stadium bath) such that a thin liquid film of depth $h_1 < 1$ [mm] overlays its border, serving as a wave damper. The real setup is shown in Figure 4.2.

The used silicone oil comes from *Sigma-Aldrich* [65], with its physical properties given in Table 1. The viscosity $\nu = 20$ [cSt] at $T = 25[°C]$ has been shown to be ideal for observing walkers with a frequency of forcing $f_0 = 80$ [Hz] (see Figure 3.6). Moreover, this viscosity is high enough to obtain an Ohnesorge number lying in the $Oh \in [0.175, 0.3]$ interval depending on the droplet's radius, this means that the magnitude (~ 1) of Oh is sufficient to neglect the deformation modes of the droplet in good approximation. Following eq. (3.1), the liquid can be considered to have an infinite depth if the liquid height h_0 fulfils the condition :

$$tanh(k_F h_0) \approx 1 \iff k_F h_0 > 4 \tag{4.1}$$

With $k_F = 1330$ [rad/m], eq. (4.1) yields the condition $h_0 > 3$ [mm] which will always be satisfied in the following experiments.

Images of the pilot-wave system are recorded with a *Panasonic DMC-FZ45* camera. The camera has a framerate of 25 FPS and a resolution of 1080x720 pixels and is placed above the bath at a height $H = 62$ [cm] to justify the paraxial approximation useful in Section 4.1.3. This camera aims to analyze both the horizontal droplet dynamics and the wave dynamics. The camera has

no trigger thus the beginning of a recording is launched manually and there is no deterministic relationship between the taken images and the droplet's vertical state. With the current setup, there is no way to properly analyze the vertical dynamics. The images are post-processed with *Matlab* routines running on PC and described in Sections 4.1.3 and 4.1.4. A desk lamp without occlusion is placed close to the camera and at the same height to avoid heating the liquid whose properties vary with temperature.

The vertical forcing of the bath as well as the acceleration measurement are fully described in Section 4.1.1. Regarding the droplet on demand generator (DOD) described in Section 4.1.2, the fluid reservoir at the rear (see Figure 4.9) is voluntarily hidden for a sake of simplicity in the schematic.

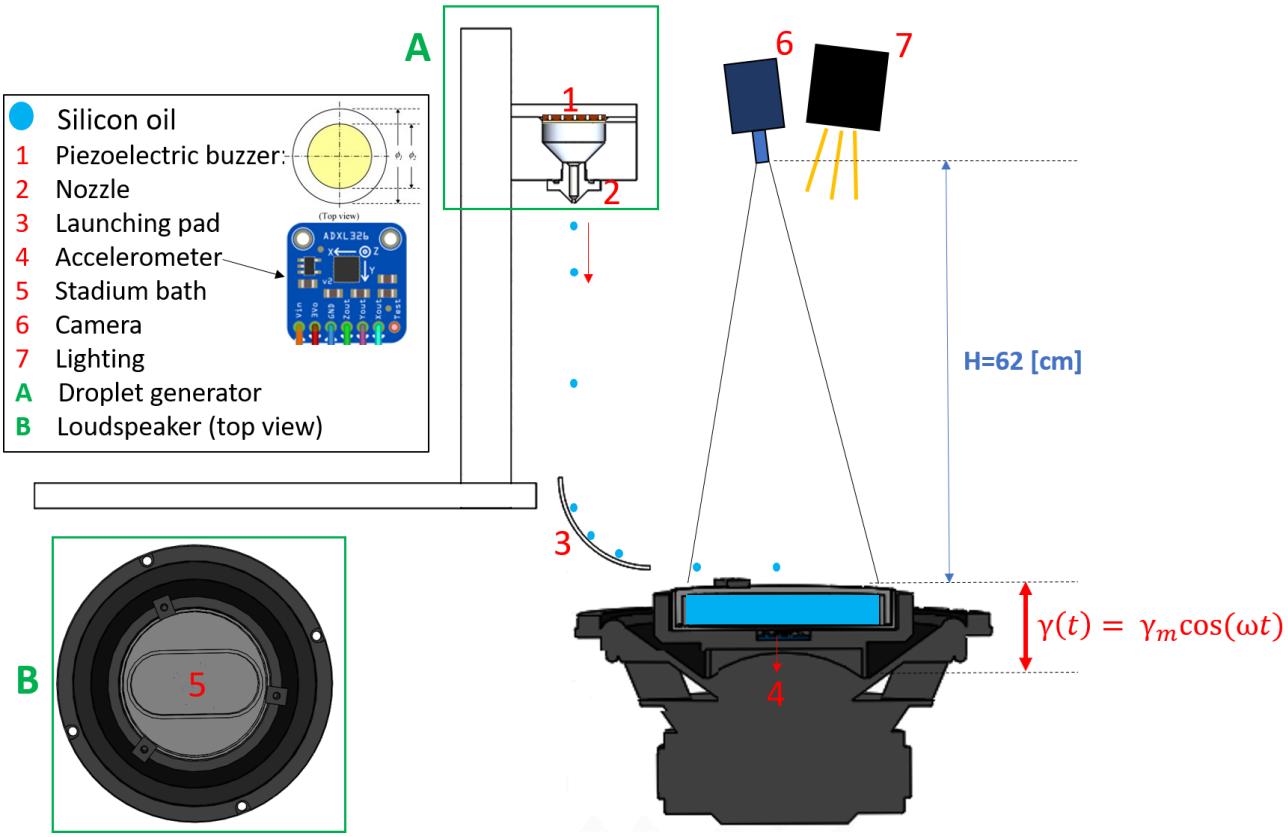

Figure 4.1: Schematic of the experimental setup.

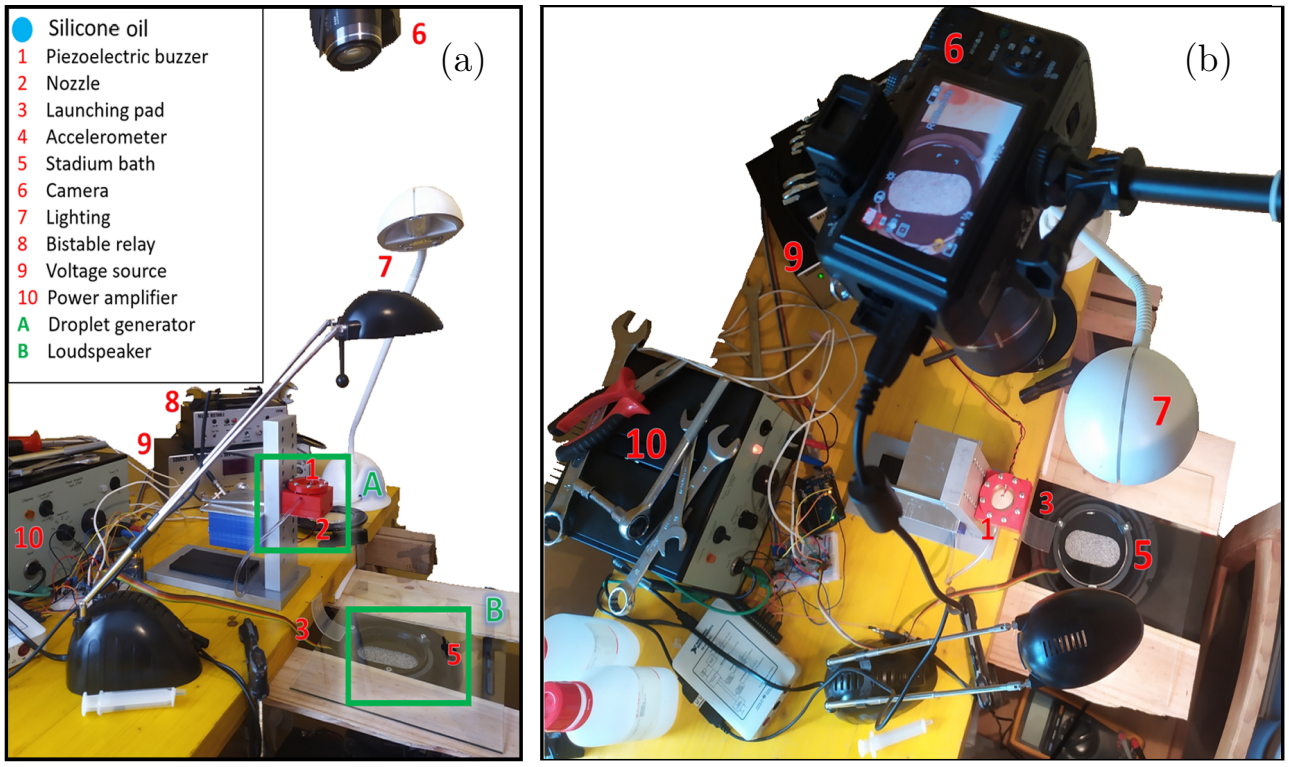

Figure 4.2: Real experimental setup. The background in painted in white for a better focus on the foreground. The accelerometer present in Figure 4.1 is hidden here. The vibrating bath is placed on a chair such that it does not vibrate all the other components attached to the table. A non treated glass screen is placed on top of the bath to protect it from parasitic air flow. (a) sideview (b) top view.

4.1.1 Vertical oscillations

The vertical forcing of the bath is ensured by a *NI Labview* program ("*MyDAQ_memory_control.vi*" in the *Supplementary materials* [35]) that communicates with a *NI myDAQ*. The *NI myDAQ* has two analog inputs (AI) and two analog outputs (AO). The electrical connections are shown in Figure A.1. The *NI myDAQ* is able to actuate the loudspeaker through the use of a power amplifier, here a *Brüel Kjaer type 2706*. The power amplifier is not shown in Figure A.1 for clarity.

The loudspeaker has carefully been positioned flat by using a bubble level as verification tool. It is placed on a heavier asynchronous motor and united with it thanks to magnetization, the whole is then placed on top of an anti-vibration foam. These actions aim to reduce the external vibrations. Nothing has been used to stabilize the bath in the transverse directions.

The acceleration measurement is performed using a 3-axis ± 16 [g] ADXL326 accelerometer [3], which is supplied with 5 [V] coming from the Arduino Uno and outputs a voltage in the range [0,3.3] [V] for each axis depending on the sensed acceleration in that direction. As there are only 2 AI with the myDAQ, the X and Y accelerations are measured with the AI of the Arduino Uno.

The developped Labview program, namely "*MyDAQ_memory_control.vi*" allows the user to vary the frequency f_0, the amplitude A (hence also peak acceleration $\gamma = (2\pi f_0)^2 A$) and sample rate N of the forcing with the myDAQ. At the observation side, the front panel shows in real-time the acceleration amplitude Γ_m, two waveforms one for Γ versus time and one for its FFT in logarithmic scale, and based on a Faraday threshold input, an estimation of the current memory

value Me. The user interface is shown in Figure A.2. The proposed utilization consists in applying a voltage amplitude for the sinusoidal forcing, rising this amplitude until observing the Faraday instability, writing the measured acceleration amplitude in the corresponding control box, and then varying the input voltage by trials and errors to reach the desired memory parameter. Due to an unresolved enormous delay between the acceleration measurement and forcing (around 4 seconds), the initially intended PI controller was not used for an automatic convergence to the set point.

Signal conditioning chain and calibration

A functional block diagram of the capacitance-to-voltage conversion is shown in Fig.1 of [3]. The frequency of forcing $f_0 = 80$ [Hz] is well within the 3 axis bandwidth (min. 550 [Hz] for Z-axis). As the acceleration measurement is performed both with a Arduino Uno and a NI myDAQ, two calibration phases will be necessary. The Arduino Uno uses a 10-bit ADC in order to output the acceleration measurement while the myDAQ keeps an analog value which will be digitized by the computer. In both cases, we aim to find the slope A and offset B of the linear relationship between the device measurement and the corresponding normalized acceleration value Γ based on a finite set of pairs (x_i, Γ_i). As described in ref. [84], in this SISO case, the coefficients of the linear regression are :

$$\begin{cases} A = \frac{\sum_{i=1}^{N}(x_i - \overline{x})(\Gamma_i - \overline{\Gamma})}{\sum_{i=1}^{N}(x_i - \overline{x})^2} \\ B = \overline{\Gamma} - A\overline{x} \end{cases} \tag{4.2}$$

Where $\overline{x}$ and $\overline{\Gamma}$ denote the averages over all the x_i's and Γ's, respectively. The calibration values are given in Table 4.1. They yield $(A, B) = (52.63, -27262)$ for the Arduino Uno and $(16047, -27007)$ for the myDAQ, respectively.

Device	Measurement output type	Range	-1 [g]	0 [g]	1 [g]	[Unit]
Arduino Uno	decimal value i	[0-1023]	499	518	537	[-]
NI myDAQ	voltage V_{DAQ}	[0-3.3]	1.622	1.682	1.745	$[V]$

Table 4.1: Measurement output types and calibration values.

No supplementary material was accessible to give calibration points beyond $1000[mg]$ in absolute value but the referenced nonlinearity of $\pm 0.3\%$ [3] enforces the confidence in this extrapolation. The maximum relative error wrt the linear regression of 6[%] in Figure 4.6 gives an upper bound on the absolute error of about $\pm 260[mg]$ for the maximal acceleration Γ_F.

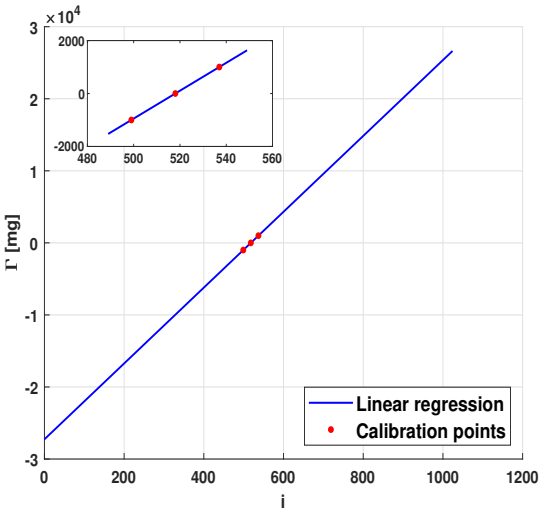

Figure 4.3: Calibration of the Arduino Uno measurement. The inset is a zoom on the calibration points to highlight their proximity to the linear regression.

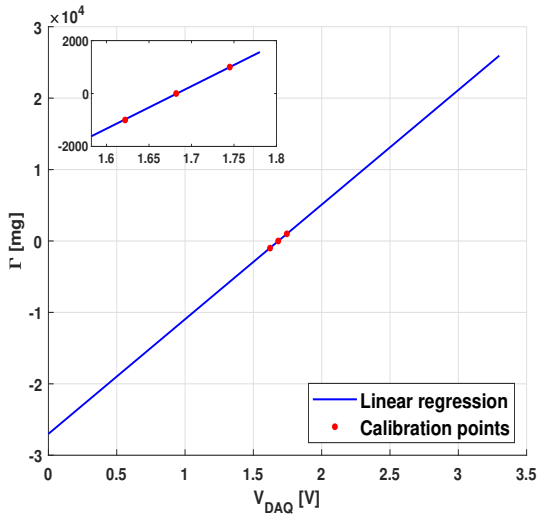

Figure 4.4: Calibration of the myDAQ measurement. The inset is a zoom on the calibration points to highlight their proximity to the linear regression.

The calibration results are depicted in Figures 4.3 and 4.4. What can be seen from these latter is that the ADXL326 is actually able to sense accelerations until ≈ 26 [g] (which is higher than the announced 16 [g]). With the given ranges, this leads to sensitivities of 50.78 [mg] between two consecutive integers for the Arduino Uno and 63.5 $[mV/g]$ for the myDAQ (magnitude predicted by [3]). As the range of interest for the acceleration is $[1-\Gamma_F, 1+\Gamma_F] = [-3144, 5144]$ [mg], the Z-axis output voltage of the ADXL326 is amplified using an op-amp based inverting amplifier, with an intermediate follower for impedance separation. A schematic of the amplifier is shown in Figure 4.5. The resulting calibration curve is given in Figure 4.6.

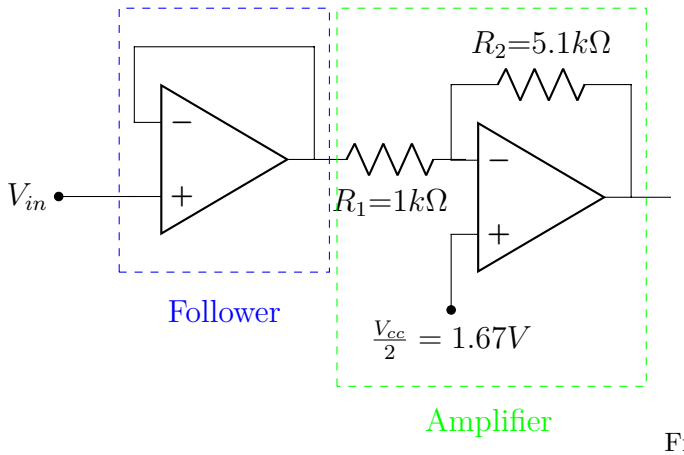

Figure 4.5: Sensitivity improvement circuit.

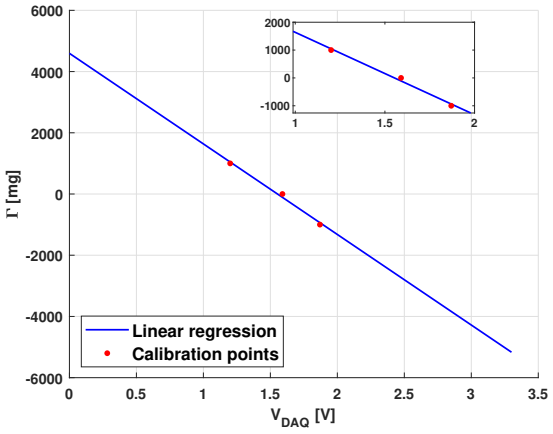

Figure 4.6: Calibration using the myDAQ after signal amplification for a higher sensitivity. The inset is a zoom on the calibration points. The resulting sensitivity is $323.6[mV/g]$.

Assuming an infinite gain for the op-amps and with $V_{cc} = 3.3$ [V], $R_1 = 1[k\Omega]$, $R_2 = 5.1[k\Omega]$, the output voltage equation writes as:

$$V_{out} = \frac{V_{cc}}{2}(1 + \frac{R_2}{R_1}) - \frac{R_2}{R_1}V_{in} = 10.187 - 5.1V_{in} \tag{4.3}$$

Analysis

The measured sinusoidal forcing is shown in Figures 4.7 and 4.8. One observes satisfying overlap between the measurement and the pure sinewave. Some harmonics can be observed in Figure 4.8, the related total harmonic distorsion (THD) is :

$$THD = 100\frac{\sqrt{\sum_{h=2}^{H} v_h^2}}{\sqrt{\sum_{h=1}^{H} v_h^2}} = 1.7867[\%] \tag{4.4}$$

Where $h = 1$ is the fundamental component and $h > 1$ are the harmonics. $H = 8$ here. The very low THD obtained in eq. (4.4) allows to consider the forcing signal to be perfect for the rest of the experiments. One can see in Figure 4.7 that the transverse accelerations along X and Y directions are non-zero due to the absence of stabilizing stuff, they oscillate with the vertical forcing with an acceleration amplitude of 75 and 136 [mg] (according to the 10-bit resolution of the Arduino ADC) for the X and Y directions, respectively. We discuss this issue in Section 4.3 and conclude that it implies an an effective Faraday threshold $\Gamma_{F,e}$ lower than the theoretical value Γ_F accompanied by an uncertainty on the actual memory parameter of the experiments.

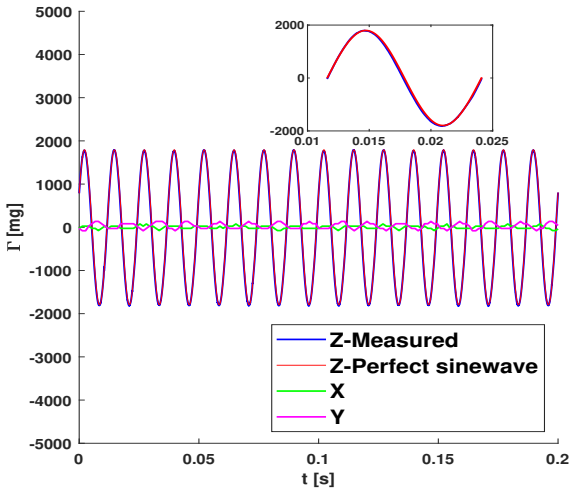

Figure 4.7: Measured vs pure sine normalized acceleration waveforms. The inset is a zoom on one period. The resulting mean square error is $MSE = 2782.6[mg^2] = 2.7826 \cdot 10^{-3}[g^2]$.

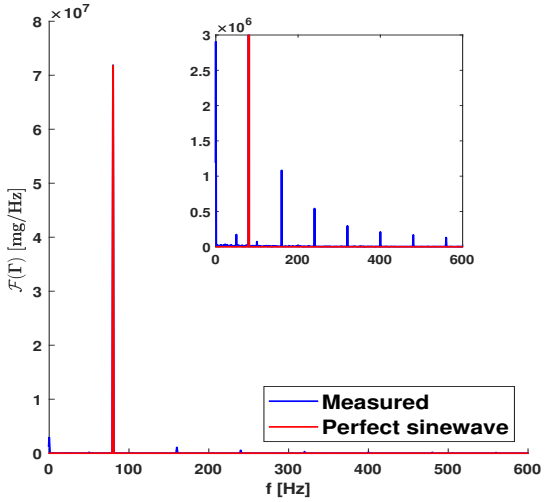

Figure 4.8: Measured vs pure sine normalized acceleration spectra. The inset is a zoom on the harmonics of the measured accemeration.

4.1.2 Droplet on-demand generator

Inspired from reference [40], a piezoelectric *Droplet on-demand generator* (DOD) has been fabricated. The purpose of this DOD is to be able to produce droplets of highly repeatable size ranging from 0.5 to 1.4 [mm] in diameter that will be directly injected in the bath with a launching pad.

A schematic of the fabricated model is shown in Figure 4.9, where the pump and the translation stage from the inspiration model have not been used for practical reasons. However, the model is designed such that the nozzle outlet is aligned with the top of the fluid reservoir ($\Delta h \approx 0$), hence leading to a pressure equilibrium at the nozzle outlet. Also, as the droplet diameter varies only by 1 % after 5000 generated droplets [40] due to a decreasing of the liquid level in the reservoir, the reservoir is simply manually filled in, and the absence of pump is not too disturbing.

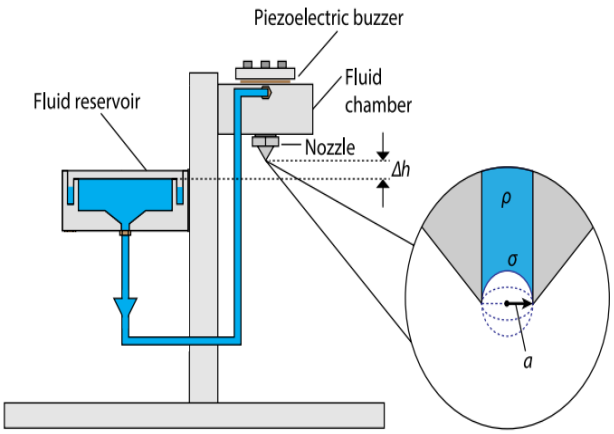

Figure 4.9: Schematic of the constructed DOD, modified from [40]. The inset is a zoom on the nozzle outlet.

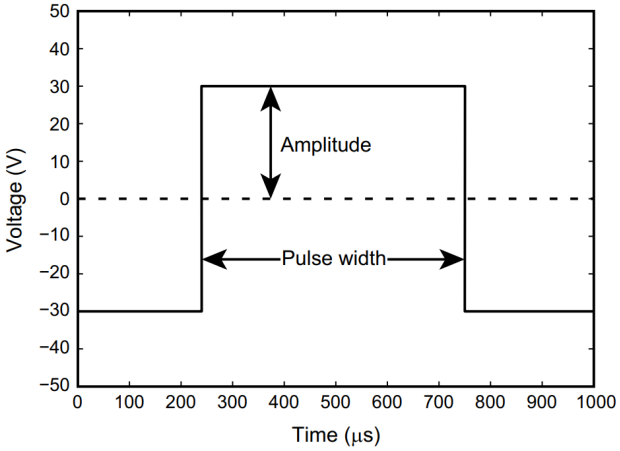

Figure 4.10: Square signal that activates the piezoelectric buzzer in order to generate a single droplet. Taken from [40].

The piezoelectric buzzer [20] is activated with square pulses generated by the switching of a bistable relay controlled by the Arduino Uno. Based on the voltage input by a source ($V_s \in [0, 50]$ [V]) and the command signal coming from the Arduino Uno, the bistable relay passes from applying $-V_s$ to $+V_s$ at the terminals of the piezo. Each time the push button shown in Figure 4.11 is pressed, a square pulse of amplitude V_s and width W_p controllable by the Arduino Uno is applied on the piezo, and a droplet is generated. The LED serves as an indicator. V_{PIN} is also input in the myDAQ to have another indicator on the Labview front panel shown in Figure A.2.

Unfortunately, due to an upper bound for the switching frequency of the used bistable relay, the prescribed [40] pulse width $W_p \sim 600[\mu s]$ in unreachable. As depicted in Figure 4.12, there is a gap between the expected pulse width written in the Arduino code and the measured pulse width at the piezo terminals. The shortest obtained pulse width is around $1000[\mu s]$ before the piezo activation vanishes for shortest Arduino pulse width commands. As shown in Fig. 7 (a) of [40], this often leads either to the generation of multiples droplets in one pulse or to high variations in the generated droplet diameter. This problem is skirted by a proper calibration of the relative position between the DOD and the launching pad such that only one generated droplet enters the oscillating bath.

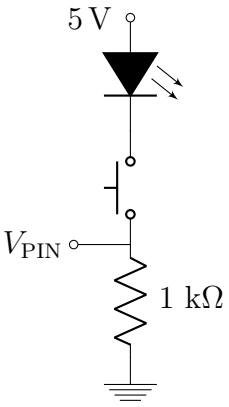

Figure 4.11: Push button montage for generating a droplet.

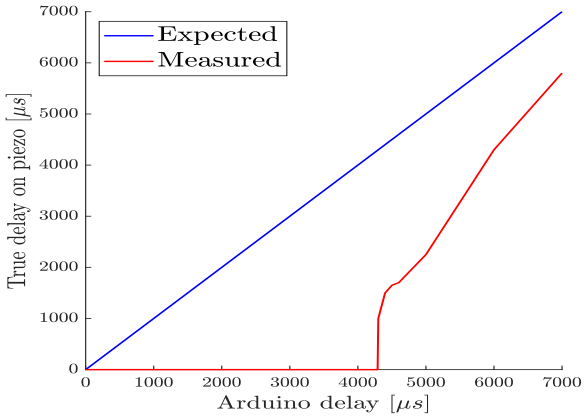

Figure 4.12: Pulse widths gap between the Arduino Uno command and the measured pulse applied at the piezoelectric buzzer terminals.

Regarding the droplet diameter estimation, the "*droplet_fall_analysis.m*" [35] program has been

developed to give an estimation at the output of the nozzle based on image analysis. Different processing steps are applied on the original images to perform the droplet detection, yielding :

Algorithm 2

1. Compute the greyscale difference $I_d[n]$ between the current frame $I[n]$ and the reference frame I_0 (without droplet).
$$I_d[n] = I[n] - I_0 \tag{4.5}$$
2. Convert the image difference into a binary image where the 1's (white pixels) are the pixels p satisfy the following condition[1] :
$$(p > 3\sigma_{I_d})\&\&(p > 3) \tag{4.6}$$
Where σ_{I_d} is the standard deviation of the pixel values of the image difference I_d.
3. Apply *salt and pepper* filtering with a 2x2 square kernel. [30]
4. $$n \leftarrow n + 1 \tag{4.7}$$

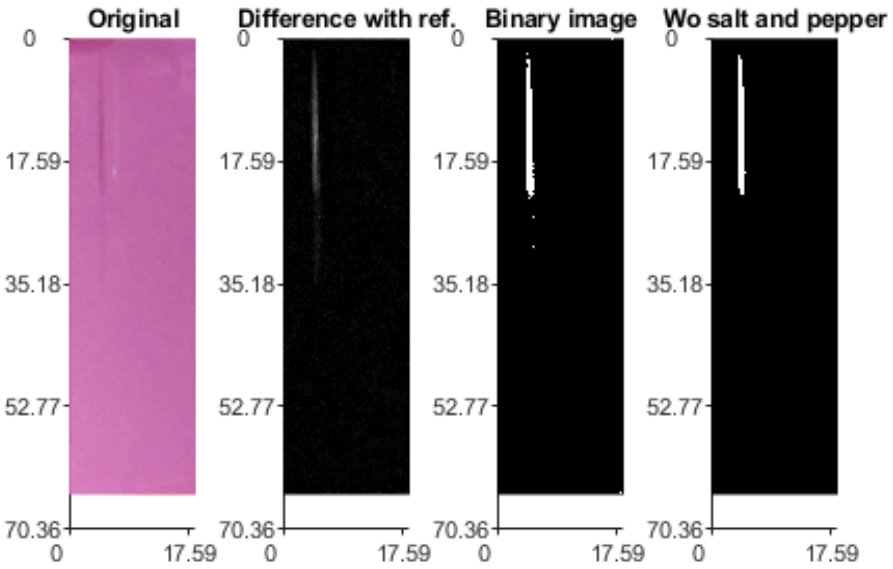

Figure 4.13: Illustration of the droplet detection algorithm results for each step. All the axes are expressed in $[mm]$, with the origin at the top left corner.

The droplet estimation is then given as the mean width of the remaining droplet fall binary image.
In practice, as previously explained, the droplet diameter is rather estimated directly when walking inside the stadium bath. In that case, "*estim_diam.m*" is used. A zoom is applied on the droplet position, and the user is invited to click on two opposite sides of the droplet, typically with 20 different images of the same droplet and the program computes the mean of these estimations. Let us now characterize the droplet generation results.

[1] This condition has been arbitrarily chosen within the ranges of values that fit the eye expectation : $[2.5\sigma_{I_d} - 4\sigma_{I_d}]$ and $[0 - 8]$ for the two lower bounds.

Characterization The estimation of the droplets' diameters is performed by manual selection on multiple images of the same droplet on images with MATLAB. To avoid any bias in the estimation, the different selections are done in randomly selected directions in the 2D plane.

The results in Figure 4.14 show multiple estimations of the diameter of the same droplet on consecutive images coming from the same video sequence. It can be seen that averaging the diameter estimations over 10 selections or more leads to a confidence in the estimation lying in the $[-0.02, 0.02]$ [mm] interval.

In Figure 4.15, we show the estimations of ten different droplets generated with the same droplet generation parameters. It can be seen that the difference between the generated droplets' diameters with the DOD remains lower than $0.1[mm]$ and allows for doing experiments with droplets of approximately the same diameter.

The crucial factor limiting the predictability and repeatability of droplets is the launching pad. Indeed, the droplet output from the nozzle of the reservoir and arriving on the launching pad generally bounces a few times (instead of sliding) before continuing towards the bath, and loses part of its volume on its way. The diameter of the droplet coming in the bath thus highly depends on the position of arrival on the launching pad as well as the launching pad's sliding conditions. These conditions seem practically unpredictable with the current setup configuration and are repeatable only in the short term.

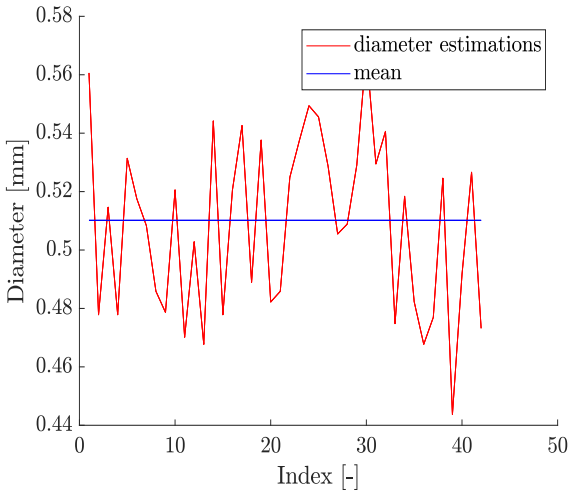

Figure 4.14: Multiple estimations of the diameter of the same droplet on consecutive images coming from the same video sequence. The measured mean is $D_m = 0.51[mm]$ with standard deviation $\sigma_D = 0.032[mm]$ over 43 measurements.

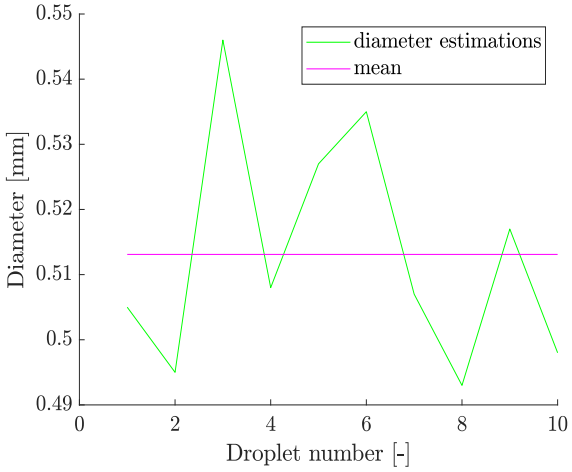

Figure 4.15: Estimations of different droplets' diameters generated with the same parameters (nozzle of diameter $1[mm]$, voltage $V_s = 50[V]$ and pulse width Arduino command $W_p = 4700[\mu s]$) averaged over 20 different images.

4.1.3 Surface visualization

The wave dynamics represent half of the complexity of the walking droplet pilot-wave system. To develop a method in order to estimate the wavy liquid surface profile, at least qualitatively, is a key issue for explaining several phenomena reported in walking droplet experiments. The objectives of this section are to list the different methods that have been investigated, discuss the choices made in the implementations and finally give some experiment results.

Ray deviations

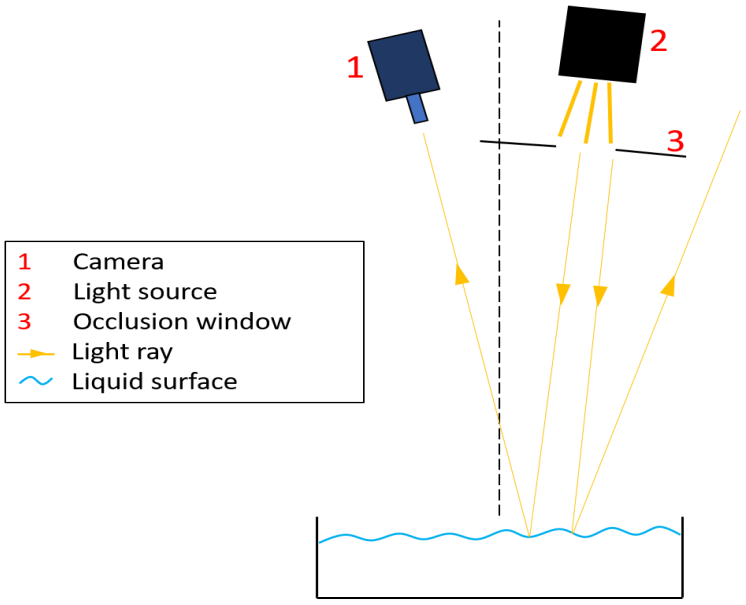

Figure 4.16: Schematic of the experimental montage used for exploiting the ray deviations principle.

The first method that was used to visualize the surface profile of bouncers and walkers [60] consists in exploiting the deviation of the parallel rays emitted by a light source induced by the slope of the liquid surface. As shown in Figure 4.16, the lighting is positioned such that it is directed to reflect on the camera lens if the liquid surface is at rest. If the local slope of the surface is weak, the rays are reflected towards the camera lens and the pixel has a high intensity. On the other hand, for steep slopes, the light rays are strongly deviated and do not go into the camera lens, the corresponding pixels thus appear darker with low intensity. Some alternatives like adding a striped pattern are based on the same principle. [43]

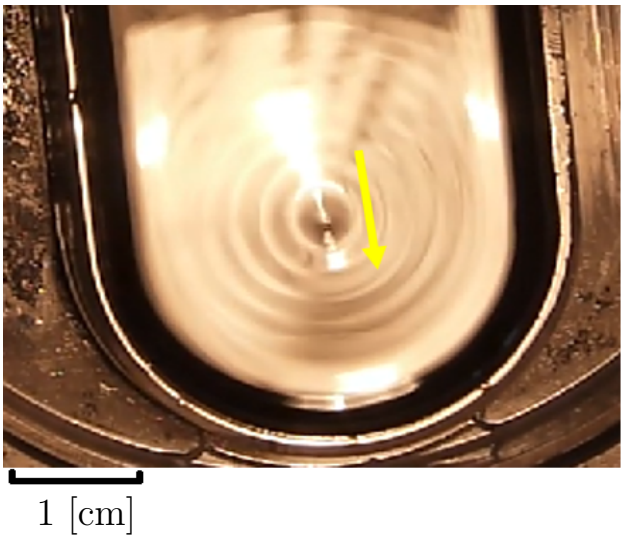

Figure 4.17: Obtained liquid surface wave field for a single walker. The yellow arrow shows the direction of motion of the walker, which can be guessed by the small shift between the droplet's position and the wave field center, as described in [19, 63].

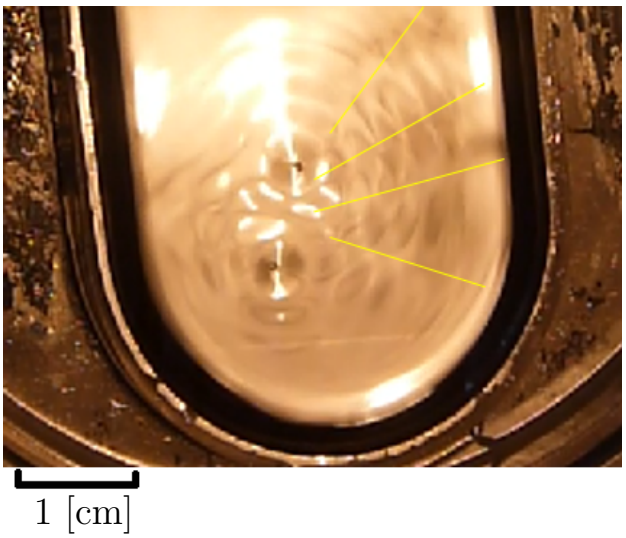

Figure 4.18: Obtained liquid surface wave field for an orbiting pair of walkers. The yellow lines are placed on the apparent destructive interference locations to highlight the interference pattern.

Brewster angle

Another idea, that was not found in the literature for this type of application, is to take advantage of the *Brewster angle* $\theta_B = arctan(n/n_a)$ where $n = 1.4$ and $n_a = 1$ are the refractive indices of the silicone oil and the air, respectively. We thus have $\theta_B = 54.46°$ here. We recall the Fresnel equations for non-magnetic media :

$$\begin{aligned} E_{1r\parallel} &= \frac{n\cos(\theta_2) - n_a\cos(\theta_1)}{n\cos(\theta_2) + n_a\cos(\theta_1)} E_{1\parallel} & E_{2\parallel} &= \frac{2n\cos(\theta_1)}{n\cos(\theta_2) + n_a\cos(\theta_1)} E_{1\parallel} \\ E_{1r\perp} &= \frac{n\cos(\theta_1) - n_a\cos(\theta_2)}{n\cos(\theta_1) + n_a\cos(\theta_2)} E_{1\perp} & E_{2\perp} &= \frac{2n\cos(\theta_1)}{n\cos(\theta_1) + n_a\cos(\theta_2)} E_{1\perp} \end{aligned} \tag{4.8}$$

Where the r, 1, 2, $\parallel$, $\perp$ subscripts stand for reflected, incidence medium, second medium, components parallel and perpendicular to the incidence plane, respectively. θ_1 and θ_2 are the angles of the incident and refracted light rays wrt the normal of the liquid surface plane at rest. As we are interested in the light rays that come from the source and are reflected back into the camera lens, we do not need the two equations from the right hand side. By placing a polarizing filter removing the $\perp$-polarized component in front of the camera, and the light source in Figure 4.16 such that $\theta_1 = \theta_B = 54.46°$ when the surface is plane, the $\parallel$-polarized component of the light rays would be entirely refracted at the interface and no light would go into the camera.

For a typical wave peak-to-peak amplitude of $\Delta_z = 20[\mu m]$ [19] and the wavelength $\lambda_F = 4.72$ [mm], considering a sine wave, the maximum slope is $\pi\Delta_z/\lambda_F = 0.0132277$ [m/m], leading to a deviation angle of the line normal to the liquid surface of $\Delta_\theta = 0.7578°$. The proposition consists in choosing $\theta_1 = \theta_B + \Delta_\theta \approx 55.22°$ to obtain a range as shown in Figure 4.19 where the true incidence angle at each position depends on the slope of the liquid surface on this latter.

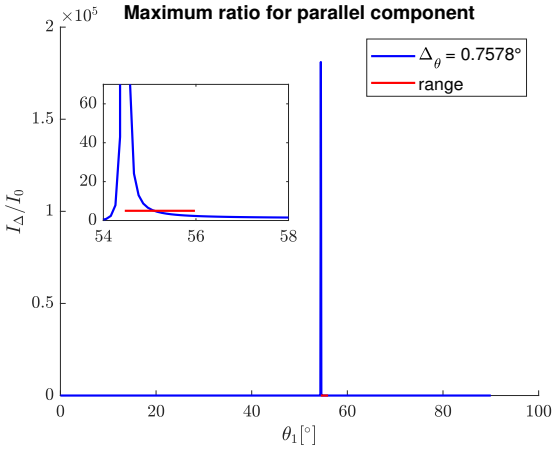

Figure 4.19: Ratio between the intensity received by the camera lens for the positions of steepest slope at the liquid surface I_Δ and the intensity if the liquid surface at rest I_0 for varying incidence angle θ_1. This ratio tends to infinity at the Brewster angle as it corresponds to $I_0 = 0$, announcing a good contrast between weak and steep slopes. The inset is a zoom on the active range of effective incidence angles that will be possible.

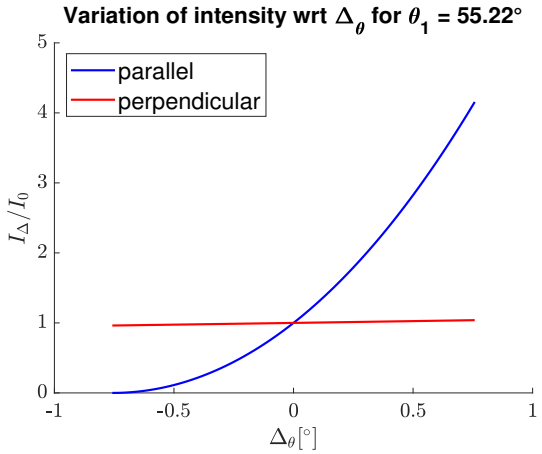

Figure 4.20: Ratio between the intensity I_Δ received by the camera lens for varying deviation angles Δ_θ and the intensity if the liquid surface at rest I_0 for a fixed incidence angle of $\theta_1 = 55.22°$. One observes the ratio tends to zero as the effective incidence angle tends to θ_B for negative slopes. It can be seen that the sensitivity is better for positive slopes with this method.

This method has not been tested because of a lack of necessary material (polarizing filter, big lenses, ...). The extension of this proposition to the 2D case has not been studied.

Schlieren method

"Schlieren photography (from German; singular "Schliere", meaning "streak") is a visual process that is used to photograph the flow of fluids of varying density. The classical implementation of an optical schlieren system uses light from a single collimated source shining on, or from behind, a target object. Variations in refractive index caused by density gradients in the fluid distort the collimated light beam. This distortion creates a spatial variation in the intensity of the light, which can be visualised directly with a shadowgraph system." [85]

Two Schlieren based methods were investigated for the liquid surface profile reconstruction :

- The Phase-shifting schlieren (PSS) method [32, 64] which consists in placing an intensity filter in front of the camera, such that the light rays slightly deviated by the liquid surface appear brighter or darker depending on the deviation. As for the *Brewster angle* based method, this one was not implemented for practical reasons. However, as no article was found in the literature to discuss the 2D case, an extension to the recovery of the 2D surface is proposed in Figure 4.23.

- The Free-surface synthetic schlieren method [31, 53, 54, 66] which consists in comparing the obtained pattern in the current image to a reference pattern when the liquid is at rest to compute the displacement of each individual pixel of the reference pattern. These displacements are directly related to the gradient of the liquid surface at position, a quantitative estimation of the liquid surface is finally obtained by computing the inverse gradient of the displacement field. This method has been implemented and gives satisfying results, see below.

PSS The working principle of this system is shown in Figure 4.21. The linear filter shown in Figure 4.22 is an example, where other types of response curves could be exploited like sinusoidal ones. The main drawback of this method is that the response curve is only valid for one direction. Variable neutral density filters exist in 2D, but with the filtering variation corresponding to an angular variation around the image plane center, the information on the deviation magnitude is lost.

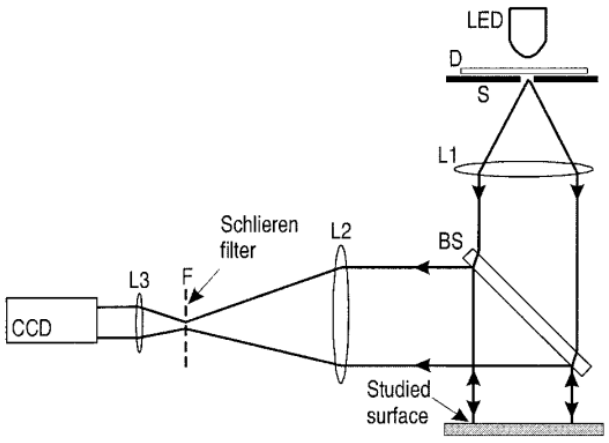

Figure 4.21: Schematic drawing of the Schlieren system working in reflection. Taken from [32]

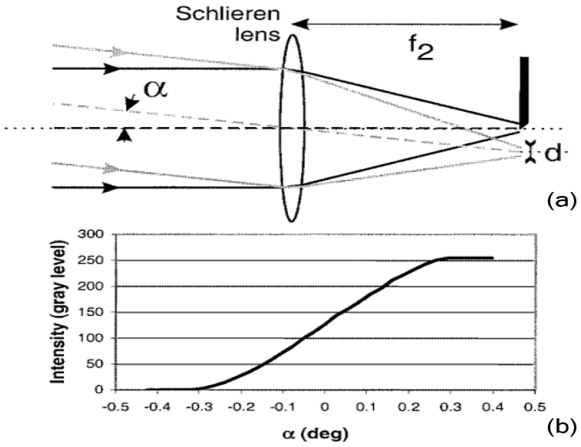

Figure 4.22: Conventional Schlieren:(a) arrangement of the knife-edge,(b) typical response curve. Taken from [32]

The proposed way to extend this principle to the 2D case, is to deal with multiple colors simultaneously. Either a 2D rainbow optical filter could be used, varying the color filtering with the deviation magnitude and the intensity filtering with the deviation orientation or conversely. Or, as shown in the proposal in Figure 4.23, the 1D principle could be extended by assigning a color for one direction (in that case, blue for deviations along $\hat{e}_x$) and another one for the second direction (in that case, red for deviations along $\hat{e}_z$). The supplementary materials needed wrt Figure 4.21 are 2 beam-splitters, 2 color filters and 3 mirrors. The basic idea behind this proposal is to reorient the second direction along the first, such that they both benefit from the filter contribution. The red deviated rays arrive rotated by 90° in the CCD, which can be simply corrected during the image processing.

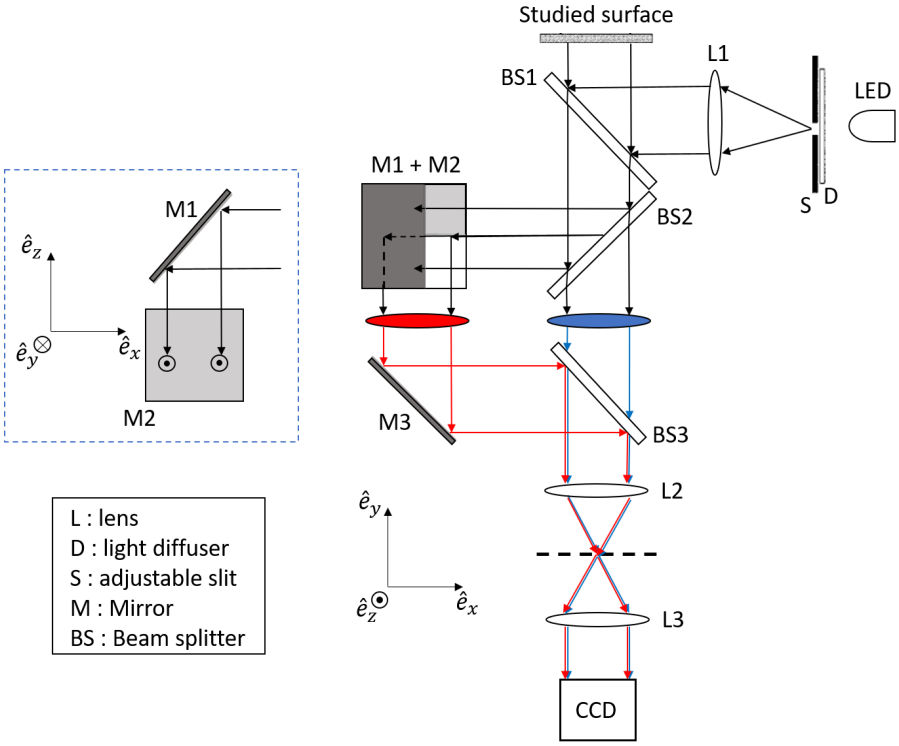

Figure 4.23: Schematic of the proposed montage for a 2D free surface recovery with the PSS method.

FS-SS The Free-surface Synthetic Schlieren method was the one implemented in this work because of its advantages regarding the necessary material, cheapness and theoretical background. The following results are taken from ref. [53] and will support the discussion on the validity of the assumptions made in the current implementation.

The objective is to find the optical displacement field $\delta\mathbf{r} = \mathbf{M'M"}$ of each object point M, where M' and $M"$ correspond to the virtual objects for flat and deformed interface respectively, induced by the refraction of the light scattered from a pattern located at $z = 0$ through the interface $z = h(x, y)$. Once the displacement field has been obtained, we need to relate it to the surface gradient ∇h of the surface. The obtained relationship between the free surface gradient and displacement field is :

$$\nabla h = -\frac{\delta\mathbf{r}}{h^*}, \quad \text{with} \quad \frac{1}{h^*} = \frac{1}{\alpha h_p} - \frac{1}{H} > 0 \tag{4.9}$$

Where $\alpha = 1 - \frac{n_a}{n}$, $h_p = h_0 + \frac{n}{n_g}h_g + \frac{n}{n_a}h_a$ is the effective surface-pattern distance, taking eventual glass and air layers between the dot-pattern and the liquid into account, and H is the pattern-camera distance.

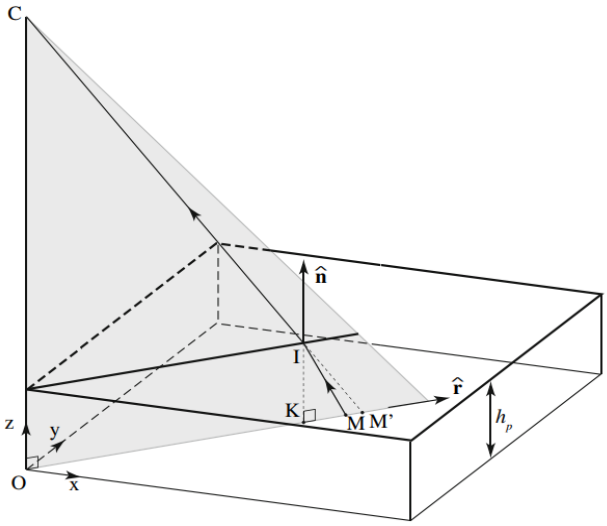

Figure 4.24: Three-dimensional ray geometry for a horizontal interface (reference case). Taken from [53].

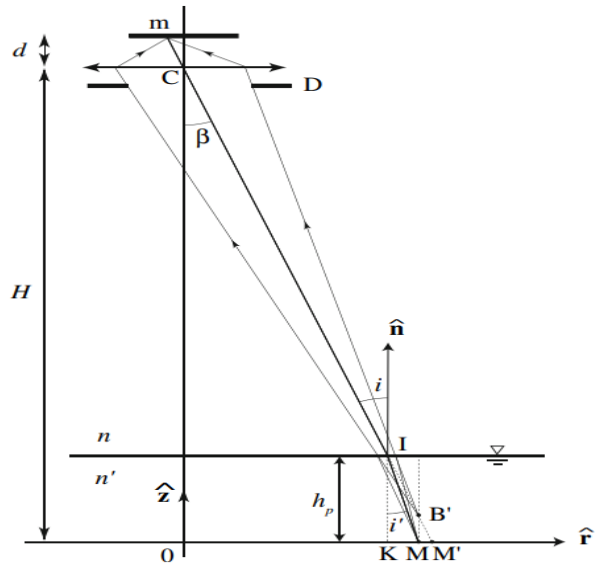

Figure 4.25: Two-dimensional view of the vertical incidence plane COM. A ray coming from a point M located on the pattern appears to come from the virtual object B'. In the pattern plane, it appears to come from the point M. Taken from [53].

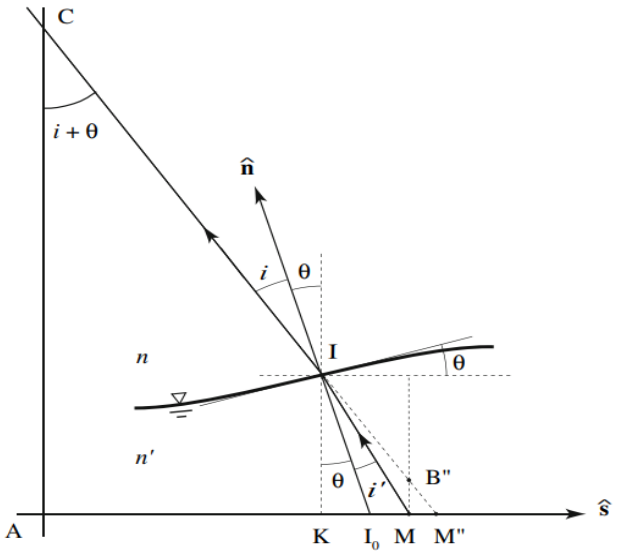

Figure 4.26: Two-dimensional view of the incidence plane CAM. A ray coming from M appears to come from the virtual object B". In the pattern plane, it appears to come from the point M". Taken from [53].

Behind eq. (4.9), three approximations were considered :

- *Paraxial approximation* The pattern-camera distance H is much larger than the field size L, yielding a maximum paraxial angle $\beta_{max} \simeq L/(\sqrt{2}H) \ll 1$. In the actual experimental setup, we have $\beta_{max} \simeq 7.6/(\sqrt{2}62) = 0.0867[rad] = 4.9°$. This value is considered as a good tradeoff as the approximation remains reasonably valid and increasing H may cost more difficulties in the manual handling of the camera and a decreasing of its fixation stability.

- *Weak slope approximation* The angle γ between the unit vector normal to the interface $\hat{\mathbf{n}}$ and the vertical vector $\hat{\mathbf{z}}$ is small. As a consequence, the surface slope θ measured in the incidence plane is also small. As discussed with the *Brewster angle* method, we typically have $\theta = 0.7578°$.

- *Weak amplitude approximation* Denoting $h(x, y) = h_p + \eta(x, y)$ the surface height, the amplitude $|\eta|$ is small compared to the mean height h_p. As discussed with the *Brewster angle* method, we typically have $|\eta| = 10[\mu m]$ and $h_p > 6[mm]$, yielding a ratio of 0.16%.

The invertibility condition, which requires that the focal length associated to the surface curvature is larger than the surface-pattern distance everywhere in the imaged field, is verified with :

$$h_{p,max} = 11[mm] < h_{p,c} = \frac{\lambda_F^2}{4\pi^2 \alpha \eta_0} = 197.5[mm] \tag{4.10}$$

Now that the assumptions have been verified, it remains to discuss the reference pattern design and the method for estimating the displacement field. About the reference pattern, a set of randomly distributed dots, partially overlapping, is used. In the example shown in Figure 4.27, dots of diameter 0.3 [mm], made of concentric circles of increasing grayscale, with an overall black-on-white density ratio of approximately 1:2, have been numerically generated with "*makebospattern.m*". The "*makebospattern.m*" code has been slightly modified to add the possibility of generating a RGB dot pattern, which may reduce the ambiguity of points association (not exploited in this work).

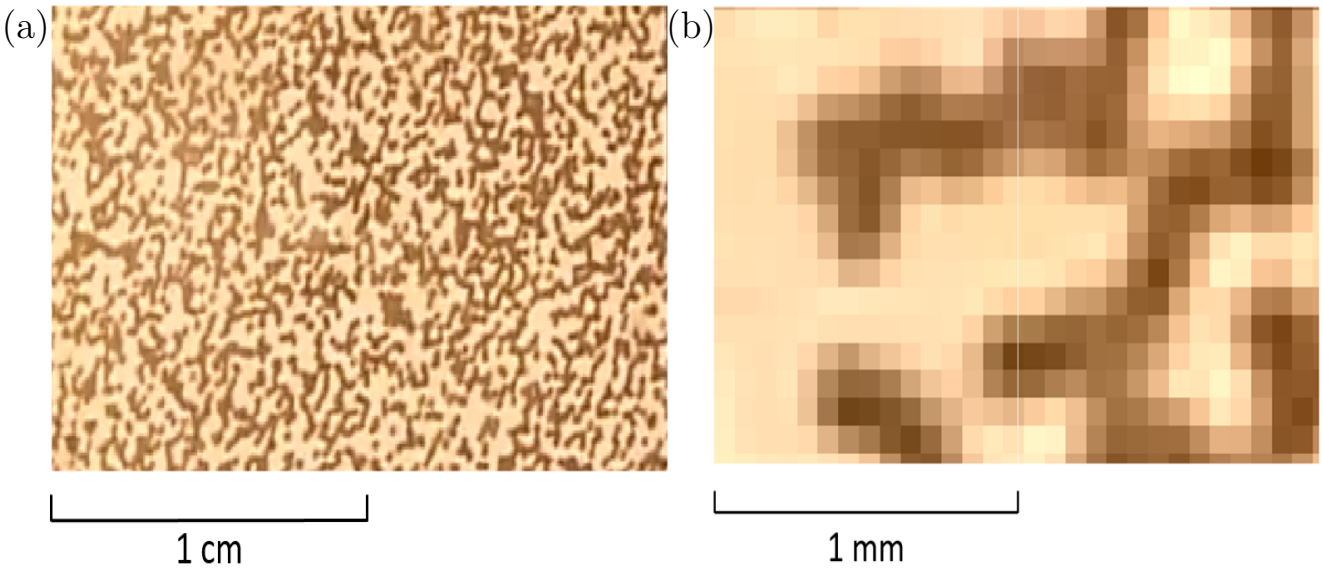

Figure 4.27: Random dot pattern used in the present experiments, as imaged by the 1080x720p camera in the stadium bath. Dots of diameter $d = 0.3$ [mm] were numerically generated, with a density of 50%, resulting in dots of approximately 5 pixels in the camera sensor. (a) 2 [cm] wide window showing the density (b) zoom on a 2 [mm] wide window, highlighting the varying grayscale of the dots. We observe a lower resolution than in Fig. 7(b) in [53].

The displacement field is finally obtained by using a rewritten DIC algorithm (see "*Surface_Visu_Correlation.m*") for points association between the reference pattern image and the deformed one. The user can select the ROI where the liquid surface estimation will be performed, which can be any rectangle in the original image. Interrogation windows of size 16x16 pixels are used for the computations of the correlation functions. The displacement for point (a, b) of the reference image is obtained as :

$$\begin{aligned}
\delta\mathbf{r}_{(a,b)} &= argmax_{(u,v)}(f \odot g)(u,v) \\
&= argmax_{(u,v)} \frac{\sum_{(i,j)\in S_{(a,b)}} (f(i,j) - f_m)\,(g(i+u, j+v) - g_m)}{\sqrt{\sum_{(i,j)\in S_{(a,b)}} [f(i,j) - f_m]^2 \sum_{(i,j)\in S_{(a,b)}} [g(i+u, j+v) - g_m]^2}} \\
&= argmax_{(u,v)}(\tilde{f} * \tilde{g})(-u,-v) \\
&= argmax_{(u,v)} \mathcal{F}^{-1}\left\{\mathcal{F}\{\tilde{f}\} \cdot \mathcal{F}\{\tilde{g}\}\right\}(-u,-v)
\end{aligned} \tag{4.11}$$

With :

$$f_m = \frac{1}{n(S)} \sum_{(i,j)\in S_{(a,b)}} f(i,j), \qquad \tilde{f}(i,j) = \frac{f(i,j) - f_m}{\sum_{(i,j)\in S_{(a,b)}} [f(i,j) - f_m]^2} \tag{4.12}$$

And similarly as eq. (4.12) for g. f (resp. g) denotes the reference pattern (resp. current observed) image in grayscale. The subscript m stands for the mean pixel value in the interrogation window $S_{(a,b)}$ with $n(S)$ being the number of pixels in this window (here 16x16), and $\tilde{f}(i,j)$ is the normalized reference pattern. The $\odot$ symbol denotes the normalized 2D cross-correlation operation (N2DCC), $*$ denotes the convolution operator while $\cdot$ denotes the pointwise product and $\mathcal{F}$ denotes the Fourier transform. The Fourier transform is performed with the FFT algorithm and only aims to reduce the computing complexity from $\mathcal{O}(N^4)$ to $\mathcal{O}(N^2 \log(N^2))$ for a two dimensional function, yielding a computing time reduction of 32 for a 16x16 interrogation window. The obtained gradient is finally inverted using a least-squares criterion with "*intgrad2.m*".

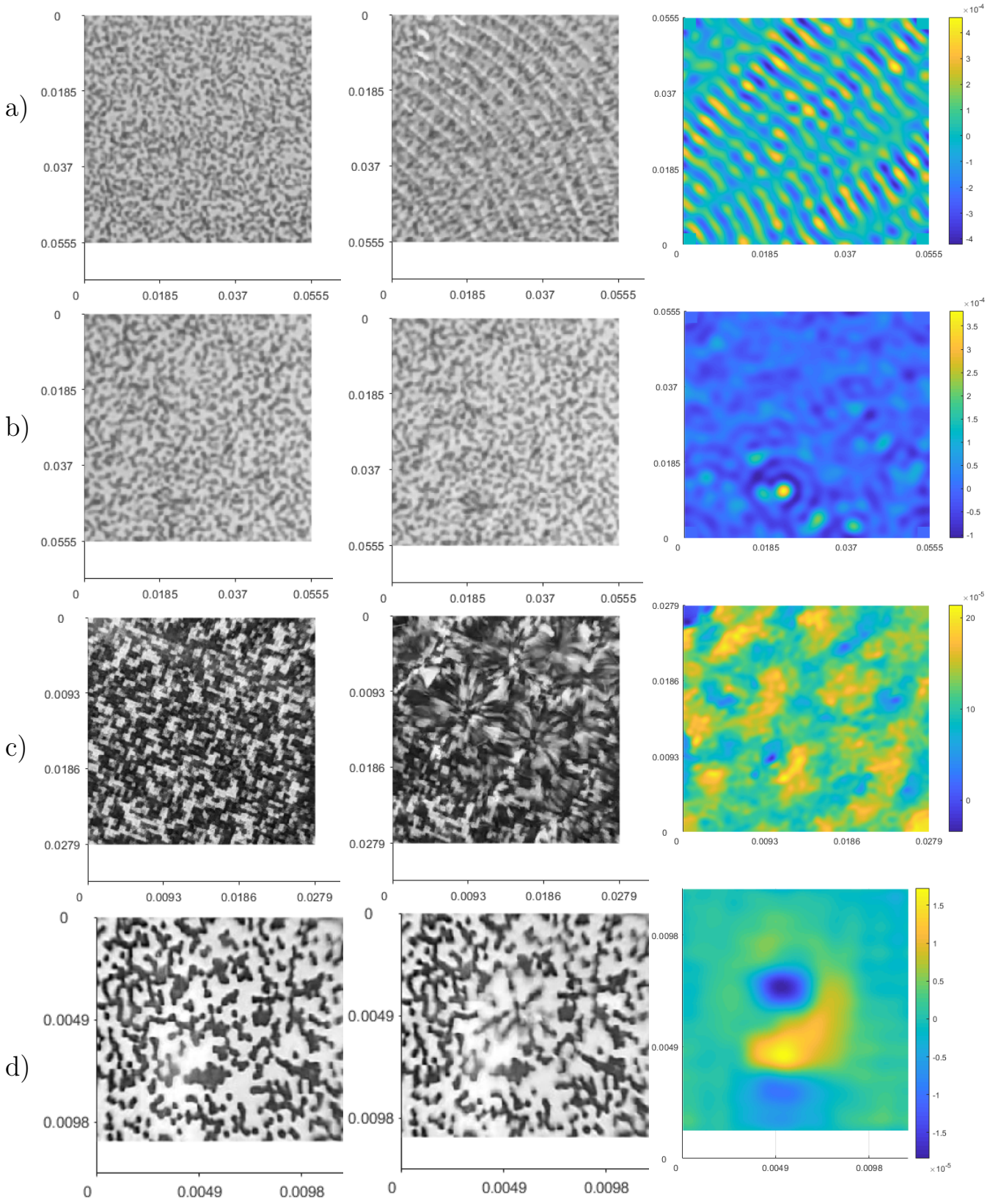

Figure 4.28: DIC based surface profile recovery results. The labels are removed for visibility issues. All the axes are expressed in $[m]$ with the origin at the top left corner. For each row, the image on the left is the reference pattern, the one on the center is the modified image and the surface estimation is given on the right. (a) Faraday planar wave (b) Droplet bounce (c) Faraday gridlike wave (d) typical crest created by a droplet bounce.

In the results given in Figure 4.28, we observe that (a) and (c) look closer from the true liquid surface. This can be explained by the bigger amplitude of the waves when passed the Faraday instability threshold, a bigger amplitude unavoidably means steeper slopes and finally longer horizontal displacements of the points in the deformed image. Indeed, with the resolution of the current camera, the longest point displacement is between one and two pixels, what is definitely not enough for a smooth and accurate reconstruction. Note that no interpolation to the subpixel level has been performed. Moreover, the temporal resolution of the camera (25 FPS) is not able to capture the surface waves with typical phase velocity $v_F^\phi = 190.8[mm/s] = 7.632[mm/image]$, the results from Figure 4.28 represent the currently established stationary waves only.

Although this method gives satisfying results for the wave surface recovery, its intrinsic black and white looking uniformity can significantly deteriorate the droplet tracking. One way to avoid this issue may come from the opportunity to use a more sophisticated reference pattern with the DNN based surface recovery described here below.

DNN based

A more recent approach proposed in [72] consists in giving the reference pattern and refraction image as input to a neural network for the surface profile estimation. The network architecture is called FSRN for Fluid Surface Reconstruction Network and "consists of two sub-nets : 1) an encoder-decoder based convolutional neural network (FSRN-CNN) for per-frame depth and normal estimation and 2) a recurrent neural network (FSRN-RNN) for enforcing the temporal consistency across multiple frames". Different loss functions are combined in the architecture, each one aiming to optimize the consistency of the depth map, normal map or with the related physics.

Moving to this type of fluid surface reconstruction would allow to replace the black and white dot pattern used in Section 4.1.3 by a smoother one, thus improving the droplet tracking performances. An attempt to contact the authors was made to obtain the open-source code and training datasets that were not available yet on their website, but did not receive any answer.

4.1.4 Droplet tracking

In order to automatize the observations made on walkers, the usual technique is to use the images taken by the camera, and to apply image processing tools to quantify the results. For the detection of the droplet position in the vibrating bath, a *droplet tracking* algorithm is necessary. A first unavoidable step requires calibrating the lighting configuration of the bath, trying to increase the contrast between the walking droplet and the background. With the light ray deviation technique (Figures 4.17 and 4.18) this contrast is clearly sufficient (discussion on Figures 4.32 and 4.33). With the random black and white dot pattern used for the surface recovery, this is more challenging. Indeed, it is difficult to increase the contrast between the droplet and the background while uniformly lighting the bath. The usual technique to deal with this it consists in lighting the bath with grazing incidence. This is not possible with the current setup (see Figure 4.1). In this section, we give a mathematical description of the tracking implementation accompanied with the intuition behind and give quantitative analysis, also by comparison with manually computed trajectory serving as ground truth.

For each frame n, the droplet's center $\mathbf{c}$ is chosen as :

$$\mathbf{c}[n] = \arg\max_{[x,y]} \quad g_n[x, y] \tag{4.13}$$

Where :

$$g_n[x,y] = \left|(\mathbf{I}_n|_{\mathcal{R}_n} - \mathbf{I}_{n-1}|_{\mathcal{R}_n})[x,y] \cdot \mathcal{F}^{-1}\left\{\mathcal{F}\{\mathbf{I}_{n-1}|_{\mathcal{C}_n}, \mathcal{R}_n\} \cdot \mathcal{F}\{\mathbf{I}_n|_{\mathcal{R}_n}\}\right\}[x,y]\right| \tag{4.14}$$

Where a bold font denotes a vector or a matrix, $\mathbf{I}_n|_{\mathcal{R}}$ is the image at integer time frame n limited to the region of interest, $\mathcal{F}$ denotes the Fourier transform operator, R_n and $\mathcal{C}_n$ denote the ROI and correlation zone sets of coordinates at time frame n, respectively.

In eq. (4.14), the metric that is maximized is the combinination (pointwise product) of an image difference and a correlation.
The first term $(\mathbf{I}_n|_{\mathcal{R}_n} - \mathbf{I}_{n-1}|_{\mathcal{R}_n})[x,y]$ computes the difference between the current and the previous frame, in the ROI $\mathcal{R}_n$. The intuition behind this is that the walker's displacement should induce a high intensity variation at its current and previous locations. This image difference is shown in Figure 4.29 (d).
The second term $\mathcal{F}^{-1}\left\{\mathcal{F}\{\mathbf{I}_{n-1}|_{\mathcal{C}_n}, \mathcal{R}_n\}\mathcal{F}\{\mathbf{I}_n|_{\mathcal{R}_n}\}\right\}[x,y]$ computes the DIC between the blue box in Figure 4.29 and R_n in the current image $\mathbf{I}_n$. The Fourier transform has the same purpose as in eq. (4.11), i.e. reduce the computational cost. The second input parameter in the Fourier transform in $\mathcal{F}\{\mathbf{I}_{n-1}|_{\mathcal{C}_n}, \mathcal{R}_n\}$ stands for the padding to the size of $\mathcal{R}_n$. Note that the correlation is normalized at the end, as viewed in Figure 4.30.

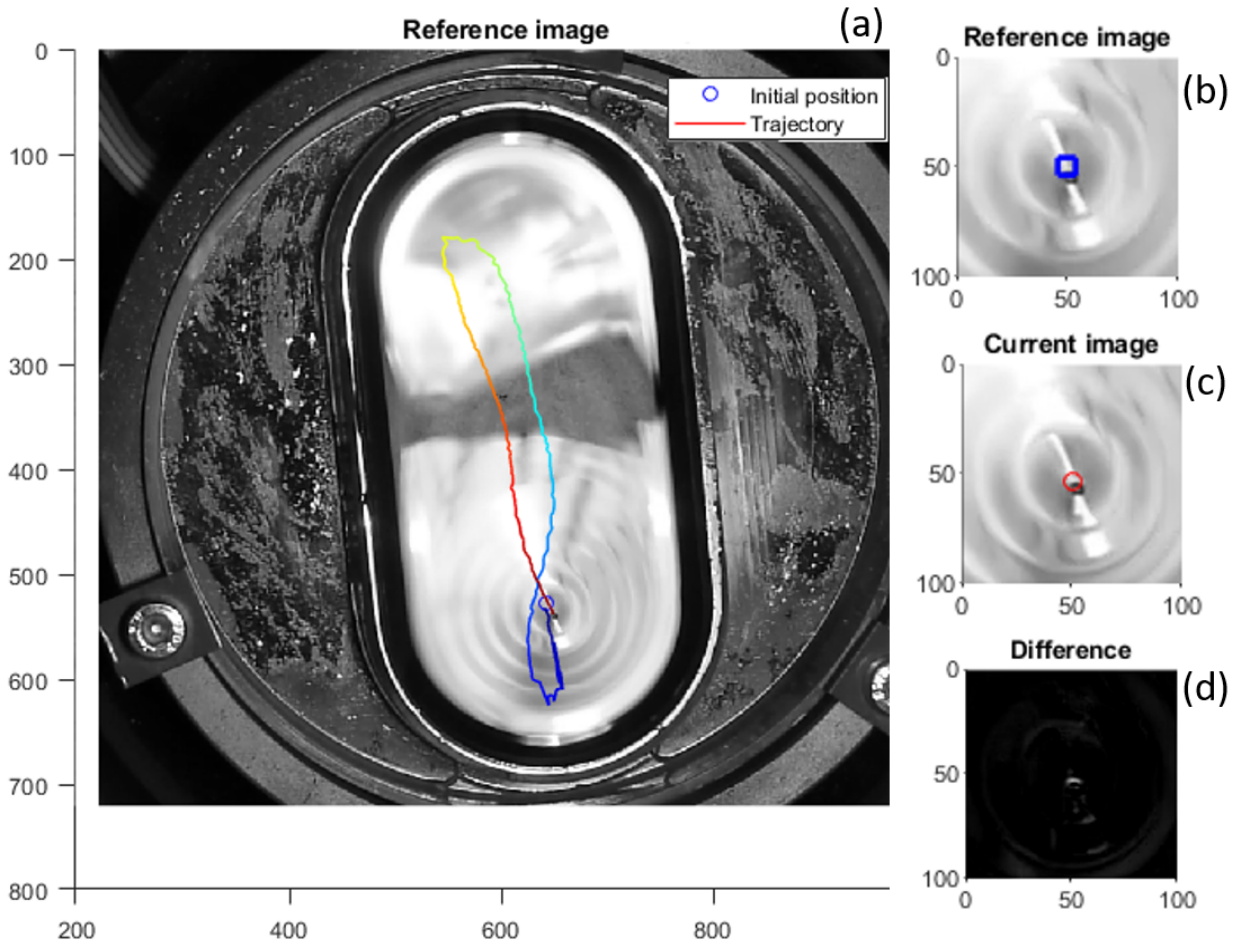

Figure 4.29: Tracking algorithm display. The axes are expressed in pixel values for this display. (a) Final full frame with the computed trajectory. The color is varying along the trajectory to give qualitative information of the time spent at a given place. (b) ROI $\mathcal{R}_n$ with the correlation zone $\mathcal{C}_n$ delimited by the blue box (c) ROI with the currently computed droplet's position, marked by a red circle (d) Image difference $(\mathbf{I}_n|_{\mathcal{R}_n} - \mathbf{I}_{n-1}|_{\mathcal{R}_n})[x,y]$.

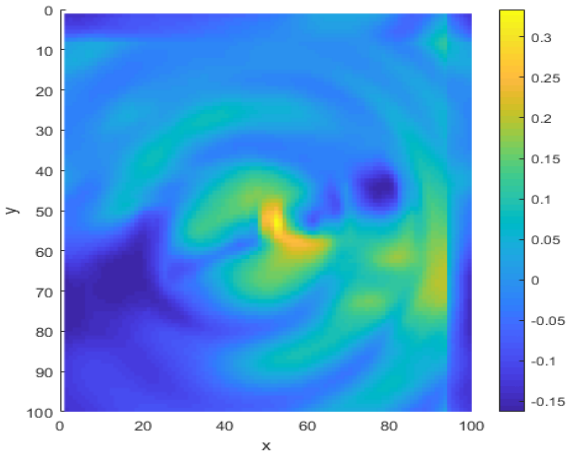

Figure 4.30: Result of the correlation $\mathcal{F}^{-1}\left\{\mathcal{F}\{\mathbf{I}_{n-1}|_{\mathcal{C}_n}, \mathcal{R}_n\}\mathcal{F}\{\mathbf{I}_n|_{\mathcal{R}_n}\}\right\}[x, y]$ normalized at the end. The axes are expressed in pixel values for this display. One observes multiple sets of local maxima, that will be discriminated thanks to the image difference contribution. The axes are expressed in pixel values for this display.

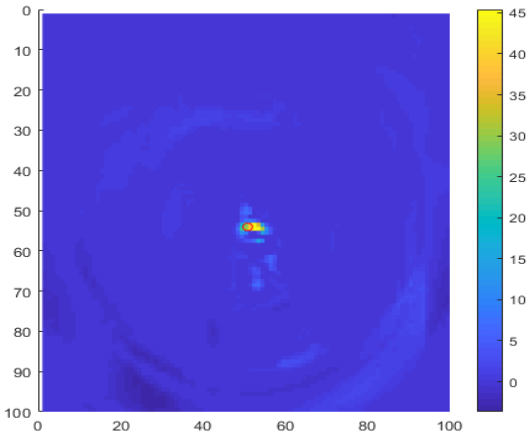

Figure 4.31: Final obtained metric $g_n[x, y]$, with $\mathbf{c}[n]$ marked by a red circle. The axes are expressed in pixel values for this display. One observes the constructive combination between the image difference and the correlation, removing the ambiguities of both. The axes are expressed in pixel values for this display.

The results in case of ray deviation lighting are shown in Figures 4.32 and 4.33. One can see the computed trajectory accurately follows the ground truth. Most of the oscillations are narrower than the actual droplet, and consequently depend on the position of the detected point inside the droplet. From Figure 4.33, it can be viewed that most errors are around 3 pixels wide (0.35 [mm] in this analysis). A couple of outliers are present yet, always induced by parasite reflections due to an non perfect illumination. However, the latter do not affect the assignment correspondence with the true trajectory. They could simply be identified because of their unnatural spacing with the rest of the trajectory and replaced by an interpolation of the other locations.

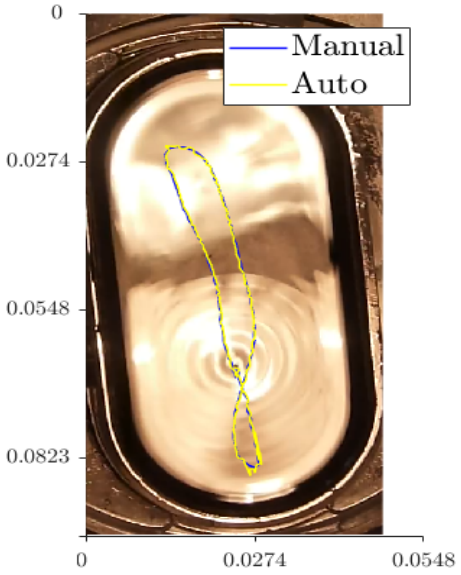

Figure 4.32: Comparison between manually and automatically computed trajectories. For the first case, the droplet center was manually selected on each frame, for the second one, the positions were numerically computed with eq. (4.14). Both axes are expressed in $[m]$.

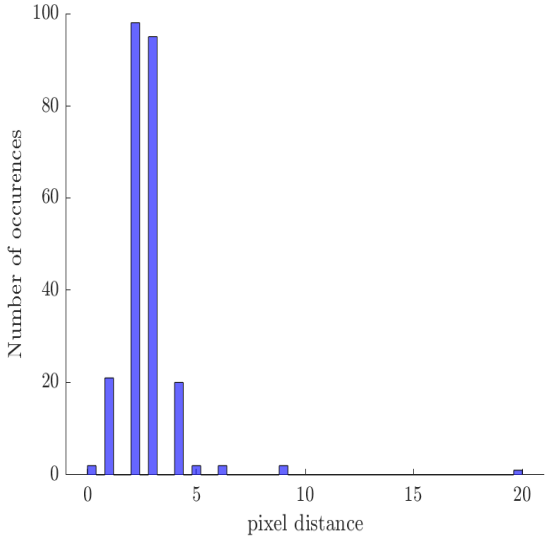

Figure 4.33: Histogram of the droplet position error in pixels for the trajectory in Figure 4.32.

The results in case of dot pattern surface recovery lighting are shown in Figures 4.34, 4.35 and 4.36. One can see the computed trajectory also follows the ground truth, but with more deviations due to correlation. From Figure 4.36, it can be viewed that most errors are around 5-6 pixels wide (0.7 [mm] in this analysis) which is twice bigger than in the ray deviation illumination case and which is the order of magnitude of the droplet's diameter. Some outliers, i.e. detected positions very far from the total detected trajectory, may still be removed. This worsening of the tracking supports the interest given for a DNN based approach for the surface recovery given in Section 4.1.3.

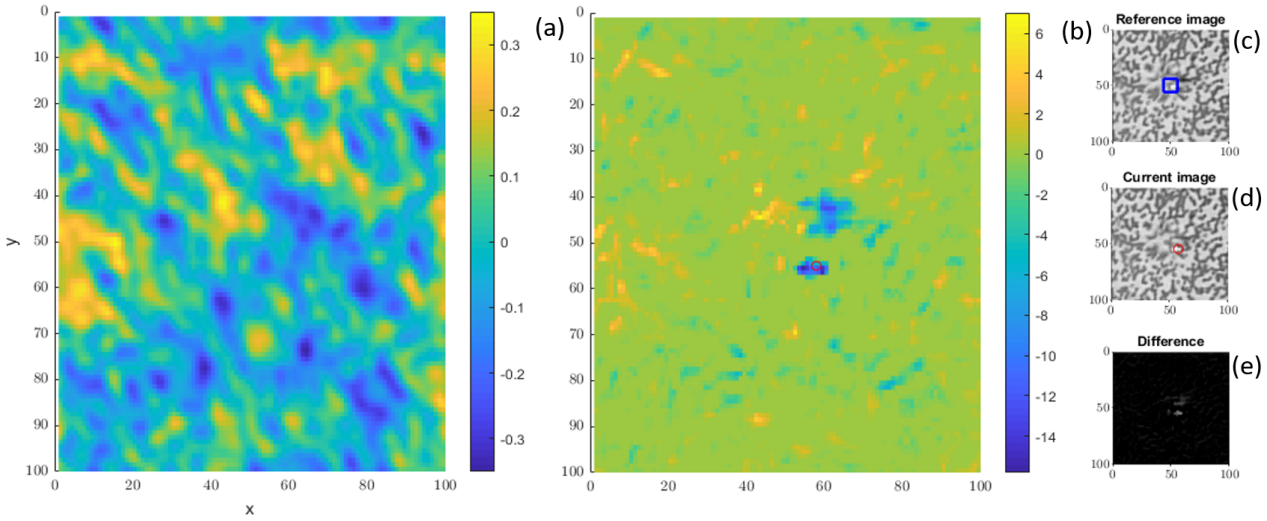

Figure 4.34: Tracking algorithm display for the dot pattern case. (a) Result of the correlation. (b) final obtained metric $g_n[x, y]$, with $\mathbf{c}[n]$ marked by a red circle. (c) ROI $\mathcal{R}_n$ with the correlation zone $\mathcal{C}_n$ delimited by the blue box (d) ROI with the currently computed droplet's position, marked by a red circle (e) Image difference $(\mathbf{I}_n|_{\mathcal{R}_n} - \mathbf{I}_{n-1}|_{\mathcal{R}_n})[x, y]$. The axes are expressed in pixel values for this display.

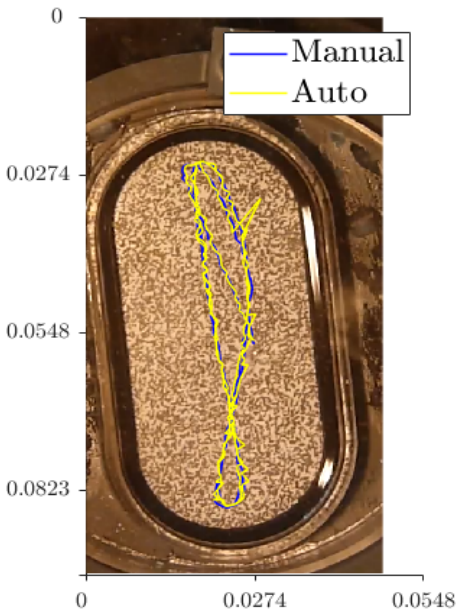

Figure 4.35: Comparison between manually and automatically computed trajectories. For the first case, the droplet center was manually selected on each frame, for the second one, the positions were numerically computed with eq. (4.14). Both axes are expressed in $[m]$.

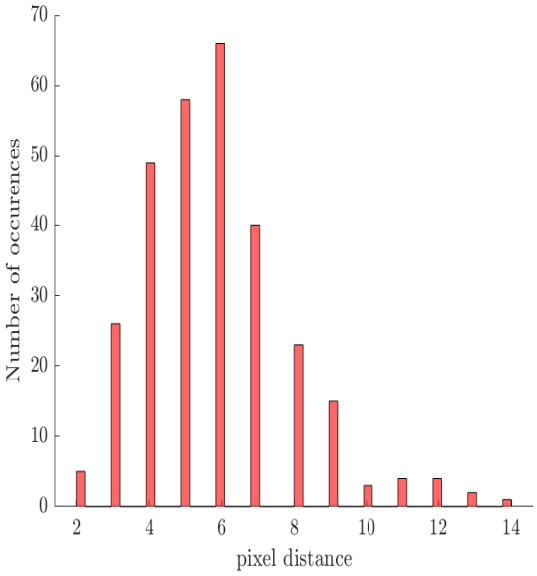

Figure 4.36: Histogram of the droplet position error in pixels for the trajectory in Figure 4.35.

Because of noisy reflections due to the way the bath and the droplet are illuminated, the correlation values were jugded unsufficiently reliable thus the method proposed in [59] to interpolate the droplet position to a subpixel level was not considered.

4.2 Validation

An important remark on the described setup is that the observed Faraday instability threshold occurs for a non dimensional acceleration amplitude of $\Gamma = 2350[mg]$ instead of the theoretical prediction of $\Gamma_F = 4144[mg]$. In front of this issue, the oscillation frequency has been checked by acoustics with the Android app *Phyphox*. The vertical actuation amplitude has also been verified with *Phyphox* by sticking a smartphone on the bath and comparing the measurement with the accelerometer output. Finally, the viscosity of the silicone oil has been estimated with the falling ball method according to [1] yielding $\hat{\mu} = 19.6[mPa.s] \approx \mu = 19[mPa.s]$. To ensure a good damping of the surface waves induced by the borders, the stadium well has been printed in 3D, with a liquid height outside the well $h_1 < 1[mm]$ and a minimal distance between the well and the borders of the bath of $7[mm]$.

This discrepancy is thought to be due to an imperfect horizontality of the bath, where as shown in Fig. 4 of [37] even a small component of the actuation in the horizontal plane of the bath leads to a saturation of the surface waves vanishing. In the measurement in Figure 4.7, we can indeed observe a non negligible component along the Y-axis of amplitude $\approx 120[mg]$. Consequently, as the dependency of the memory parameter Me on the tilt of the bath is unknown, it is chosen to give an estimation of this tilt in terms of *Roll-pitch-yaw* rotation convention and to **simply give the non-dimensional acceleration peak Γ measured along the Z-axis** (as the two other components can be deduced from the rotation).

The objective is to find, from the measurements in Figure 4.7, the tilt angles associated to the rotation matrix $\mathbf{R}(\alpha, \beta, \theta) = \mathbf{R}_z(\alpha)\mathbf{R}_y(\beta)\mathbf{R}_x(\theta)$, where we assume no rotation around the Z-axis (hence $\alpha = 0$), such that the measured 3-axis acceleration $[X', Y', Z']^T$ is related to the truly applied acceleration $[0, 0, Z]^T$ as :

$$\begin{bmatrix} X' \\ Y' \\ Z' \end{bmatrix} = \mathbf{R}(\alpha = 0, \beta, \theta) \begin{bmatrix} 0 \\ 0 \\ Z \end{bmatrix} = \begin{pmatrix} c\beta & s\beta s\theta & s\beta c\theta \\ 0 & c\theta & -s\theta \\ -s\beta & c\beta s\theta & c\beta c\theta \end{pmatrix} \begin{bmatrix} 0 \\ 0 \\ Z \end{bmatrix} = \begin{bmatrix} s\beta c\theta Z \\ -s\beta Z \\ c\beta c\theta Z \end{bmatrix} \tag{4.15}$$

where s and c stand for the sine and cosine operations, respectively. θ is directly deduce from the mean $m_{Y'}$ of Y' due to the gravity acceleration :

$$\theta = arc\sin\left(\frac{m_{Y'}}{m_{Z'}}\right) = arc\sin\left(\frac{70}{981}\right) = 4.09° \tag{4.16}$$

and β is obtained by dividing the first line of eq. (4.15) by the third :

$$\beta = arc\tan\left(\frac{X'}{Z'}\right) = arc\tan\left(\frac{80}{1795}\right) = 2.55° \tag{4.17}$$

This tilt cannot be cancelled because of the lack of suitable material. This means that there is an uncertainty on the current memory parameter Me, also inducing issues regarding the reproducibility of the obtained experiments results.

4.3 Results and discussion

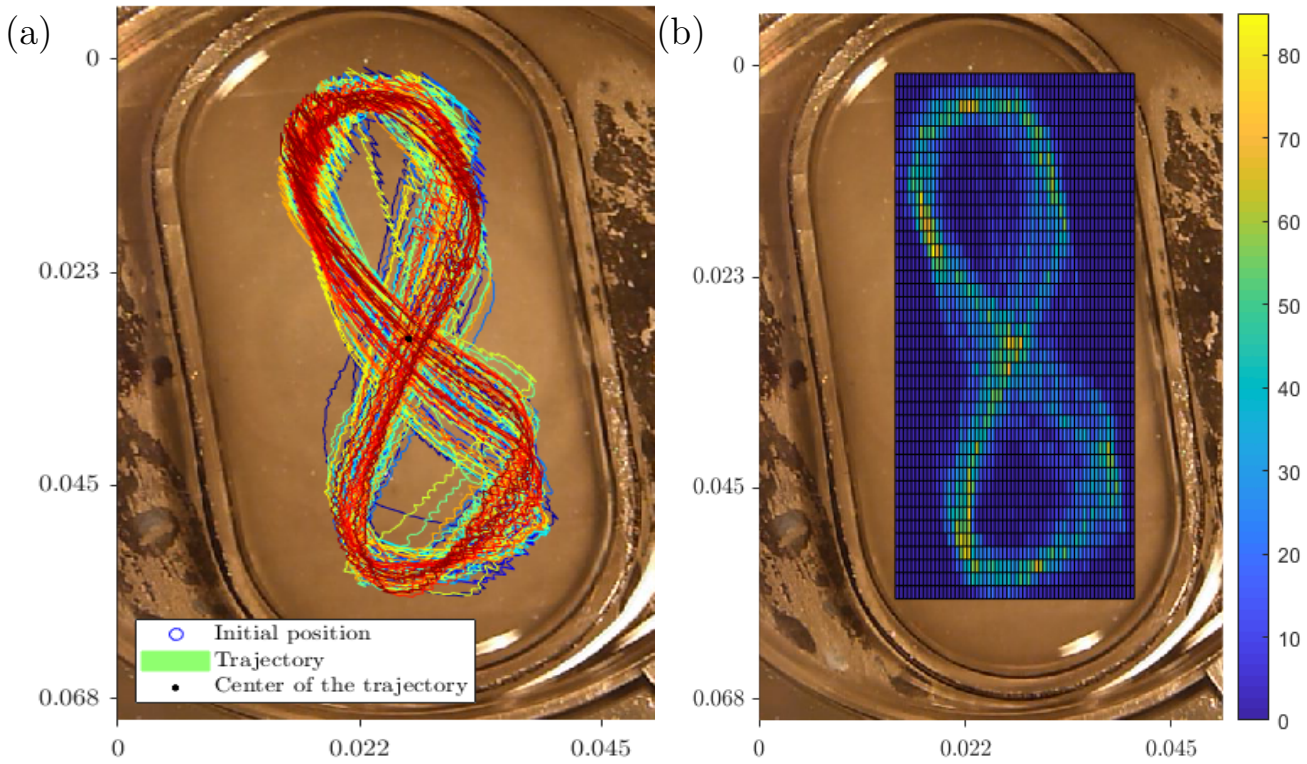

Figure 4.37: Walking droplet observations in the stadium cavity with parameters : $(f, \Gamma, D) = (80[Hz], 1920[mg], 1.05[mm])$. All the axis are expressed in [m] and the colorbar in (b) gives the number of occurrences. (a) Obtained trajectory. The colors along the trajectory evolve gradually from the starting point to the ending one. (b) 2D empirical density corresponding to (a).

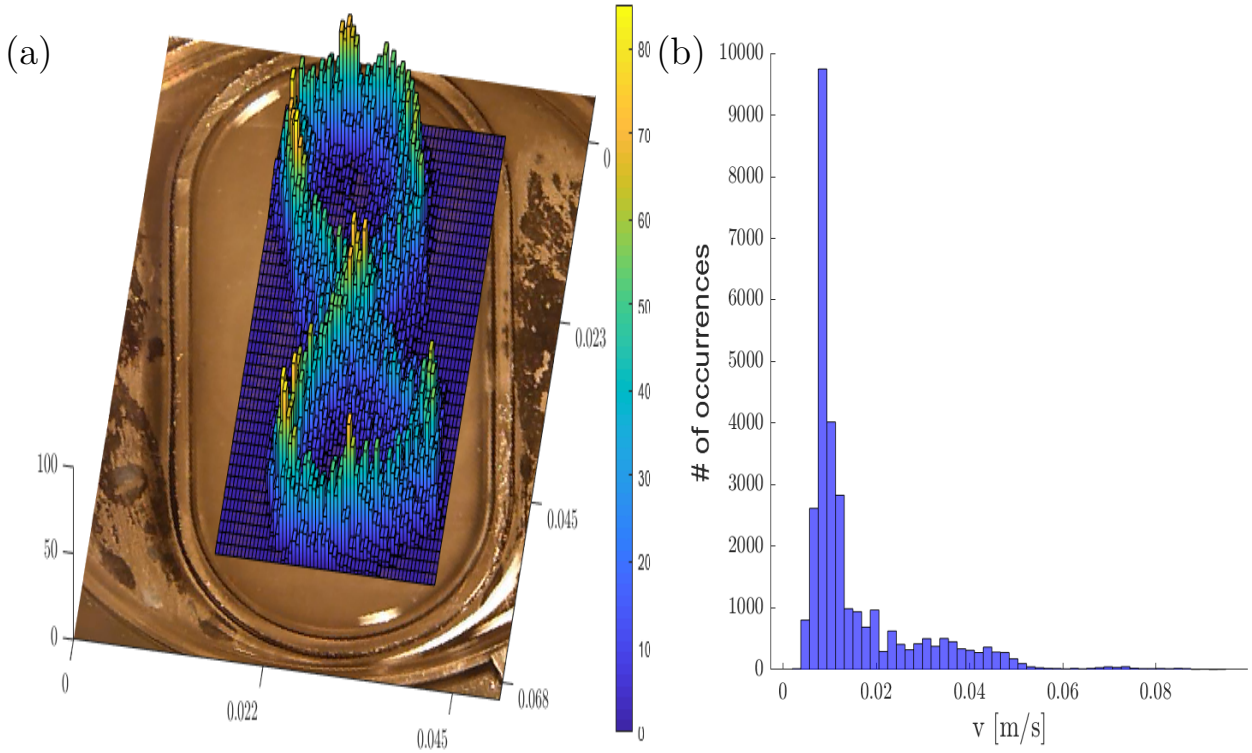

Figure 4.38: Walking droplet observations in the stadium cavity with parameters : $(f, \Gamma, D) = (80[Hz], 1920[mg], 1.05[mm])$. (a) Isometric view of the 2D histogram from Figure 4.37(b). (b) Histogram of the walker's speed.

The global observation made with a walking droplet inside the stadium cavity is represented in Figure 4.37. We clearly see that a pattern shows up, having an ∞-like shape. An isometric view of the 2D histogram from Figure 4.37(b) is also shown in Figure 4.38(a). An histogram of the measured droplet's velocity is shown in Figure 4.38(b), we observe a very large peak corresponding to the free walking speed between the reflections on the cavity borders, while the deviations from this peak correspond to the reflections on the borders of the cavity combined some noise in the measurements related to the results described with Figure 4.33.

Figure 4.37(b) gives the empirical pdf, representative of the probability of finding the walking droplet at any location in the stadium. As shown in the left column from Figure 4.40, this pattern is very robust, in the low memory regime, against forcing frequency variations (f_0 has been varied in the $[70-85][Hz]$ range) and thus to variations in the resulting length ratios (λ_F/R_b has thus been varied in the $[0.279-0.24]$ range, useful for the comparison as written in eq. (5.6)). In the right column though, we can see that the pattern tends to disappear as the memory parameter Me increases. Figure 4.40(e) is not relevant for the analysis of the pattern but is shown to highlight the fact that imperfect horizontality of the bath (as discussed in Section 4.2) influences the behaviour of the droplet. As for very low memory regimes, the droplet's velocity is low, it tends to be reflected far from the borders and this highlights a preferred side in the stadium cavity due to the slight tilt of the bath.

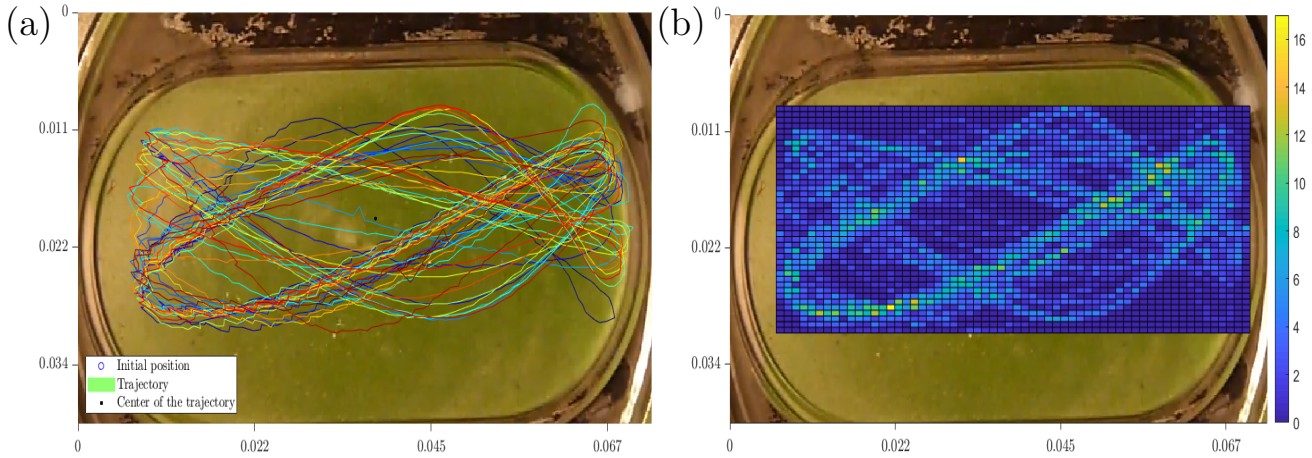

Figure 4.39: Walking droplet observations in the stadium cavity with parameters : $(f, \Gamma, D) = (80[Hz], 2200[mg], 0.95[mm])$. (a) Trajectory. (b) Empirical 2D pdf.

Another experiment has been conducted near the effective Faraday instability threshold $\Gamma \lessapprox \Gamma_F = 2300[mg]$. We can observe in Figure 4.39(a) that the high memory regime induces loopy reflections on the right side border, as observed in ref. [61]. In this case, the ∞-like shape has disappeared to yield another stationary pattern. The reproducibility of other patterns than the one from Figure 4.37 in the high memory regime should be tested with more reliable experimental setups.

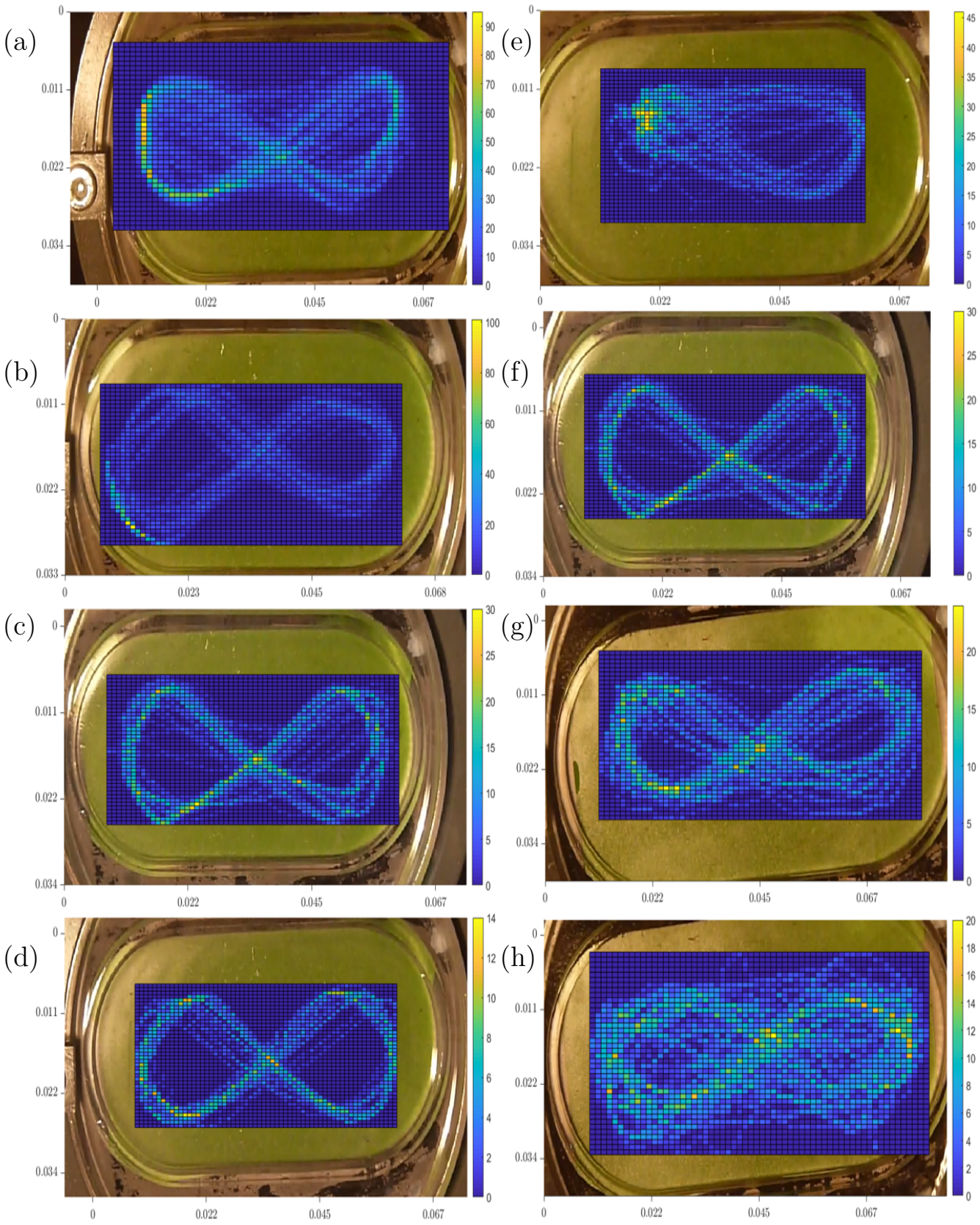

Figure 4.40: Robustness of the ∞-like shaped pattern against forcing variations. All the axes are expressed in $[m]$. In all cases, the droplet diameter $D \in [0.75 - 0.85][mm]$. Left column : variation of the frequency f_0 in the range of walking possibilities given in Figure 3.6. (a) $f_0 = 70[Hz]$, (b) $f_0 = 75[Hz]$, (c) $f_0 = 80[Hz]$, (d) $f_0 = 85[Hz]$. Right column : variation of the shaking amplitude Γ with $f_0 = 80[Hz]$. (e) $\Gamma = 1650[mg]$, (f) $\Gamma = 1900[mg]$ (g) $\Gamma = 2090[mg]$ (h) $\Gamma = 2200[mg]$.

Chapter 5

Electronic transport analysis

Quantum billiards (or cavities) are mesoscopic billiards. Electrons shoot over this "table" with velocities bigger than $10^5[m/s]$, colliding elastically with the walls until they disappear into one of the pockets (a.k.a. *leads*). The motion of an electron in a typical metal wire is very different from the rectilinear motion of a billiard ball. The impurities in the metal scatter the electrons in all directions, so that the motion becomes completely unpredictable. One speaks of a "random walk". A measure for the influence of impurities on the electron motion is the so called "mean free path" L_μ which gives the typical distance an electron can move before colliding with an impurity. Therefore, the analysis of electrons behaviour inside quantum billiards has been possible by obtaining a mean free path much greater than the size of the billiard. The electronic industry has become very skilled at fabricating semiconducting materials with a large mean free path. The world record is around $100[\mu m]$. To eliminate the impurities a technique is used called "molecular beam epitaxy". [87] A crystal is grown one atomic layer at the time, until a nearly perfect lattice of atoms is obtained. Because the process is controlled on the atomic scale, it is possible to vary the composition of the individual atomic layers in the crystal. This is used to fabricate a billiard table for electrons which is not only very smooth (i.e. with a large mean free path), but also perfectly flat. From such materials, the so-called heterostructures, one can then carve out extremely small geometries such as quantum dots, or billiards, using lithography techniques combined with metal deposition or etching.

Focusing our discussion on the stadium billiard, the existence of quantum scars (introduced in Section 2.2) had been theoretically predicted [29] before being experimentally observed by C. Marcus and his associates in 1992 [46]. The experimental observations have then been followed by numerical simulations conducted by Akis, Ferry and Bird [4, 5] as shown in Figure 5.1. Both in the experimental and numerical observations, it is shown that the low field magnetoconductance G of stadium shaped quantum dots can be periodic, indicating that only a few regular orbits dominate the quantum transport, even though the structure is classically chaotic (as discussed in Section 2.1). The important role played by the contacts, which essentially select certain eigenstates to dominate the transport, is pointed out in ref. [4]. They also show that transport in open quantum dots can be mediated by single robust eigenstates (generally localized within the interior of the dot), even when the dot leads support several propagating modes.

It has to be pointed out that the quantum scars can always be associated to an analog classical periodic orbit. These scars are also shown to exist in relativistic systems. Indeed, using graphene as a paradigm, ref. [26] have discovered relativistic quantum scars for both closed and open systems, as depicted in Figure 5.2.

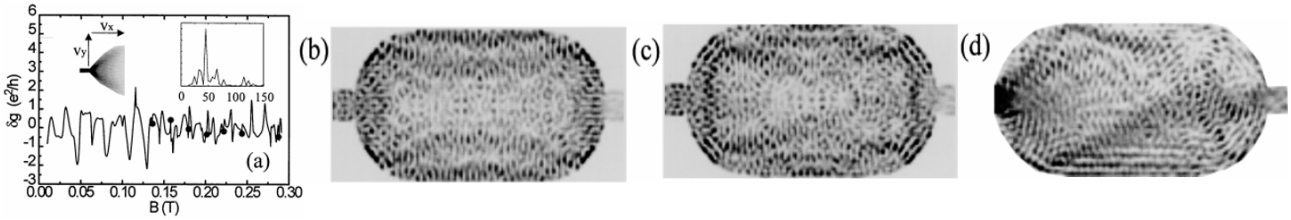

Figure 5.1: Simulations from ref. [5]. (a) Conductance fluctuations (δg) as a function of magnetic field B. The right inset shows the corresponding power spectrum and the left inset the collimated beams emerging from a Quantum Point Contact. ($|\psi(x,y)|^2$) versus x and y is plotted for (b) $B = 0.135[T]$ and (c) $B = 0.288[T]$, showing a rectangular scar in both cases. (d) also corresponds to $B = 0.288[T]$, but now phase breaking is introduced to isolate the effects of the input lead.

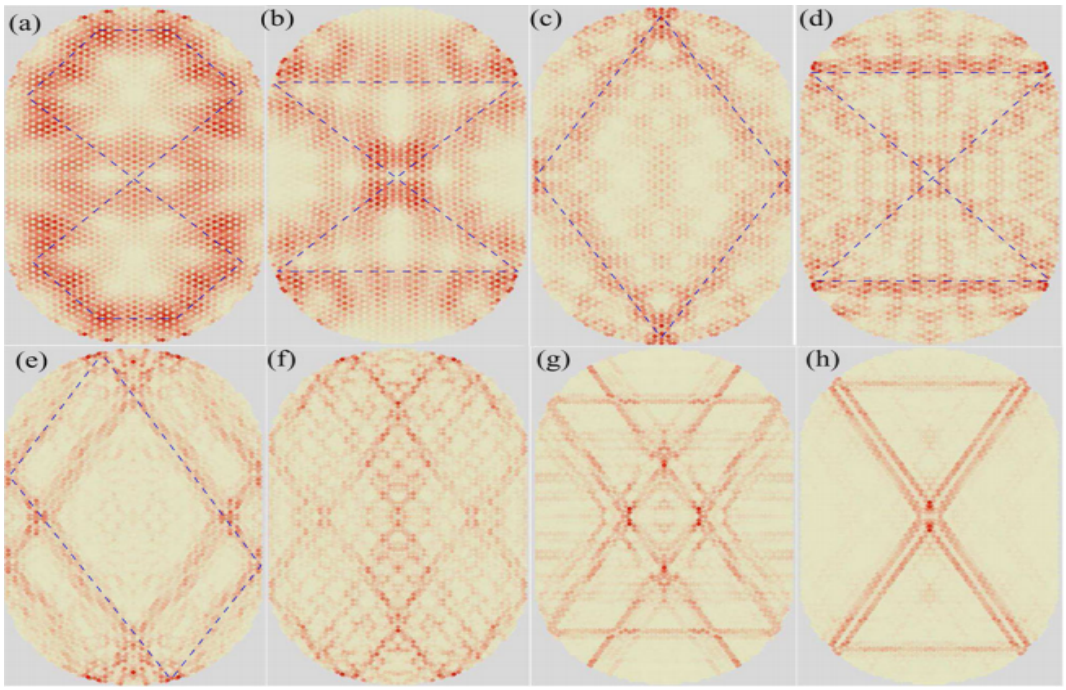

Figure 5.2: Typical scars in a stadium-shaped graphene confinement. The energy values for (a–h) are $E/t = 0.25347, 0.36358, 0.57665, 0.60699, 0.81956, 0.91061, 0.97722$, and 0.99198, respectively. The dashed lines represent classical periodic orbits associated to these scars. Taken from ref. [26].

5.1 Quantum simulations

Name	Expression	Value [Unit]
Planck's constant	h	6.626069e-34 [J.s]
Electric charge of the electron	e	$1.602 \cdot 10^{-19}[C]$
Light celerity	c	299792458 [m/s]
Boltzmann constant	k_B	$1.3806503 \cdot 10^{-23}$ $[kg.m^2/Ks^2]$
Mass of the electron	m_e	$9.1 \cdot 10^{-31}$ [kg]
Hopping parameter	t	2.8 $[eV]$
Lattice parameter	a_{square}	0.25 $[nm]$
Default Fermi energy	E_f	0.87 $[eV]$
Scaling parameter	s	1 [-]
Applied potential	V_g	0 $[eV]$
Applied magnetic field	B	0 $[T]$
Width of the leads	$width\_leads$	2.8$[nm]$
Stadium semicircle radius	R_q	11.275$[nm]$
Stadium length	L	45.1$[nm]$

Table 5.1: Values used for the quantum numerical simulations

For the simulation of the electronic transport in a stadium cavity, two Python packages have been used in parallel : ***Kwant*** and ***Pybinding*** to develop the "*Stadium_Kwant.ipynb*" and "*Stadium_Pybinding.ipynb*" codes, respectively (see the *Supplementary materials* [35]). Both are used for numerical tight-binding [86] calculations in solid state physics. Concretely, they resolve the single electron time independent Schrödinger's equation in an arbitrary chosen geometry (see Appendix B). The default values used for the simulations are given in Table 5.1.
In practice, the confinement of electrons in a 2D space is performed by the use of heterostructures, leading to a 2 dimensional electron gas (2DEG) [87]. In the simulations, we will directly consider a 2D system. The usual material allowing to confine the electrons in a 2DEG is the heterostructure $Al_xGa_{1-x}As$. As described in Appendix B, the real lattice is approximated by a simpler lattice in the simulations, in this case a square lattice, as shown in Figure 5.3.

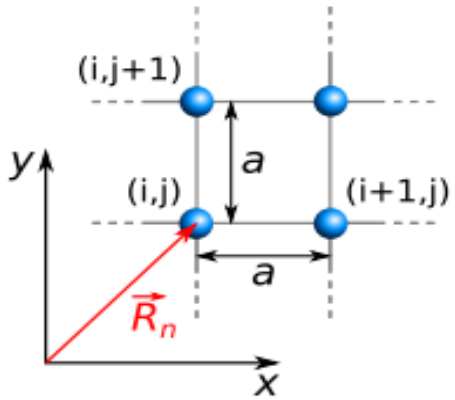

Figure 5.3: Schematic of a square lattice where the atoms are represented by blue balls. The lattice parameter is a and each atom position is given by a vector $\mathbf{R}_n$ where n is the atom label running over the couples (i, j). Taken from [52].

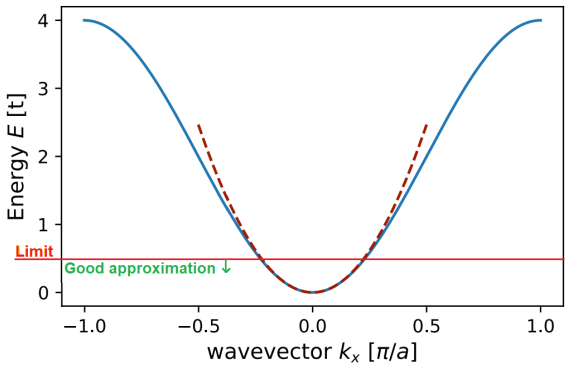

Figure 5.4: The energy dispersion (band structure) of eq. (5.1) is depicted in blue as a function of k_x for $k_y = 0$ and $E_0 = 4t$. A Taylor series development of this curve for small energies is depicted with the red dashed line. Adapted from [52].

Following reference [52], as we consider only the neighbouring atoms for the *hopping* energy

(the energy gained by an electron two be able to go from one atom to another), the *energy dispersion* can be expressed as :

$$E = E_0 - 2t\left(\cos(k_x a) + \cos(k_y a)\right) \tag{5.1}$$

As we consider a single electron transport in this application, the energy range available for the electron is small, resulting in a low Fermi energy. By looking eq. (5.1), it implies $k = (k_x, k_y) \sim 0$. The energy (by always considering $E_0 = 4t$) can then be expressed with the second order Taylor series as :

$$E = t\left[(k_x a)^2 + (k_y a)^2\right] = ta^2k^2 \tag{5.2}$$

Where $k^2 = k_x^2 + k_y^2$. The approximation in eq. (5.2) is considered valid as long as the condition $E_f < 0.5t$ is verified (this condition is thus checked in the codes [35]). This expression, represented in Figure 5.4, is actually the kinetic energy for a free particle described by the simple equation :

$$\frac{-\hbar^2}{2m}\nabla^2\psi(\mathbf{r}) = E\psi(\mathbf{r}) \tag{5.3}$$

There is no potential term in this Hamiltonian. The solutions for the energy and the wave are :

$$\psi(\mathbf{r}) = \exp(i\mathbf{k}\cdot\mathbf{r}) \qquad E = \frac{\hbar^2k^2}{2m} \tag{5.4}$$

By comparing eq. (5.2) and eq. (5.4), we can determine the effective mass m of the electrons of our square lattice as a function of the lattice and hopping parameters a and t :

$$m = \frac{\hbar^2}{2a^2t} \tag{5.5}$$

The conclusion is that electrons behave as free particles but their mass is modified by the presence of the periodic lattice.

To make the quantum simulations comparable to the experimental results obtained with walking droplets in Section 4.3, we impose the same ratio between the wavelength and the stadium semicircle radius, i.e. :

$$\frac{\lambda}{R_q} = \frac{\lambda_F}{R_b} \tag{5.6}$$

Where R_q and R_b denote the stadium semicircle radii in the quantum simulations and in the experiments ("b" stands for "bath"). The Fermi wavelength λ is related to the energy E as :

$$E = \frac{\hbar^2k^2}{2m} = \frac{\left(\frac{h}{2\pi}\right)^2\left(\frac{2\pi}{\lambda}\right)^2}{2m} = \frac{h^2}{2m\lambda^2} \tag{5.7}$$

The condition on the ratio λ/R_q from eq. (5.6) is fulfilled in "*Stadium_Kwant.ipynb*" and "*Stadium_Pybinding.ipynb*" by imposing the Fermi energy $E = E_f < 0.5t$, computing the resulting Fermi wavelength λ from eq. (5.7) and choosing the cavity dimensions (hence R_q) consequently.

5.2 Results and discussion

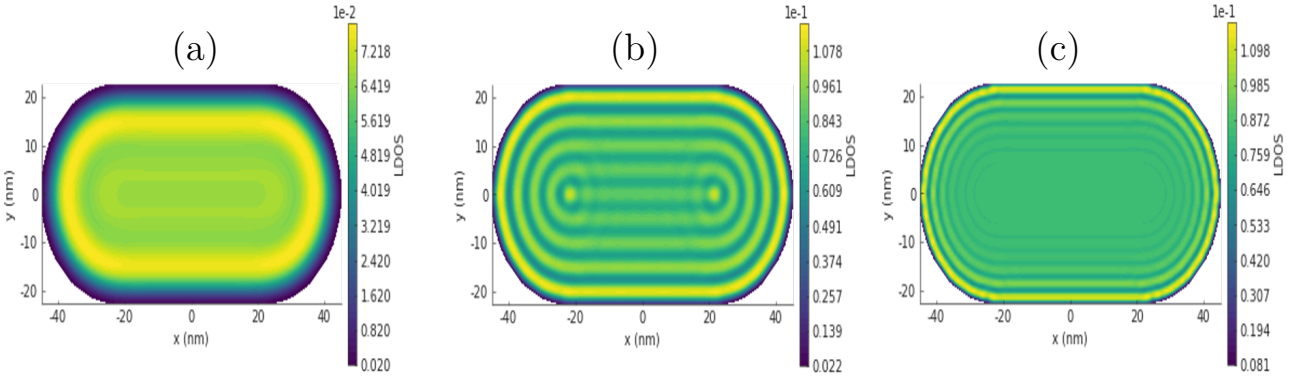

Figure 5.5: Local density of states obtained with "*Stadium_Pybinding.ipynb*". (a) $\lambda/R_q = 1.387$ (b) $\lambda/R_q = 0.44$ (c) $\lambda/R_q = 0.25$.

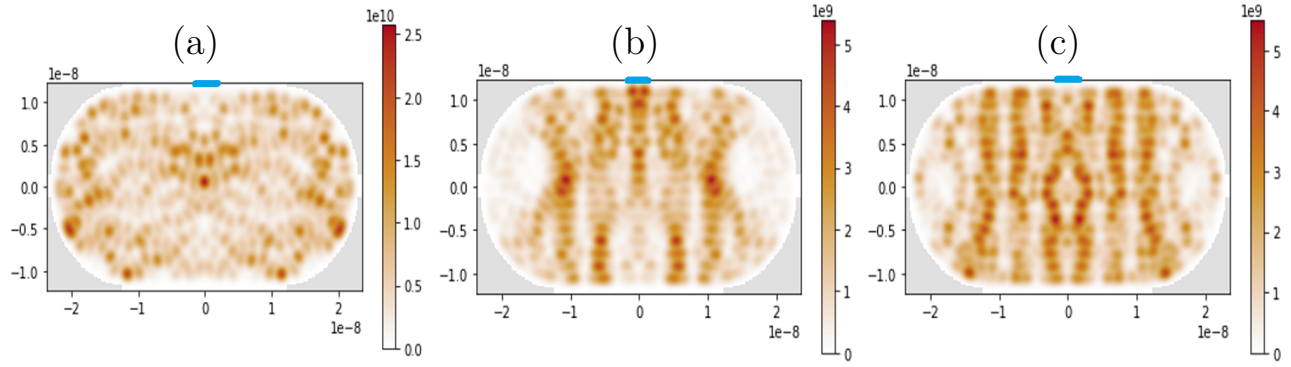

Figure 5.6: pdf obtained with "*Stadium_Kwant.ipynb*". The axes are expressed in $[m]$. (a) $\lambda/R_q = 0.254$ (b) $\lambda/R_q = 0.25$ (c) $\lambda/R_q = 0.2463$. The only lead is highlighted in blue.

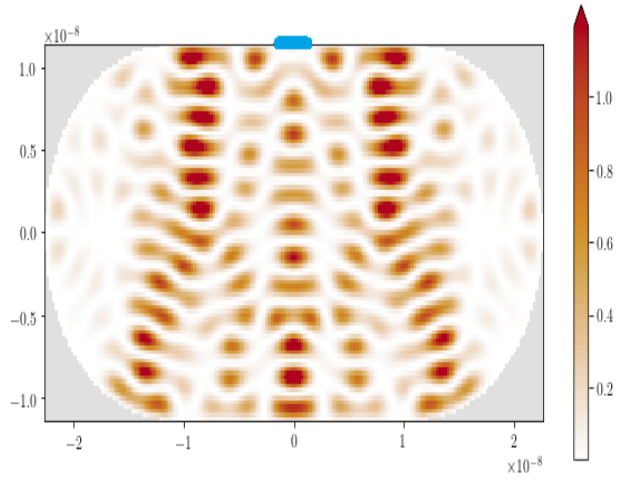

Figure 5.7: Pdf pattern chosen for the recurrence curve in Figure 5.8 with $E_f/t = 0.2$. The axes are expressed in $[m]$. The only lead is highlighted in blue.

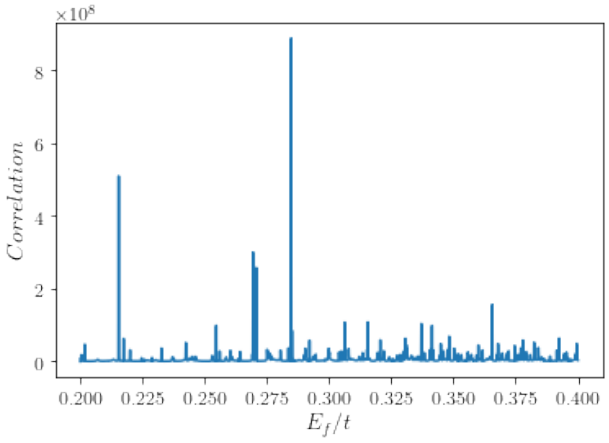

Figure 5.8: Recurrence pattern obtained by correlating the simulated scar pdf at different Fermi energies E_F with the pattern from Figure 5.7.

Figure 5.5 displays the Local Density Of States maps for stadium cavities with three consecutive λ/R_q ratios, computed with *Pybinding*. The LDOS at position $\mathbf{r} = [x, y]^T$ inside the billiard writes as :

$$LDOS(\mathbf{r}) = \frac{1}{\sigma\sqrt{2\pi}} \sum_{n=1}^{N} |\Psi_n(\mathbf{r})|^2 \exp\left(-\frac{1}{2}\left(\frac{E_n - E}{\sigma}\right)^2\right) \tag{5.8}$$

Where $\sigma = 0.01$ is the broadening, $|\Psi_n(\mathbf{r})|^2$ is the probability of presence of the electron at position $\mathbf{r}$ and E_n denotes the n-th discrete energy level. The plot in Figure 5.6 is given with $N = 1000$.
One observes a regular and symmetric steady state LDOS, where the Fermi wavelength λ clearly decreases wrt the dimensions of the billiard from (a) to (c). What can be deduced from the results displayed in Figure 5.5 is that, despite it does not require leads as *Kwant*, *Pybinding* is not suitable for a comparison with the observations made with walking droplets in Section 4.3 because it can only capture cavity eigenmodes without any electron flow. Indeed, as developed in Appendix B, the framework underlying *Pybinding* the 2D time-independent Schrödinger equation, which implies that one completely looses the time-dependency which is critical in the walking droplet case. It has to be noted that Figure 5.5 displays the LDOS because its drawbacks are clearer than with the pdf maps (as done with *Kwant* and explained below) but the conclusions remain identical in both cases. From this observation, *Pybinding* has been dropped out.

On the other hand, Figure 5.6 displays the pdf maps for stadium cavities with three very close λ/R_q ratios, computed with *Kwant*, i.e. it displays a contour plot of $|\Psi_n(\mathbf{r})|^2$ at each position $\mathbf{r}$. *Kwant* is especially suited for electronic transport simulation and requires the presence of leads (source of electrons arriving in the cavity) for this purpose. The width of the lead is important as it influences the wavefunction modes (i.e. the different wavelengths) that will be considered in the cavity. [4] Aware of this fact, the width of the leads is chosen to match the Fermi wavelength λ such that no other multiple of λ are able to interfere (see Table 5.1). As shown in Figure 5.6, the computed pdf presents scarring effects. However, compared to the walking droplet case described in Section 4.3 and as shown in Figure 5.8, the scarring pattern in the stadium cavity is highly sensitive to the ratio λ/R_q, or equivalently to the energy E_f (this is precisely a hallmark of chaotic behaviour). This sensitivity is also accompanied by a recurrence curve in Figure 5.8, where the similarity (in the 2D cross-correlation sense) with the arbitrarily chosen pdf scarring pattern from Figure 5.7 exhibits many peaks at specific fermi energy values E_f (as also demonstrated in ref. [8]).

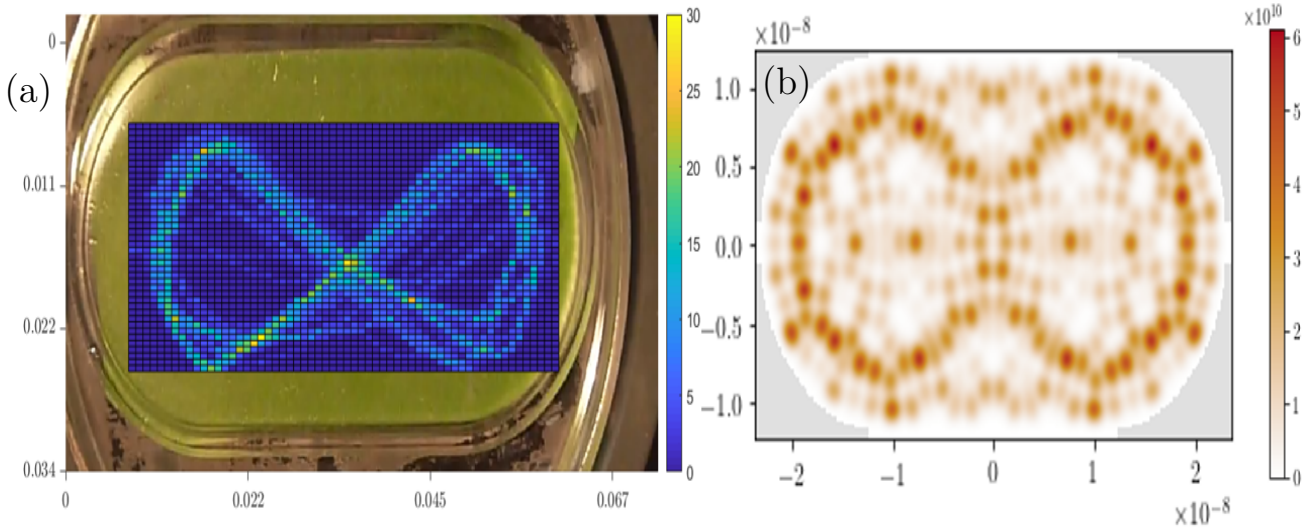

Figure 5.9: Similarity in two $\infty - like$ shapes. (a) Experimental observation with the walking droplet. (b) Electron transport simulation with *Kwant*.

A direct comparison between the walking droplet and the electron behaviours in the stadium cavity is given in Figure 5.9. Pooling the results obtained in 4.3 with the walking droplet and the ones obtained by simulation in this section, the walking droplet cannot behave as a classical particle inside a stadium with dimensions comparable to the Faraday wavelength ($R_q = 4\lambda_F$), the droplet is always influenced by the billiard borders through its coupling to its pilot-wave in the walking regime. Moreover, the observations seem to show similarities between the quantum scars appearing in electron transport experiments and the walking droplet long-term behaviour. In both cases, the uniform probability distribution for a classical particle is lost to yield structured patterns of higher probability of presence, or *scars*. The clear difference in robustness between the scarring patterns with walking droplets and electrons is thought to be related to the difference between the quantum speed $v_q = \hbar k/m_e \approx 2.6 \cdot 10^5 [m/s]$ and the walking droplet maximum ballistic speed [24] $v_{max} = b\sqrt{\frac{\pi}{2}}\lambda_F f \frac{N_c}{2} \approx 6[m/s]$. Indeed, the number of bounces of the electron on the borders of the billiard (in a semiclassical view point) scales as $v_q/(4R_q) \approx 6 \cdot 10^{12}[s^{-1}]$ while it is $v_{max}/(4R_b) \approx 75[s^{-1}]$ for the walking droplet. Comparing (i.e. multiplying) the latter by the Schrödinger timescale $\frac{4\pi m}{\hbar k^2}$ and the Faraday period T_F gives 1237.8 and 1.875, respectively. It thus seems from the previous quantitative analysis that the probability of presence of the electron inside the stadium cavity is significantly more sensitive to imperfections and small variations than the probability of presence of the walking droplet inside the stadium bath.

Even if the two shapes look similar, it seems inappropriate in this case to interpret the pdf simulated with *Kwant* as being related to a continuous displacement of the electron along this trajectory, contrary to the walking droplet case. However, the focus is made on the interpretability of the measured pdf. In the walking droplet case, one has a pilot-wave system where the particle is coupled to its guiding wave, and this time-dependent coupling leads to another, probabilistic and stationary, wave which represents the chances to find the particle in a given position of the stadium cavity when trying to measure its position at a given time instant. This interpretation is non refutable for the electron transport case and is directly related to the *De Broglie* theory briefly presented in Chapter 1.

Chapter 6

Conclusion and perspectives

This work constitutes the first experimental setup on walking droplets developed at *UCLouvain*. All the key features have been covered, from the actuation control to the measurement tools. Some improvements can still be brought to this setup which could lift hurdles for further experimental investigations, and they are described in Section 6.2.

6.1 Discussion on the obtained results

Let us first remind the central question of this master thesis :

"*How does the behaviour of a walking droplet (a.k.a.* walker*) compare to the classical and quantum particles' behaviours inside a Bunimovich stadium cavity?*".

From the observations given in Sections 4.3 and 5.2, the walking droplet long-term behaviour seems to show strong similarities with some specific quantum scars appearing in electron transport experiments. In both cases, the uniform probability distribution for a classical particle is lost, and one rather observes structured patterns of higher probability of presence, or *scars*. The scars have been obtained in the quantum numerical simulations with the *Kwant* package only. Importantly the comparison with the walking droplet experiments is not fully valid due to the necessary presence of leads in the case of *Kwant* simulations.

The main result of this master thesis is a striking difference in sensitivity between the scarring pattern of the walking droplet experiment and the scarring pattern of electron's pdf. It appears that the walking droplet ∞-like shaped scarring pattern introduced in Section 4.3 is robust against forcing frequency and amplitude variations, which is not the case at all for electrons in the quantum numerical simulations. This sensitivity in the quantum case is thought to be related to the difference in speed between the quantum speed $\hbar k/m$ and the walking droplet speed, as discussed at the end of Section 5.2.

We also notice that the walking droplet does not behave as a "classical particle" inside a stadium with dimensions comparable to the Faraday wavelength ($R_q = 4\lambda_F$) in the sense that it does not exhibit the same kind of chaotic dynamics, leading to a uniform probability distribution. This behaviour may stem from the fact that the droplet is always influenced by the billiard borders through its coupling to its pilot-wave in the walking regime. However we emphasize that we only focused our experiments on a relatively small cavity size, and the behaviour in a stadium billiard of larger dimensions could be investigated to confirm that the walking droplet never behaves as a classical particle in such geometry.

We nevertheless inform that these results have been obtained with an experimental setup which is not optimal, the latter should thus be treated cautiously and may preferably be confirmed by another laboratory.

6.2 Experimental setup improvement

As this setup is the first version and the objective was to cover all the aspects of the walking droplet experiment instead of optimizing all the components, there remains some improvements that can be brought.

First, as this is the reason why the memory parameter Me cannot be rightly measured or controlled, it seems crucial to enhance to horizontality of the bath. For this purpose, we suggest the use of millimetric screws to accurately adjust the tilting of the bath. Also, the uniaxial vibration could be improved by following the suggestions given in ref. [45], i.e. mount the assembly on a levelling platform, accompanied by heavy blocks to further attenuate the vibration of the support structure and mount the vibrating bath on an optical table in order to isolate the table and carriage from any floor vibrations.

Secondly, as explained in Section 4.1.1, there is a delay of around 4 seconds between the actuation and the corresponding acceleration measurement with the current Labview code "*MyDAQ_memory_control.vi*". Removing this delay would allow to use a PI regulator so as to impose a desired memory parameter Me with a stabilized bath.

Regarding the visualization tools, in addition to the developed Schlieren method described in Section 4.1.3, it would be preferable to develop another method of quantitative liquid surface mapping to allow for a cross-validation of both methods. This second method could either be "laser beam deflection" (as in ref. [53]), the "Brewster angle" or "DNN" based methods (described in Section 4.1.3). We suggest however to use the "DNN" based method [72] (when the open-source code is available) as it would allow for using a more regular pattern and thus increase the droplet tracking accuracy. In top of that, the lighting shown in Figure 4.2 with two basic lamps makes it difficult to illuminate the bath uniformly. The use of light diffuser would be more convenient.

Moreover, let us remind that the current setup configuration does not allow for analyzing the vertical dynamics of the walking droplet. Indeed, as depicted in Figure 4.1, the bath is inserted in an opaque structure attached to the membrane of the loudspeaker, that prevents observation of the droplet vertical motion from the side. The solution would be to replace this structure by another one, with the same shape but made of a transparent material (e.g. plexiglass), also slightly higher to exceed the loudspeaker's contour.

Finally, the used launching pad contains imperfections and could be replaced by a 3D printed version accompanied by a reservoir located under it in order to collect the flowed oil.

6.3 Perspectives for future research

This work opens many perspectives for further investigation in the comparison between the quantum world and the walking droplet pilot-wave system. Regarding the experimental side, a fairer comparison with the presented quantum numerical simulations would be to consider a new stadium billiard, opened at one or multiple locations by the presence of leads. The addition of these leads would allow to study an analog of conductance with walking droplets, where the difference of potential between the input lead and output lead would be obtained by a difference of liquid depth between the two and the flow would be associated to the time spent inside the billiard. This experiment would allow to look for an eventual periodic dependence of the transmission on the difference of potential, analog to recurrence observed in electron transmission vs electron energy. One could also imagine to add the analog of magnetic field by making the whole system turn around the vertical axis, and observe if the walking droplet trajectories become curved, until presenting a behaviour similar to the Quantum Hall Effect [83] where, in the quantum case, the particles tend to follow the borders of the billiard.

The question of whether the walking droplet could behave as a classical particle inside a large enough billiard could also be investigated by performing various measurements about the reflections of droplets on walls of different shapes and sizes. If the dependence of the reflections on the walls is found to be important, it would mean that the walking droplet cannot bounce elastically as a classical particle except for some counterexamples as a flat symmetric wall. The influence of the forcing parameters (f_0, Γ) on the walking droplet behaviour inside a stadium billiard may also be further investigated, especially in the high-memory regime, unreachable with the used setup in its current configuration.

Next, it would have been interesting to take into account the time dependence in the quantum numerical simulations. Indeed, as the time needed for the droplet to converge to its permanent scarring trajectory is measurable, it should be possible to compare it with the convergence of the wavefunction by solving the time-dependent Schrödinger equation inside the stadium billiard.

About the mathematical models of the walking droplet pilot-wave system proposed in the literature, as discussed at the end of Section 3.1, none of them is currently able to handle eventual reflections of the liquid surface waves at interfaces (e.g. the borders of the stadium cavity). It implies that all the current models assume an infinitely wide system for the wave dynamics, hence cannot provide reliable prediction for the evolution of the walking droplet inside a small system as the stadium billiard. This absence in the current models is mainly due to the lack of experimental studies of wave reflections at interfaces and the increased computing complexity induced by taking account the contribution of reflected waves. According to Loïc Tadrist and his professional contacts (private conversation), it seems that the boundary condition for the wave dynamics at the interface is of the *Robin* type (hence a combination of *Dirichlet* and *Neumann* condition) in the non-viscous case.

Finally, an experimental verification of the developments made by Gilet in [24] with a more accurate experimental setup seems promising in the perspective of a direct correspondence between the walking droplet experiment and the quantum analog.

Appendices

Appendix A

Vertical oscillations

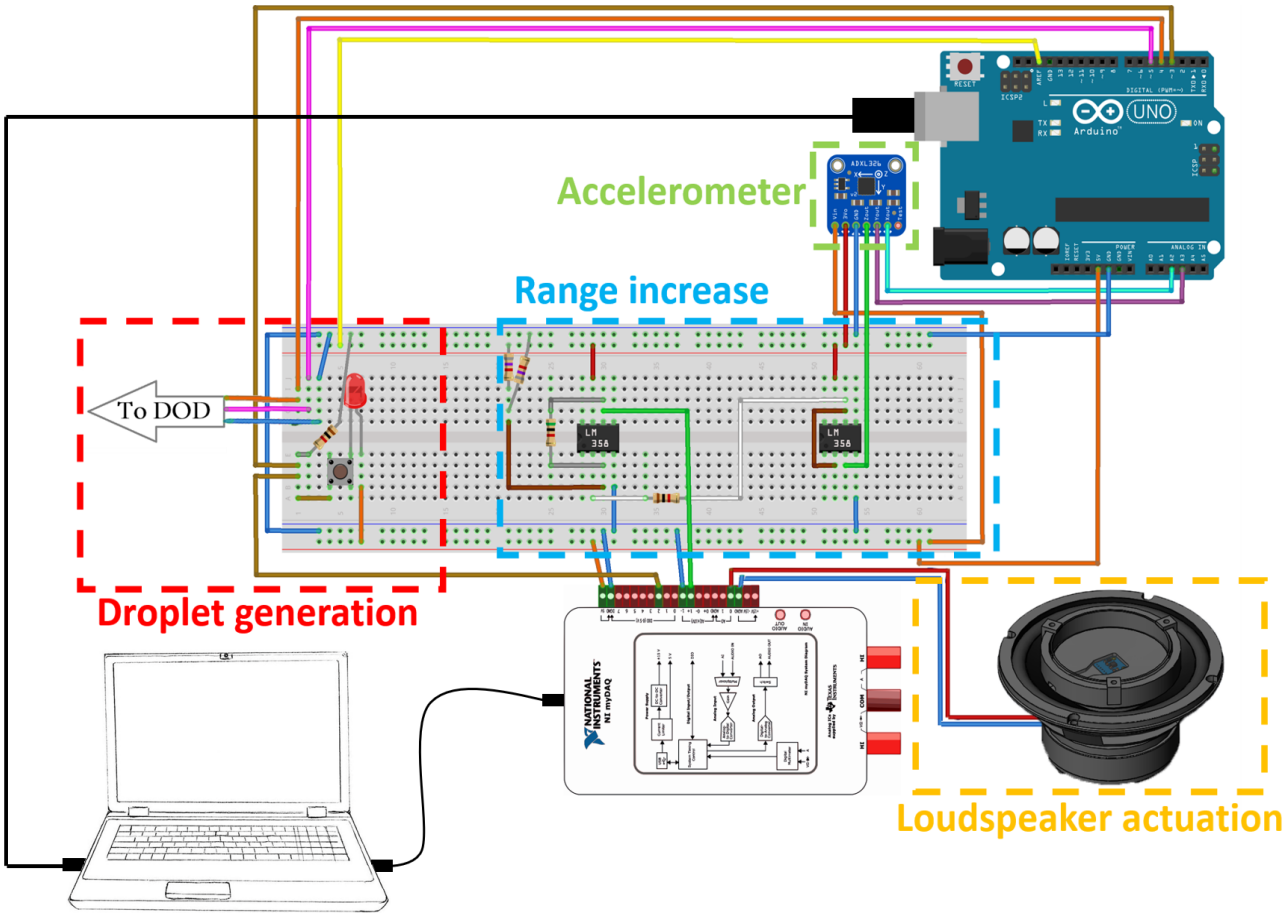

Figure A.1: Electrical connections

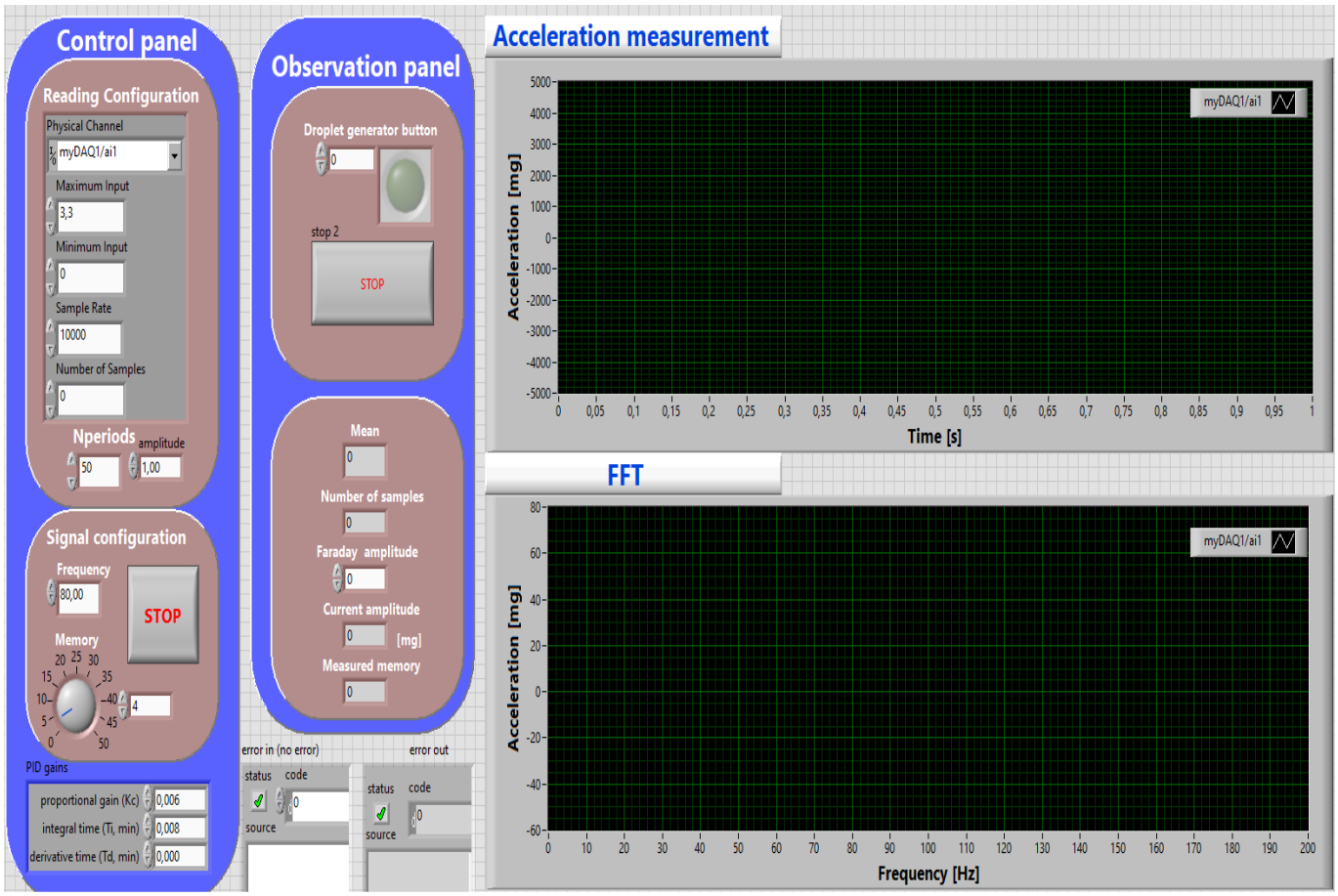

Figure A.2: Front panel of the developped Labview program.

Appendix B

Quantum simulations

The general workflow of the *Kwant* and *Pybinding* packages starts with model definition. Three main parts are required to describe a tight-binding model:

- **The crystal lattice** - The specification of the primitive lattice vectors and the configuration of the unit cell (atoms, orbitals and spins), as shown in Figure B.2.
- **System geometry** - The model system can be infinite through the use of translational symmetry or it can be finite by specifying a shape. The two approaches can also be composed to create periodic systems with intricate structural patterns. The structure can be controlled up to fine details, e.g. to form specific edge types as well as various defects.
- **Fields** - Functions can be applied to the onsite and hopping energies of the model system to simulate external fields or various effects.

Once the model description is complete, *Pybinding* or *Kwant* will build the tight-binding Hamiltonian matrix. The next step is to apply computations to the matrix to obtain the values of the desired quantum properties. Different computation methods as the *Kernel polynomial* or *Exact diagonalization* exist.

B.1 Simplification of the lattice

The first objective will be to choose a geometry for the lattice which is a trade-off between simple and close to reality. The organization of atoms in a $Al_xGa_{1-x}As$ looks like :

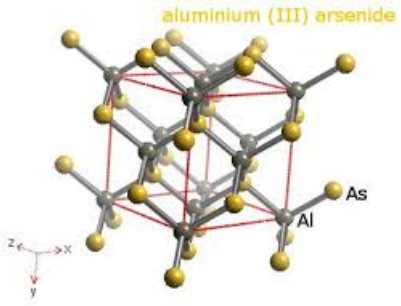

Figure B.1: Organization of the atoms in $Al_xGa_{1-x}As$. (taken from Google image)

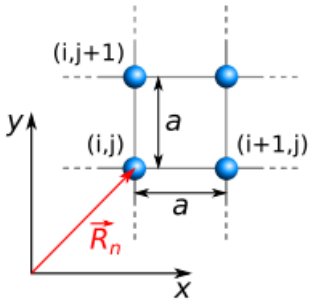

Figure B.2: Schematic of a square lattice where the atoms are represented by blue balls. The lattice parameter is a and each atom position is given by a vector $\mathcal{R}_n$ where n is the atom label running over the couples (i, j).

In order to simplify the problem in a simulation point of view, the structure in Figure B.1 in approximated by a square lattice as shown in Figure B.2 where the nuclei of each atom are considered at a fixed position.

B.2 Simplification of the Schrödinger equation

To analyze from which precise equation *Kwant* and *Pybinding* start from, let us give the general formulation of the Schrödinger equation :

$$H\psi(\vec{r}_1,\ldots,\vec{r}_n,t) = -i\hbar\frac{\partial}{\partial t}\psi(\vec{r}_1,\ldots,\vec{r}_n,t) \tag{B.1}$$

Where H is the Hamiltonian operator expressed as :

$$H = \sum_{i=1}^{n}\frac{\hbar^2}{2m_i}\Delta_{\vec{r_i}} + V(\vec{r}_1,\ldots,\vec{r}_n,t) + \underbrace{\sum_{i=1}^{n}\sum_{j>i}\frac{e^2}{4\pi\epsilon_0 r_{ij}}}_{\text{Electronic repulsion}} \tag{B.2}$$

With $\Delta_{\vec{r_i}}$ being the Laplacian operator applied in direction $\vec{r_i}$ and $V(\vec{r}_1,\ldots,\vec{r}_n,t)$ takes into account the attraction of the nuclei as well as any eventual added potential. One notices the neglecting of the mutual repulsion between electrons (see *Tight-binding approximation* below). Reducing the problem to 2D and in a cartesian frame yields :

$$H = \sum_{i=1}^{n}\frac{\hbar^2}{2m_i}\left(\frac{\partial^2}{\partial x_i^2}+\frac{\partial^2}{\partial y_i^2}\right) + V(\vec{r}_1,\ldots,\vec{r}_n,t) \tag{B.3}$$

Since the transport of electrons in a solid is studied, the nuclei of the atoms can be considered to be fixed in space. The nuclei are therefore only taken into account in the Hamiltonian to determine the potential V.

Adding the assumption that the solution should be time invariant ($\frac{\partial}{\partial t}\psi(\vec{r}_1,\ldots,\vec{r}_n,t)=0$), i.e. a stationary equilibrium is quickly established in the dynamical system, the equation simplifies to :

$$\left(\sum_{i=1}^{n}\frac{\hbar^2}{2m_i}\left(\frac{\partial^2}{\partial x_i^2}+\frac{\partial^2}{\partial y_i^2}\right) + V(\vec{r}_1,\ldots,\vec{r}_m)\right)\Phi(\vec{r}_1,\ldots,\vec{r}_n) = E\Phi(\vec{r}_1,\ldots,\vec{r}_n) \tag{B.4}$$

Introducing now the *Tight-binding approximation* [86] which is reasonable to describe electronic transport in nanostructures, we remind its two main hypoyheses :

1. Only one kind of orbital is implicated in electron transport.
2. We neglect all the interactions between electrons. We can therefore consider each one as being alone in the periodic lattice.

From these latter, the dependence on the position of the nuclei vanishes and leads to a single electron problem depending only on its position (x,y) in the 2D space :

$$\left(\frac{\hbar^2}{2m^*}\left(\frac{\partial^2}{\partial x^2}+\frac{\partial^2}{\partial y^2}\right) + V(x,y)\right)\Phi(x,y) = E\Phi(x,y) \tag{B.5}$$

On which some supplementary simplifications as the *Linear combination of atomic orbitals* and *on-site and hopping parameters* are described in [86]. The remaining equation will finally be discretized in the two space dimensions (x,y) in order to be numerically solved.

Bibliography

[1] Determination of viscosity with the falling ball viscometer according to höppler. https://www.ld-didactic.de/documents/en-US/EXP/C/C3/C3121_e.pdf. [Online; accessed 3-June-2020].

[2] C. A. Galeano-Rios, A. Nachbin, J. W. M. Bush, and P. A. Milewski. *"Faraday pilot-wave dynamics: modelling and computation.". J. Fluid Mech. (2015), vol. 778, pp. 361-388.*

[3] Adafruit. Adxl326 5v 3-axis accelerometer. https://www.analog.com/media/en/technical-documentation/data-sheets/ADXL326.pdf. [Online; accessed 9-May-2020].

[4] R. Akis, D. K. Ferry, and J. P. Bird. *"The persistence of eigenstates in open quantum dots.". Appl. Phys. Lett. 81, 129 (2002).*

[5] R. Akis, D. K. Ferry, and J. P. Bird. *"Wave Function Scarring Effects in Open Stadium Shaped Quantum Dots.". Phys. Rev. Let., vol. 79, 123 (1997).*

[6] A. Andersen, J. Madsen, C. Reichelt, S. Rosenlund Ahl, B. Lautrup, C. Ellegaard, M. T. Levinsen, and T. Bohr. *"Double-slit experiment with single wave-driven particles and its relation to quantum mechanics.".*

.

[7] A. Bogatskiy. Periodic orbit quantization. https://www.google.com/url?sa=t&rct=j&q=&esrc=s&source=web&cd=&cad=rja&uact=8&ved=2ahUKEwjim6Om8-fpAhWJxqQKHf5RAwwQFjACegQIBBAB&url=http%3A%2F%2Ftheory.uchicago.edu%2F~ejm%2Fcourse%2FJournalClub%2Falex_gutzwiller_formula.pdf&usg=AOvVaw1FaebpAx_uwMK7WTSrXJJQ.

[8] D. Cabosart, A. Felten, N. Reckinger, A. Iordanescu, S. Toussaint, S. [U+FFFD]aniel, and B. Hackens. "Recurrent Quantum Scars in a Mesoscopic Graphene Ring.". Nano Letters 17(3), (2017).

[9] Y. Couder, E. Fort, S. Protière, A. Eddi, J. Moukhtar, E. Sultan, A. Boudaoud, C. H. Gautier, F. Moisy, and M. Rossi. A macroscopic-scale wave-particle duality.

[10] T. Cristea-Platon, P. J. Saenz, and J. W. M. Bush. "Statistical projection effects in a hydrodynamic pilot-wave system.". Nature Physics, vol. 14, pp. 315–319 (2018).

[11] T. Cristea-Platon, P. J. Saenz, and J. W. M. Bush. "Walking droplets in a circular corral : Quantisation and chaos.". Chaos 28, 096116 (2018).

[12] S. Dorbolo, D. Terwagne, N. Vandewalle, and T. Gilet. "Resonant and rolling droplet.". New Journal of Physics, vol. 10, pp. 11 (2008).

[13] S. Douady. "Experimental study of the Faraday instability.". J. Fluid Mech. , vol. 221, pp. 383409 (1990).

[14] R. Dubertrand, M. Hubert, P. Schlagheck, N. Vandewalle, T. Bastin, and J. Martin. "Scattering theory of walking droplets in the presence of obstacles.". New J. Phys. 18 113037 (2016).

[15] M. Durey and P. A. Milewski. "Faraday wave–droplet dynamics: discrete-time analysis.". J. Fluid Mech. (2017), vol. 821, pp. 296-329.

[16] A. Eddi, A. Boudaoud, and Y. Couder. "Oscillating instability in bouncing droplet crystals.". EPL (Europhysics Letters), vol. 94, Number 2 (2011).

[17] A. Eddi, A. Decelle, E. Fort, and Y. Couder. "Archimedean lattices in the bound states of wave interacting particles.". EPL (Europhysics Letters), vol. 87, Number 5 (2009).

[18] A. Eddi, E. Fort, F. Moisy, and Y. Couder. "Unpredictable Tunneling of a Classical Wave-Particle Association.". Phys. Rev. Let. (2009), 102(24):240401.

[19] A. Eddi, E. Sultan, J. Moukhtar, E. Fort, M. Rossi, and Y. Couder. "Information stored in Faraday waves: the origin of a path memory.". J. Fluid Mech. (2011), vol. 674, pp. 433–463.

[20] Farnell. Piezoelectric buzzer. https://fr.farnell.com/multicomp/mcabt-455-rc/element-audio-piezo-2-8khz-35mm/dp/2433035.

[21] B. Filoux, M. Hubert, and N. Vandewalle. "Strings of droplets propelled by coherent waves.". Phys. Rev. E. 92, 041004(R). (2018).

[22] E. Fort and Y. Couder. "Single-Particle Diffraction and Interference at a Macroscopic Scale.". Phys. Rev. Let. (2006), 97(15):154101.

[23] T. Gilet. "Dynamics and statistics of wave-particle interactions in a confined geometry.". Phys. Rev. E, vol. 90, 052917 (2014).

[24] T. Gilet. "Quantumlike statistics of deterministic wave-particle interactions in a circular cavity.". Phys. Rev. E, vol. 93, 042202 (2016).

[25] heligone. Heligone youtube channel on walkers. https://www.youtube.com/user/heligone/videos.

[26] L. Huang, Y.-C. Lai, D. K. Ferry, S. M. Goodnick, and R. Akis. "Relativistic Quantum Scars.". Phys. Rev. Let., vol. 103, 054101 (2009).

[27] M. Hubert, B. Filoux, P. Schlagheck, and N. Vandewalle. "Walking droplets in linear channels.". Phys. Rev. Fluid 2, 013601 (2017).

[28] M. Hubert, M. Labousse, and S. Perrard. "Self-propulsion and crossing statistics under random initial conditions.". Phys. Rev. E 95, 062607 (2017).

[29] E. J. Heller. "Bound-State Eigenfunctions of Classically Chaotic Hamiltonian Systems: Scars of Periodic Orbits.". Phys. Rev. Let., vol. 53, 1515 (1984).

[30] L. Jacques and C. De Vleeschouwer. Mathematical morphology and relatives. https://moodleucl.uclouvain.be/pluginfile.php/1996716/mod_folder/content/0/W05/ELEC2885_Mathematical-morphology-and-relatives.pdf?forcedownload=1.

[31] J. Jeene Castro. "Using Free Surface Synthetic Schlieren to Observe the Surface Waves of Water.". Bachelor thesis, Utrecht University (2016).

[32] L. Joannes, F. Dubois, and J.-C. Legros. "Phase-Shifting Schlieren: High-Resolution Quantitative Schlieren that Uses the Phase-Shifting Technique principle.". Applied Optics 42(25), pp. 5046-5053 (2003).

[33] C. King. "Exploring Quantum, Classical and Semiclassical Chaos in the Stadium Billiard.". Quanta (2014); 3: 16–31.

[34] M. Labousse. "Étude d'une dynamique à mémoire de chemin: une expérimentation théorique.". Université Paris-Diderot - Paris VII, (2014).

[35] O. Leblanc. Supplementary materials. https://github.com/oliviero3/Walking-droplet-in-stadium-cavity.

[36] J. Lei and X. Li. "Some dynamical properties of the stadium billiard.". Physica D: Nonlinear Phenomena, Volume 189, Issues 1–2, 15, Pages 49-60, (2004).

[37] E. Louis, J. A. Miralles, G. Chiappe, A. Baza, J. P. Adrados, and P. Cobo. "Faraday instability in a vessel with a well: A numerical analysis.". Phys. Fluids, vol. 23, 114102 (2011).

[38] J. Lundbek Hansen and P. Cvitanovic. Lyapunov exponents for the stadium billiard, 1995.

[39] L. M. Faria. "A model for Faraday pilot waves over variable topography.". J. Fluid. Mech., vol. 811, pp. 51-66 (2016).

[40] D. M Harris, T. Liu, and J. WM Bush. "A low-cost, precise piezoelectric droplet-on-demand generator". Experiments in Fluids 56(4), (2015).

[41] D. M. Harris, J. Moukhtar, E. Fort, Y. Couder, and J. W. M. Bush. "Wavelike statistics from pilot-wave dynamics in a circular corral.". Phys. Rev. E, vol. 88, 011001(R) (2013).

[42] D. M. Harris, B. P.-T., A. Damiano, L. M. Faria, and J. W. M. Bush. "Wavelike statistics from pilot-wave dynamics in a circular corral.". Chaos 28, 096105 (2018).

[43] D. M. Harris, J. Quintela, V. Prost, P.-T. Brun, and J. W. M. Bush. "Visualization of hydrodynamic pilot-wave phenomena.". Journal of Visualization 20(1) (2016).

[44] D. M. Harris and J. W. M. Bush. "Droplets walking in a rotating frame : from quantized orbits to multimodal statistics.". J. Fluid. Mech., vol. 739, pp. 444-464 (2013).

[45] D. M. Harris and J. W.M. Bush. "Generating uniaxial vibration with an electrodynamic shaker and external air bearing.". Journal of Sound and Vibration 334 (2015) 255–269.

[46] C. M. Marcus, A. Rimberg, R. M. Westervelt, P. F. Hopkins, and A. C. Gossard. "Conductance Fluctuations and Chaotic Scattering in Ballistic Microstructures.". Phys. Rev. Lett. 69, 506 (1992).

[47] H. C. Manoharan, C. P. Lutz, and D. M. Eigle. "Quantummirages formed by coherent projection of electronic structure.". Nature volume 403, pages512–515(2000).

[48] J. Molacek and J. W. M. Bush. "Drops bouncing on a vibrating bath.". J. Fluid Mech. (2013), vol.727, pp. 582-611.

[49] J. Molacek and J. W. M. Bush. "Drops walking on a vibrating bath : towards a hydrodynamic pilot-wave theory.". J. Fluid. Mech., vol. 727, pp. 612-647 (2013).

[50] R. N. Valani and A. C. Slim. "Pilot-wave dynamics of two identical, in-phase bouncing droplets.". Chaos 28, 096114 (2018).

[51] R. N. Valani, A. C. Slim, and T. Simula. "Superwalking droplets.". Phys. Rev. Let., vol. 123, 024503 (2019).

[52] Nicolas Moreau. Lelec 2710 - exercise sessions simulations using the kwant package. https://moodleucl.uclouvain.be/pluginfile.php/2027659/mod_folder/content/0/Execise_sessions_LELEC_2710.pdf?forcedownload=1, 2019. [Online; accessed 15-December-2019].

[53] A. P. Damiano, P. Brun, C. A. Galeano-Rios, D. M Harris, and J. WM Bush. "Surface topography measurements of the bouncing droplet experiment.". Exp Fluids, vol. 57, 163 (2016).

[54] A. P. Damiano, P.-T. Brun, D. M. Harris, and C. A. Galeano-Rios. "Surface topography measurements of the bouncing droplet experiment.". J. Fluid. Mech., vol. 674, pp. 433–463 (2011).

[55] B. Parry and J. Parker. Pilot wave dynamics of walking droplets; cal poly slo physics. https://www.youtube.com/watch?v=JUI_DtzXdw4.

[56] S. Perrard. "Une mémoire ondulatoire : Etats propres, Chaos et Probabilités.". Université Paris-Diderot - Paris VII, (2014).

[57] S. Perrard, M. Labousse, E. Fort, and Y. Couder. "Chaos Driven by Interfering Memory.". Phys. Rev. E. (2014), vol. 113, 104101.

[58] M. Phillips. "The Dynamics of the Upper Ocean.". Phys. Rev. Let., vol. 261, pp.37 (1977).

[59] S. Protiere. "Gouttes rebondissantes : une association onde-particule à échelle macroscopique.". Université Paris-Diderot - Paris VII, (2007).

[60] S. Protière, A. Boudaoud, and Y. Couder. "Particle–wave association on a fluid interface.". J. Fluid Mech. (2006), vol. 554, pp. 85–108.

[61] G. Pucci, P. J. Saenz, L. M. Faria, and J. W. M. Bush. "Non-specular reflection of walking droplets.". J. Fluid. Mech., vol. 804 (2016).

[62] G. Pucci, D. M. Harris, L. M. Faria, and J. W. M. Bush. "Walking droplets interacting with single and double slits.". J. Fluid. Mech., vol. 835, pp. 1136-1156 (2017).

[63] C. A. G. Rios. "Hydrodynamic Pilot-waves: Analytical modeling approaches to the interaction of drops and surface waves.". Doctoral thesis, IMPA, (2016).

[64] B. Scheid, O. Kabov, C. Minetti, P. Colinet, and J.-C. Legros. "Measurement of free surface deformation by reflectance-Schlieren method.". 3rd European Thermal Sciences Conference (2000) .

[65] Sigma-aldrich. Silicon oil. https://www.sigmaaldrich.com/catalog/product/aldrich/378348?lang=fr&region=BE. [Online; accessed 26-April-2020].

[66] A. Simonini, P. Colinet, and M. Rosaria Vetrano. "Reference Image Topography technique applied to harmonic sloshing.". 11th International Symposium on PIV.

[67] L. Tadrist, N. Sampara, P. Schlagheck, and T. Gilet. "Interaction of two walkers: Perturbed vertical dynamics as a source of chaos.". Chaos 28, 096113 (2018).

[68] L. Tadrist, J.-B. Shim, T. Gilet, and P. Schlaghec. "Faraday instability and subthreshold Faraday waves: surface waves emitted by walkers.". J. Fluid Mech. (2018), vol. 848, pp. 906-945.

[69] G. Tanner. "How chaotic is the stadium billiard? A semiclassical analysis.". J. Phys. A: Math. Gen. 30 (1997) 2863–2888.

[70] T. Tao. Open question: scarring for the bunimovich stadium. https://terrytao.wordpress.com/2007/03/28/open-question-scarring-for-the-bunimovich-stadium/. [Online; accessed 19-April-2020].

[71] D. Terwagne, F. Ludewig, N. Vandewalle, and S. Dorbolo. "The role of deformations in the bouncing droplet dynamics.". Physics of Fluids 25, 122101 (2013).

[72] S. Thapa, N. Li, and J. Ye. Dynamic fluid surface reconstruction using deep neural network. In The IEEE Conference on Computer Vision and Pattern Recognition (CVPR)*, June (2020).*

[73] A. U. Oza, M. Labousse, S. Perrard, and J. W. M. Bush. "Pilot-wave dynamics in a harmonic potential: Quantization and stability of circular orbits.". Phys. Rev. E 93, 033122 (2016).

[74] A. U. Oza, R. R. Rosales, D. M. Harris, and J. W. M. Bush. "Pilot-wave dynamics in a rotating frame: on the emergence of orbital quantization.". J. Fluid. Mech., vol. 744, pp. 404-429 (2014).

[75] A. U. Oza, O. Wind-Willassen, D. M. Harris, R. R. Rosales, and J. W. M. Bush. "Pilot-wave hydrodynamics in a rotating frame: Exotic orbits.". Physics of Fluids, vol. 26, 082101 (2014).

[76] N. Vandewalle, B. Filoux, and M. Hubert. "Bragg's reflection for walking droplets in 1D crystals.". arXiv:1904.05778v1 (2019).

[77] Veritasium. Is this what quantum mechanics looks like? https://www.youtube.com/watch?v=WIyTZDHuarQ.

[78] Wikipedia contributors. The copenhagen interpretation — Wikipedia, the free encyclopedia. https://en.wikipedia.org/wiki/Copenhagen_interpretation, (2020). [Online; accessed 27-May-2020].

[79] Wikipedia contributors. De broglie-bohm theory — Wikipedia, the free encyclopedia. https://en.wikipedia.org/wiki/De_Broglie\T1\textendashBohm_theory, (2020). [Online; accessed 27-May-2020].

[80] Wikipedia contributors. Hopf bifurcation — Wikipedia, the free encyclopedia. https://en.wikipedia.org/wiki/Hopf_bifurcation, (2020). [Online; accessed 04-June-2020].

[81] Wikipedia contributors. Horseshoe map — Wikipedia, the free encyclopedia. https://en.wikipedia.org/wiki/Horseshoe_map, (2020). [Online; accessed 04-June-2020].

[82] Wikipedia contributors. Interpretations of quantum mechanics — Wikipedia, the free encyclopedia. https://en.wikipedia.org/wiki/Interpretations_of_quantum_mechanics, (2020). [Online; accessed 27-May-2020].

[83] Wikipedia contributors. Quantum hall effect — Wikipedia, the free encyclopedia. https://en.wikipedia.org/wiki/Quantum_Hall_effect, (2020). [Online; accessed 11-June-2020].

[84] Wikipedia contributors. Régression linéaire — Wikipedia, the free encyclopedia. https://fr.wikipedia.org/wiki/Régression_linéaire, (2020). [Online; accessed 13-May-2020].

[85] Wikipedia contributors. Schlieren photography — Wikipedia, the free encyclopedia. https://en.wikipedia.org/wiki/Schlieren_photography, (2020). [Online; accessed 15-May-2020].

[86] Wikipedia contributors. Tight binding — Wikipedia, the free encyclopedia. https://en.wikipedia.org/wiki/Tight_binding, (2020). [Online; accessed 06-June-2020].

[87] Wikipedia contributors. Two-dimensional electron gas — Wikipedia, the free encyclopedia. https://en.wikipedia.org/wiki/Two-dimensional_electron_gas, (2020). [Online; accessed 06-June-2020].

[88] O. Wind-Willassen. "Drops on hydrophobic surfaces and vibrated fluid surfaces.". Doctoral thesis. DTU, (2014).

[89] O. Wind-Willassen, J. Molacek, D. M. Harris, and J. W. M. Bush. "Exotic states of bouncing and walking droplets.". Physics of Fluids 25, 082002 (2013).

UNIVERSITÉ CATHOLIQUE DE LOUVAIN
École polytechnique de Louvain
Rue Archimède, 1 bte L6.11.01, 1348 Louvain-la-Neuve, Belgique | **www.uclouvain.be/epl**